ELECTROCHEMICAL INVESTIGATION OF ION IMPLANTED *p*-Si

THÈSE N^O 2783 (2003)

PRÉSENTÉE À LA FACULTÉ SCIENCES ET TECHNIQUES DE L'INGÉNIEUR

Institut des matériaux

SECTION DES MATÉRIAUX

ÉCOLE POLYTECHNIQUE FÉDÉRALE DE LAUSANNE

POUR L'OBTENTION DU GRADE DE DOCTEUR ÈS SCIENCES

PAR

Adrian SPIEGEL

ingénieur en sciences des matériaux diplômé EPF
de nationalité suisse et originaire de Zürich (ZH)

acceptée sur proposition du jury:

Prof. P. Schmuki, directeur de thèse
Dr M. Döbeli, rapporteur
Prof. H. J. Mathieu, rapporteur
Prof. S. Virtanen, rapporteur

Lausanne, EPFL
2003

CONTENTS

3 Experimental   45

4 Results and Discussion   59

ABSTRACT

The present work investigates the possibility of selective electrochemical metal deposition on ion implanted p-Si. The idea is that defects introduced into the substrate by ion implantation make it more susceptible to electrochemical reactions compared to intact Si; this increased sensitivity is to be used for selective reactions at the defect sites. It is believed that the increased reactivity is due to a lowering of the Schottky barrier breakdown potential, U_{bd}, of the semiconductor-electrolyte interface due to the introduction of additional energy states in the semiconductor's bandgap. These additional states may be used for facilitated charge transfer by direct tunnelling enabling spatially well defined electrochemical reactions at the implant sites.

In a first step the damage created by ion implantation (Ga^+ and Au^{2+} by focused ion beam, FIB; Ga^+ by broadband ion implantation, BII) was analyzed and compared to numerical simulations. Optical microscopy, REM, AFM, and Raman spectroscopy were for characterisation. It was found that the damage created was in good agreement with the theoretical models: more damage was created for heavier ions and higher ion doses. AFM proofed to be a valuable tool to assess surface sputtering for high implant doses, while optical microscopy was more sensitive for low doses. Raman spectroscopy was used to determine the degree of amorphization of the substrate. We found that amorphization doses varied considerably depending on the implantation mode used. For BII the dose needed for amorphization was similar to values reported in the literature, while FIB implantation needed doses roughly 50 times higher. We assume that this is due to the very high current fluences in the FIB combined with short pixel dwell times during the implantation process; both these factors promote self healing of the substrate, hence a higher dose is needed for amorphization to take place.

Deposition experiments at different potentials and in different electrolytes on samples implanted with varying doses lead to the following findings. Selective electrodeposition on ion implanted p-Si is possible, however, deposition conditions have to be chosen carefully. Low and high (close to or above the amorphization limit) implant doses lead to unsatisfactory deposits (sample not fully covered). We assume that in the first case, not enough defect sites are present for sufficient formation of initial nuclei, while in the second case the amorphous substrate seems to behave as an insulator making any deposition virtually impossible. Also, for the successful deposition of Cu from an acidic electrolyte, benzotriazole, a brightening agent, was added to improve deposit quality. The result were finely grained, even, and well delimited deposits with a resolution matching that of the implant process (~200 nm). Deposition time and potential are crucial too, as long times and more cathodic potentials promote outgrowth, while short deposition times and potentials close to the open cell potential, ocp, may not suffice to cover the implant site completely.

Microcapillary measurements were used to measure on either intact or implanted sites only, thereby minimizing other, undesirable influences. It was found that on intact Si, the Schottky diode stays intact down to potentials as low as several V, whereas on implanted Si reactions began to take place typically below -500 mV indicating that the Schottky barrier has broken down. Also, amorphous samples showed a different behaviour from all the others without any distinct U_{bd} and an ocp shifted by several hundred mV towards more cathodic potentials.

Finally, samples implanted by ion projection direct structuring, IPDS, were used to test the suitability for possible industrial applications. It was found that, even though implant conditions were quite different from before (noble gas ions at 75 keV vs. Ga^+ at 30 keV) selective electrochemistry was still possible. Patterns as small as 150 nm were resolved over a surface of several mm^2.

RÉSUMÉ

Ce travail de thèse porte sur l'électrodéposition sélective de métaux sur silicium de type p (p-Si) induite par des défauts nanométriques créés par l'implantation ionique. Le principe de dépôt électrochimique sélectif est basée sur l'effet débloquant induit par les défauts. L'interface p-Si/électrolyte, par analogie avec une jonction de Schottky, présente un comportement bloqué pour les polarisations cathodiques. Aussi, comme pour une diode, il existe un potentiel de claquage, U_{bd}, au dessus duquel il est de nouveau possible de faire circuler un courant à travers l'interface p-Si/électrolyte. Dans les cas d'une surface endommagée (par exemple suite à un bombardement ionique) le U_{bd} est atteint pour des surtensions moins cathodiques que pou une surface intacte. Ainsi, en appliquant une tension comprise entre le potentiel de claquage d'une surface contenant des défauts et celui d'une surface intacte des réactions électrochimiques sélectives deviennent possibles.

Dans une première étape, les défauts créés soit par l'implantation d'ions Ga$^+$ et Au^{2+} à l'aide d'un faisceau ionique focalisé, FIB, soit par bombardement d'ions Ga$^+$ via un implanteur industriel, BII, ont étés analysés et comparés à des simulations numériques. Un bon accord est apparu entre les simulations et les mesures expérimentales effectuées par microscopies à force atomique et optique. Lorsque la masse ionique et la dose augmentent, les défauts s'avèrent plus importants. Les analyses par spectroscopie Raman montrent une amorphisation du substrat dans les zones implantées. Dans le cas des échantillons implantés par BII le seuil d'amorphisation, d_a, correspond aux valeurs trouvées dans la littérature. À l'inverse, pour les échantillons implantés par FIB, la dose d_a est supérieure d'un facteur 50 environ. Il semble que cet écart puisse être expliqué par les conditions extrêmes de l'implantation par FIB (haute densité de courant, temps de repos par pixel court) qui faciliterait la diffusion des défauts dans le cristal augmentant ainsi sa tolérance aux défauts.

Des dépôts sélectifs ont été réalisés dans diverses conditions électrochimiques sur substrats implantés à des doses variables. Bien que le dépôt sélectif de cuivre à partir d'un électrolyte acide soit possible, les structures ainsi déposées sont peu satisfaisantes: tailles de grains élevées, bords mal définis et recouvrement insuffisant. En optimisant les paramètres électrochimiques et en ajoutant un agent de lissage, le benzotriazole, il a été possible de former des structures de très bonne qualité: grains fins, bords bien délimités, dépôts denses et compacts. Des résultats intéressants ont aussi été obtenus en utilisant un électrolyte basique contentant des ions d'or. Dans les conditions optimales, la résolution latérale des dépôts est similaire à celle des zones implantées Il a donc été possible de réaliser des structures présentant une résolution latérale égale à 200 nm. Vu l'aire très réduite des zones implantées comparée à la surface en contact avec l'électrolyte, des mesures électrochimiques à l'aide d'une cellule micro-capillaire ont été effectuées afin de distinguer le comportement propre des zones implantées de celui de la surface intacte. La différence est clairement visible: pour une surface intacte aucune réaction électrochimique n'est observée jusqu'à des valeurs de surtension cathodique de plusieurs volts. Le U_{bd} mesuré par micro-capillaire est décalé de plus de $-4\,V$ par rapport à une mesure électrochimique macroscopique. Par contre, pour des surfaces implantées des réactions apparaissent à partir d'environ $-0.5\,V_{SCE}$. Ainsi, la sélectivité du dépôt électrochimique peut très probablement s'expliquer par la différence entre le potentiel de claquage d'une surface intacte et celui d'une surface endommagée.

Enfin, des échantillons ont été implantés par une technique appelée "ion projection direct structuring", IPDS, où des ions sont projetés sur une large surface à travers un masque. Ainsi, il est possible d'implanter des surfaces de plusieurs mm^2 en quelques secondes alors que l'utilisation d'un appareil FIB et son mode linéaire de fonctionnement requerrait plusieurs heures pour le même résultat. Par la technique IPDS, il a été montré que la formation de structures présentant une résolution latérale de 150 nm était possible et ceci à grande échelle, même si les conditions de dépôt sont assez différentes de celles étudiées auparavant.

Chapter 1

INTRODUCTION

1.1 Overview

The drive towards smaller, faster, and cheaper micro- and nanoscopic components has had a profound impact on engineering in general and specifically on the field of materials science. Next to electrical engineering, materials science has probably played the most important role in the development of microdevices and continues to do so. Since the invention of the integrated circuit (IC) in 1958 by Kilby [1], every new step in miniaturisation has presented engineers with obstacles to overcome: light-sources had to be built, lithographic masks (and materials offering both high resistivity and ultra-fine resolution) had to be developed, photoresists reacting under very specific lighting conditions and able to mask in the 100 nm region had to be found, and so on. And with decreasing feature size (currently 110 nm, reaching 90 nm and less in the next year or two) the difficulties to find viable solutions are increasing.

Semiconductor (SC) metalization in particular has continuously gained in importance. While the following list is not complete, it may give an overview over the applications of SC metalization:

- As the number of transistors per chip increases exponentially, the number of metallic interconnects is growing at an even higher rate. Problems of increasing power consumption have forced the industry to adopt copper instead of aluminium as interconnect material. For future improvements small low-resistivity interconnects are needed.

- Advances in the growing field of micro- and nano electromechanical systems (MEMS and NEMS) are only possible if structures on a sub-micrometer scale can be easily produced.

- The field of quantum confinement research investigates effects that only manifest themselves on a length scale comparable to that of single molecules and therefore depends on the ability to build such structures.

While photolithography has been very successful in the field of miniaturization and has helped to keep up with Moore's law[1], fundamental problems may force the industry to begin considering new approaches for microstructuring materials; after all 'if there is no attempt to find alternatives, they will never be found' [3].

This thesis investigates a possible alternative approach to produce said metallic micro- and nano-structures: selective electrochemistry on ion beam implanted silicon. We believe that this technique may offer feasible solutions to the problem of SC metalization.

We have investigated the possibilities offered by the combination of a high resolution ion beam-based pattern reproduction (either maskless with a focused ion beam, FIB, or using stencil masks and broad-band ion implanters, BII) followed by selective electrochemical metal deposition. Due to the particle-nature of ion beams their resolution is not limited by their wavelength but rather by technological problems such as the construction of higher resolution ion beam devices; these problems can –theoretically– be overcome. Optical techniques are inherently limited by the wavelength of the light used. FIBs with a resolution in the 10 nm range are available today and it is likely that better machines will be developed.

Electrochemistry takes place on an atomic or molecular scale, and resolution limits are therefore very low. Thermodynamically stable structures of ten metal atoms, i.e. roughly 1-2 nm, do exist [4], a size range which can probably be considered to be the ultimate resolution for any 'standard' miniaturization technique. We therefore believe, that electrochemistry can resolve patterns produced by high-resolution ion beam techniques. It remains to be seen if mask- and resistless selective techniques may also reach these resolutions.

---

1. Moore's law [2] was formulated in the 1960. He predicted –on an almost entirely empirical basis– that circuit density of an IC would double every 18 months; Moore's law has turned out to be astonishingly accurate for almost 40 years now.

To emphasize the differences between photolithographic techniques and our proposed approach, both techniques will be explained briefly. Only a short introduction to photolithographic chipmaking will be given here; for more comprehensive information several sources are available [5-7].

Figure 1.1 shows the principal steps of photolithographic microstructurization:

- A clean wafer is covered by a layer of photoresist.
- A mask is placed close to the wafer surface and light projected through the mask. As a consequence chemical bonds are broken in the photoresist where it is exposed to the light (positive resist).
- Washing/dissolving follows; the previously exposed photoresist is dissolved (only an image of the mask remains on the wafer).
- Metal is deposited onto both the wafer surface as well as the remaining photoresist.
- Finally, the remaining photoresist is removed. The desired metal structure remains.
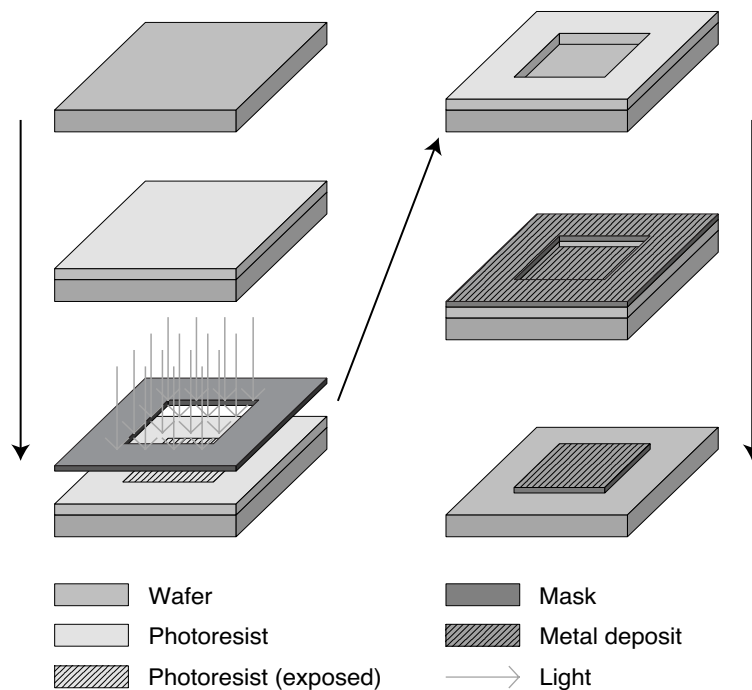
Fig. 1.1: Schematic overview of photolithographic microstructuring

Photolithographic microstructuring involves many individual and complex steps. Maintaining the desired precision during the process becomes increasingly difficult as the structure size decreases. Given these limits, we investigated an alternative approach to microstructuring of semiconductors (see figure 1.2):

- A clean wafer is implanted with ions; the implant sites correspond to the desired shape of the metal structure. Implantation may be performed with by FIB (maskless implantation for flexibility in design, the beam is raster-scanned over the surface to produce the desired pattern) or using ion projection lithography, IPL, where a broad ion beam is projected through a stencil mask (for large scale applications).
- Structures are grown on the implant sites by selective electrochemistry.
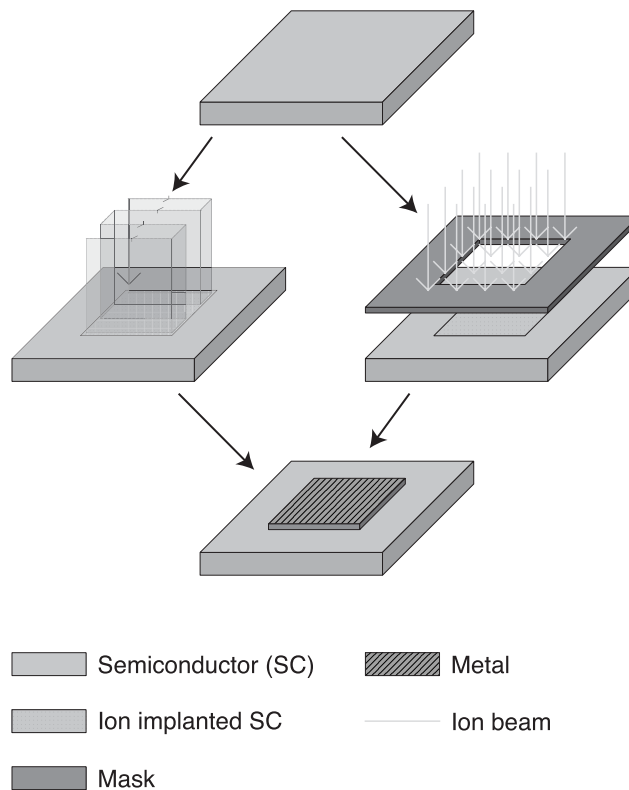
Fig. 1.2: Schematic representation of selective electrodeposition on ion beam induced damage sites.

We believe that the ion beam-based approach offers some new, interesting properties when compared to photolithographic metalization.

- It is based on properties inherent to damaged SCs. Therefore this approach should not be limited by the wavelength of the particle beam used, but only by the size of the damage zones created. Damage zones in the range of 100 nm were obtained during our work and, based on work by others [8], we are confident that 50 nm or less can be achieved.

- The range of materials that can be deposited is very broad and includes different metals (Cu, Au, Ni, Pd, etc.), semiconductors (CdS, etc.), and insulators (various electropolymers). Applications based on selective dissolution (selective formation of porous semiconductors [9, 10]) are also possible. One could also imagine applications based on the changed electrochemistry of the defect zone (micro-sensors, lab-on-a-chip systems, etc.).

- The process appears to be 'simple' as only two steps are involved. Also, the use of potentially hazardous substances (solvents, etc.) is reduced.

- Mask production is either not needed (if a FIB is used for pattern reproduction) or greatly simplified as the mask pattern is further demagnified by a factor 4 to 8.

- The method is 'robust': we have obtained structures with a resolution of 100 nm over several mm^2 in a standard laboratory environment.

1.2 Literature

The following section provides an overview of the field of electrochemical micro- and nanostructuring, concentrating on metalization and ion beam related techniques.

1.2.1 Metal Deposition

Metal deposition on SC surfaces or metalization plays an important role in the electronics industry [11-14] as it is a key step in many applications. As mentioned before, interconnects [15-17] and mechanical structures [18, 19] depend on it.

In Schottky [20, 21] and ohmic [22] junctions metals are brought into direct contact with a semiconducting substrate. Depending on the respective work functions either an ohmic or a Schottky junction is established [23]. Field effect transistors (FETs) such as

metal-oxide-semiconductor field effect transistors (MOSFETs) [24] and metal-semiconductor-FETs (MESFETs) [23, 25] also depend on metal-semiconductor interfaces.

In state-of-the-art processors such as Intel's Pentium 4 or Motorola's G4 tens of millions of transistors [26] and other elements are connected by even more interconnects. While these interconnects have originally not received much attention, power consumption and heat development have recently forced the industry to move from aluminium to copper as interconnect material (as it conducts electricity much better than Al) [27-29].

Gold has attracted some attention as a potential heat sink [30] and its easy solderability make it an attractive material in the IC industry [31, 32]. Other possible applications of microstructured Au-patterns lie in the field of sensors and biology. The 'docking' of specific molecules onto surfaces can be monitored in-situ by combining integrated circuits with specific catalytic entities such as Au or Au-based alloys [33, 34].Biotechnology uses Au-structured templates to grow cells on pre-defined patterns [35, 36]. Bio-sensors often use metal coated porous membranes as electrodes [37, 38] for sensing.

a)   Deposition Techniques

Depending on the desired application a wide range of metalization techniques exists today. However, most of these techniques can be attributed to one of the following categories: deposition from the vapour phase or from the liquid phase.

For deposition from the vapour phase, direct line-of sight methods are summarized with the term physical vapour deposition, as opposed to chemical vapour deposition, CVD, which is based on diffusive-convective gas transfer and which involves a specific chemical reaction at the substrate.

Metal deposition from the liquid phase is carried out by immersion of the substrate into a metal containing liquid. If no external voltage is applied the metal is either present in liquid form and binds chemically to the substrate or is dissolved as ions in the electrolyte. In the later case the metal ion is part of a redox couple present in the electrolyte; the redox reaction takes place at the sample surface once the latter is immersed into the liquid.

If an external voltage is applied for metal deposition to take place one speaks of electro-chemical metal deposition. A negative potential is applied to the substrate to force the metal-lic anions present in the electrolyte to adsorb at the cathode (the substrate under negative potential), where they are reduced to their metallic form. By varying the applied potential, the duration, and the electrolyte composition, the deposition process can be adapted to a broad range of conditions. The equipment as well as the reagents needed for electrochemical metal deposition are cheap and easily available and, because the process takes place in the liquid phase, it is rather robust: a resolution in the sub 200 nm range can be obtained even in a standard laboratory environment.

Electrochemical metal deposition has been described extensively [39-48] as it is considered to be a model electrochemical system. Nucleation and growth phenomena have been studied and a theory −based on nucleation and growth from the gas phase− has been established [49].

In the 1960's, Gerischer *et al.* adapted this idea to describe the electrolyte/semiconductor interface [50, 51]. Details concerning SC electrochemistry can be found in chapter 2 of this thesis. In general metals are deposited onto *n*-type SCs [20, 52] or onto *p*-type SCs under illumination [53] (for an introduction into the behaviour of semiconductors please refer to chapter 2.1.2). Only recently successful attempts have been made to deposit metals onto *p*-type SCs [54, 55].

Traditionally the semiconductor industry has mostly relied on deposition from the gas phase. However, the switch from Al to Cu interconnects has stirred interest in the field of both electroless [56, 57] as well as electrochemical [58] metalization. Mainly the electro-chemical deposition of Cu onto SCs as well as onto barrier layer materials has been studied since Cu can be deposited quite easily from the liquid phase. Furthermore, by choosing appropriate electrolyte systems, phenomena such as superfilling [29, 58, 59] can be used to metalize deep trenches or other complex geometries that would lead to the formation of gaps if other techniques were used.

1.2.2 Microstructurization by Ion Beam

This chapter provides a short overview on some of the surface structuring techniques that have been put into place using ion beam devices. We will not limit ourselves to purely lithographic systems but will also consider techniques that make direct use of the surface structuring properties (by sputtering or implantation) of the beam. Due to the focus of this work, electrochemical techniques will be treated in more detail. While microstructurization by ion beams is not the most widely used technique, it will be treated more extensively. For an summary of other electrochemical microstructurization techniques please refer to chapter 1.2.3.

Ion beams, and more specifically focused ion beams (FIB), have been a valuable tool in micron and submicron technology for the last 30 years [60, 61]; they can be used for a broad range of applications such as IC repair and modification [62], failure analysis [63], lithographic mask repair [64], and FIB lithography [65]. In an industrial environment FIBs are especially useful in the pre- and early- production phase due to their high spatial resolution and their flexibility with respect to ion species, dose, energy, and pattern design [66]. If a FIB system is further equipped with a mass separator, a liquid alloy ion source, LAIS (see chapter 3.2.1) can be used to obtain different ions with varying charges from he same source, which is particularly useful for implantation experiments [67]. Another application is direct pattering by ion milling for the production of micromechanical components [68], micro- and nano-imprinting tools [69-71], or SEM and TEM sample preparation [72]. If a precursor gas is used, direct pattern [73] or mask deposition [74, 75], as well as chemically enhanced local etching [76, 77] become possible. And, last but not least, the FIB can be used for surface analysis as a scanning ion microscope [78].

a)   Resist-Based Systems

Due to their particular nature, ion beams can be used to directly expose resist layers on a substrate. If a FIB is used to expose the resist, the operation is comparable to e-beam lithography: the desired structure is drawn using appropriate software and transferred by direct writing into the resist by a computer-controlled ion beam. Positive or negative-resist systems exist [79], as the incoming energy of the beam can be used to either break existing bonds in the resist material (positive resist, e.g. PMMA) or to create such bonds (negative resist). Resists may be organic (similar or identical to the ones used for e-beam lithography) [80] or inorganic layers such as Al_2O_3 [81]. Fuhrman *et al.* have shown that even the H-terminated surface of Si after a 1 min HF dip can be used as a negative resist [82, 83]: FIB treatment leads to hydrogen desorption at the FIB-impact sites. These sites were then passivated by O_2 to form SiO_2. In a subsequent etch step in different etchants, this natural oxide proved to be sufficient for selective etching of the substrate.

One of the advantages of FIB-lithography when compared to e-beam lithography is that the dose required to expose the resist –in terms of $\mu C/cm^2$– is usually about two orders of magnitude lower than the dose required for exposure by electrons. This is due to the fact that ions in the 30 keV - 200 keV energy-range lose most of their energy in the resist while electrons with an energy of 20 keV - 100 keV penetrate deep into the substrate and lose only a small fraction of their energy in the resist [8]. The mechanism of ion exposure of a resist is mainly determined by the energy transferred from the ions to the electrons in the resist (electronic stopping power). Therefore, the activated volume is smaller and precise control can be maintained more easily.

Instead of using a focused beam to expose the resist, it is also possible to use an unfocused beam in conjunction with a stencil mask; in this case, one speaks of ion projection lithography. This approach allows features as small as 50 nm [8], and permits a high sample throughput. Usually, the mask image is further reduced by ion-optics once the ion beam has passed through the mask; therefore, the demands for mask precision are not as strict as for other nano technologies. Due to its excellent resolution, IPL is a possible candidate for sub 100 nm lithography.

b)   Micromachining

Ion beams are frequently used for surface sputtering, either for cleaning sample surfaces (for surface analysis), for substrate vaporisation (SIMS), direct structuring (SEM, TEM sample preparation [72]), or direct 3D structuring to obtain microdevices and nanoimprinting stamps. Depending on the ions used, their dose and energy, the impinging ions will sputter the substrate surface, i.e. remove atoms and create 'grooves'. Since precise control is available over all 3 dimensions, complex geometries can be obtained [84-86]. Such structures can also be used as micro-imprinting-tools [69-71] where either a reactive precursor or the final material is placed on the nano imprinting tool.

Another mask- and resistless method for microstructuring semiconductors (or any other substrate for that matter) using ions is based on the energy released by the impinging ions: it is used to trigger a reaction with a reactive precursor gas present at low vapour pressure in the vicinity of the sample surface. The gas may either etch the sample surface (FIB assisted gas etching [87]) or crack under the influence of the ions to form a deposit [88, 89].

FIB assisted etching is often used to etch SiO_2 [90, 91] but can also be used to etch porous semiconductors [92] or even metals [93]. For example, to etch SiO_2 XeF_2 is used according to:

$$SiO_2 + 2(XeF_2) \; \overline{\quad FIB \quad} \!\! > \; SiF_4 + O_2 + 2\,Xe \qquad\qquad (1.1)$$
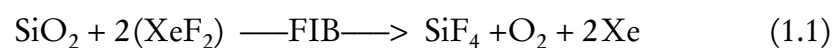
At the impact site SiO_2 reacts with the gaseous XeF_2 to form volatile SiF_4. The substrate is 'unprotected' at the reaction site and subsequent structuring is easily possible.
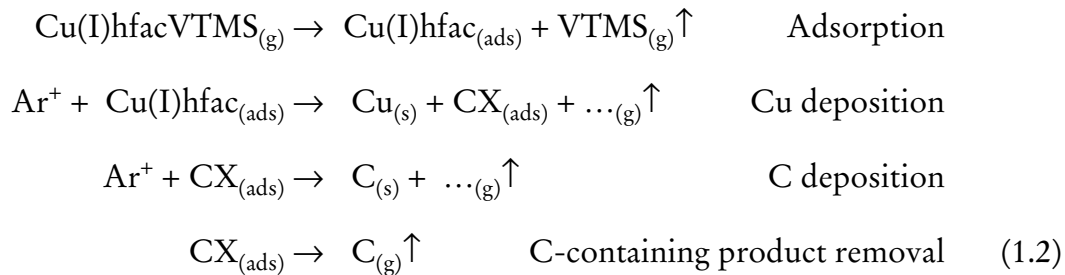
c)   Ion Beam Deposition Techniques

Ion beams with low energies in the region of some 100 eV have been used to deposit ions directly onto a surface. Using this method, shallow structures of Au have been obtained on Si [94]. Resolutions of 8 μm down to some 100 nm can be achieved; however, the necessary exposure time remains long. Similarly, Ga can be deposited directly using a Ga-ion source [95]. Due to the quality of available Ga-sources lines of 200 nm width have been obtained.

With higher energy beams (some 10 keV) buried, conductive layers of $CoSi_2$ have been obtained by implanting Co ions into Si, followed by an annealing step [96-98]. By varying the dose and the energy, the depth and the conductance of the buried layer can be controlled. A similar approach has been used to intermix thin layers of Pt and Co by bombardment with noble-gas ions [99]. The goal was to create magnetic domains in the order of 50 nm, which would be useful in structured magnetic media. This technique, called ion projection direct structuring, IPDS, is a potential candidate for future magnetic storage device production.

While most of the techniques described above suffer from low throughput due to the high ion doses needed, ion beam-induced chemical deposition tries to overcome that handicap by use of a precursor introduced close to the sample surface. The ion beam then acts as promoter and defines the precise location of the reaction. FIB induced CVD [88, 100, 101] is independent of the substrate, but the technique is employed regularly for mask-repair and IC-modifications.

The precursor gas is chosen such that its ion beam-assisted decomposition leads to the formation of structures on the sample surface. Depending on the precursor gas, these structures may be conducting [88, 102, 103] or insulating [100, 104, 105]; furthermore, a laser may be used to further increase deposition speed [106]. To deposit Cu structures, a gas like Cu(I) hexafluoroacetylacetonate vinyltrimethylsilane (Cu(I)hfacVTMS) is chosen, and deposition takes place according to reaction 1.2 [88].

$$
\begin{aligned}
Cu(I)hfacVTMS_{(g)} &\rightarrow\ Cu(I)hfac_{(ads)} + VTMS_{(g)}\uparrow &&\text{Adsorption} \\
Ar^+ + Cu(I)hfac_{(ads)} &\rightarrow\ Cu_{(s)} + CX_{(ads)} + \cdots_{(g)}\uparrow &&\text{Cu deposition} \\
Ar^+ + CX_{(ads)} &\rightarrow\ C_{(s)} + \ \cdots_{(g)}\uparrow &&\text{C deposition} \\
CX_{(ads)} &\rightarrow\ C_{(g)}\uparrow &&\text{C-containing product removal} \quad (1.2)
\end{aligned}
$$

While all the by-products evaporate, Cu (and residual C compounds) remain on the surface. Due to the C-contamination conductivity is usually lower than for elemental Cu; it can however be improved by subsequent annealing steps [107]. Kubena *et al.* have found that heating the substrate to >100 °C during deposition increases deposition ratio and sample conductivity for both Fe and Al structures [108].

d) Selective Electrochemistry on Ion Implanted Semiconductors

A different approach is used when implanted ions are used to change the substrate's electrochemical properties. In the semiconductor industry B atoms are frequently implanted and used as etch stops, as B-doped Si has a much higher etch resistance than undoped Si [25]. Several groups have used this effect to obtain sub-micrometer sized structures where the FIB-trace appears in relief after a KOH etch [109]. The process can be further improved to obtain complex structures (sloped sidewalls, cantilevers, and U-shaped freestanding beams) when use is made of the anistropical nature of the KOH etch [110, 111]. By using a photochemical HCl etch, critical doses for selective etching as low as $<3 \cdot 10^{10}\,Au/cm^2$ have been reported [112]. If HF is used as etchant, selectivity is reversed with respect to KOH: the implants now act as a positive resist. This effect has been used to obtain fine gratings for optical applications [113]. Xu *et al.* found that a KOH etch on Ga$^+$ implanted Si followed by rapid thermal annealing, cleaning in H_2SO_4, and a subsequent stain-etch in HF lead to freestanding structures of photoluminescent porous Silicon (π-Si) [114]. While the KOH selectively etched the Si surrounding the implanted structures, the HF lead to a porosification of the implant sites. It seems that selective wet-etching of ion implanted Si is not limited to Si substrates, but that III-V compounds such as GaAs, InP, InGaAs, and InGaAsP can be used as well [115].

Based on the observation that ion-beam induced damage makes SCs more susceptible to electrochemical reactions, Schmuki *et al.* showed that selective formation of π-Si on *n*-type SCs can be achieved electrochemically [9, 10, 116]. It is assumed that a shift of the material's Schottky barrier breakdown potential towards the open cell potential, ocp, takes place: normally a doped SC when brought into contact with an electrolyte, will show a diode-like current-voltage behaviour. For a *p*-type SC, the cathodic branch would be blocking due to a

lack of charge carriers in the depletion layer, while the anodic side would show a conducting behaviour; for n-type SCs the behaviour is reversed. At surface defects however, additional energy states are introduced into the SC, facilitating a direct passage of charge carriers from the SC to the electrolyte (or vice-versa). This effect has been used to locally porosify different SCs [9, 10], as well as to deposit different metals (Cu, Au, Pd, Ni) directly onto the damage sites with a resolution of up to 100 nm [54, 117, 118]; in these cases the defects were created by FIB implantation. For a more detailed description of SC electrochemistry please refer to chapter 2.1. For selective porosification n-type SCs are used (as they show a blocking behaviour on the anodic side of the current-density/voltage curve). At defects sites enough charge carriers are available for the anodic dissolution of the substrate (e.g. Si in an HF containing electrolyte). It is then possible to obtain porous, photoluminescent silicon with a pore-size in the sub-100 nm region. For the selective deposition of metals onto SCs, p-doped SCs have to be used as they are blocking on the cathodic side of the ocp.

Electrochemical techniques can also be used to obtain depth profiles of implanted species. This process, called delineation, is quite important for the semiconductor industry as precise knowledge over the distribution of implanted species is often needed. In this case electrochemistry is used to selectively etch either the substrate or the implanted species. The advantage is that the concentration selectivity can be controlled precisely. Delineation is used for quality control and device characterization [119] as well as for the production of working devices [120].

1.2.3 Other Microstructurization Techniques

Photolithography, the most widely used technology, has been described briefly before. A technique derived from photolithography is LIGA –a German acronym for lithography, electrodeposition and moulding– which uses a thick resist-layer and x-ray photons to achieve higher resolutions. Due to the thick resist layers, 3D moulds can be obtained to create complicated structures [121]. In general, the trend is towards short wave-length light sources in order to overcome the resolution limit.

For prototypes, mask development, small series, or high value items, e-beam lithography is frequently used. Its implementation is similar to FIB-lithography: a focused e-beam is raster-scanned over the resist-coated substrate, redrawing a previously defined structure. Currently e-beam lithography offers the highest resolution of all lithography techniques with structures as small as 10nm. However, due to the slow, linear writing process the samples are expensive. Therefore, e-beam lithography is usually used for high value applications such as mask development.

Kolb *et al.* have used a scanning tunnel microscope (STM) in solution to deposit metal on the STM-tip [122, 123]. In a second step these metal cluster (both Au and Pd) were deposited on the substrate surface. As the technique is *in-situ* it is possible to observe the deposited nano-dots directly after deposition.

Recently, attempts have been made to use scanning probe techniques for nanostructuring materials. One attempt is to use an electrolyte filled nanocapillary to scan the surface [124]. This device −termed ESCM− can either be used as a microscope to reveal both topographical as well as electrochemical information about the substrate, or as a lithography tool which can deposit or dissolve material with a resolution of roughly 100nm. It works on any conducting surface and may become a valuable tool in determining the corrosive properties and the detailed corrosion mechanisms of complex multi-phased alloys.

Atomic force microscopes have been used to scratch a *p*-Si substrate in order to sensitize it for selective electrodeposition of metals or remove a masking oxide layer [55, 125]. The principle of the first application is the same as the one used in this work: by introducing additional states at the defect sites the substrate becomes locally sensitized to electrochemical reactions; however, experiments were only partially successful as neither damage-zone coverage nor selectivity could be controlled [125]. The use of an oxide layer as mask material and its removal by AFM has proven to be a viable possibility to produce structures in the 100nm range [55, 125].

Chapter 2

THEORY

2.1 Semiconductor Electrochemistry

2.1.1 Basic Concepts of Electrochemistry

Electrons in metals are more or less free to move and most of the rate limiting steps involved in their electrochemistry are due to the behaviour of the charge carriers in the electrolyte. In SCs on the other side, electrons may not be able to move freely due to the presence of the bandgap. In order to control electrochemical reactions on SC surfaces it is therefore important to understand the implications of this behaviour.

Electrochemical reactions always involve the transfer of at least one electrical charge (electron) from one species (reducing agent, i.e. a substance that can donate electrons) through an ionic conductor (electrolyte) to another species (oxidant, i.e. a substance that can accept electrons). The two sites of the reaction are called electrodes or more precisely cathode (usually the place of reduction) and anode (usually the place of oxidation) respectively; the place where they are in contact with the electrolyte is the interface. In order for a current to flow, the two electrodes must be connected by an electronic conductor, usually a simple wire, in which electrons flow from the anode to the cathode; obviously in the electrolyte the cations move in the opposite direction as shown in figure 2.1.
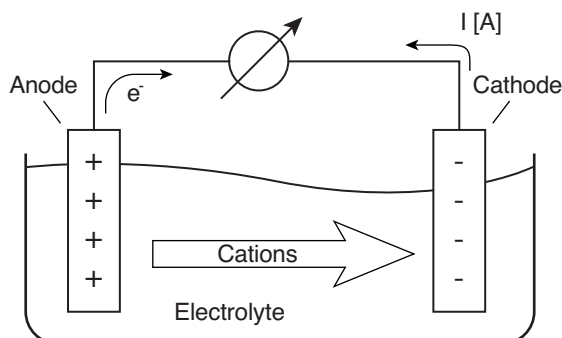
Fig. 2.1: Current flow in an electrochemical cell.

The charge transfer at the two electrodes generates a current which is by definition positive at the anode and negative at the cathode. In electrochemical experiments one can only measure the sum of these two currents since they are using the same path of conduction. It is however possible to calculate these partial currents using so-called Tafel slopes; this technique uses the fact that, under oxidising conditions, it is possible to neglect the cathodic current and vice versa. To the following reference provides an excellent introduction into the field of electrochemistry [126].

2.1.2 Energy Bands and the Semiconductor

The conduction properties of solids are determined by their electronic band structure which results from the overlap of the energy levels of all atoms being part of the solid. Since the number of energy levels present in a solid is almost infinite, their combination results in the creation of continuous energy bands [23, 127] as opposed to the discrete energy levels which characterise single atoms or molecules. These energy bands are filled with electrons, starting at the lowest energy band until the Fermi energy level (E_F). The highest filled band and the lowest empty band are termed valence and conduction band, respectively. The upper limit of the valence band is called E_v while the lowest level of the conduction band is called E_c. In the case of overlapping energy bands –e.g. for metals– the solid is an electronic conductor, i.e. electrons are free to move. If, however, the energy bands are separated by what is called an energy- or bandgap, the material is no longer conducting; it is either an insulator or a SC

depending on the value of the gap. The value of the bandgap is designated E_g ($E_g = E_c$ - E_v). Usually a material is considered to be a SC if the bandgap does not exceed roughly 3 eV, i.e. if thermal fluctuations may excite an electron into the conduction band, leaving a hole in the valence band. The electric current is then carried by electrons in the conduction band and holes in the valence band (figure 2.2). If the bandgap exceeds 3 eV, the material is considered an insulator as electrons will not be able to pass from the valence to the conductance band spontaneously.
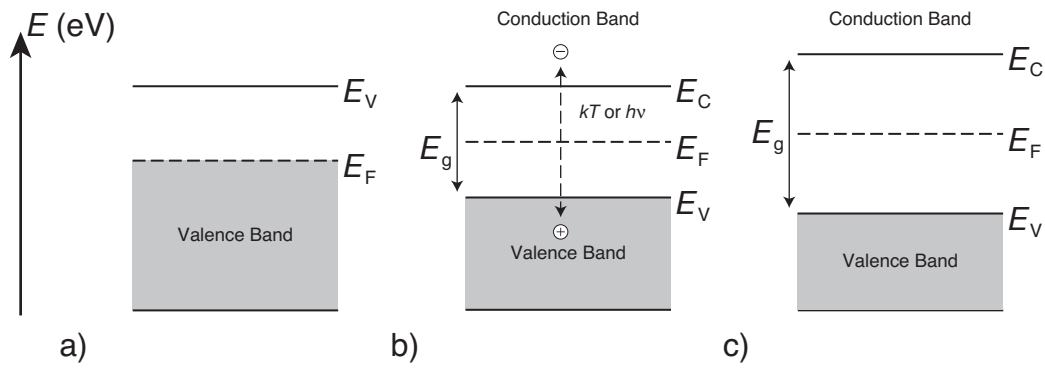
Fig. 2.2: Band structure in an a) electronic conductor, b) semiconductor, c) insulator; gray areas designate bands filled with electrons.

One can distinguish two different types of SCs: intrinsic and extrinsic. The first type presents an ideal model that is encountered in pure SCs only. The Fermi level lies exactly in the middle between the conduction and valence band (see Eq. 2.1) and, therefore, conductivity is low as electron-hole pairs can hardly be created.

$$E_F = E_V + \frac{E_g}{2} \tag{2.1}$$

Due to impurities and defects, such as vacancies or interstitials, real crystals have additional –new– energy levels in the band gap. Thus SC properties can be changed by adding controlled amounts of impurities (doping) which create additional energy levels close to either the conduction or the valence band. Two types of impurities can be added to a SC. If the number of valence electrons of the dopant species is higher than that of the SC's lattice, the

dopant is called donor as it leads to an excess of electrons (e^-) in the crystal. If the dopant has less valence electrons than the SC's lattice, the dopant is called acceptor and leads to the creation of mobile holes (h^+) as charge carriers. At $T = 0\,\text{K}$, the first case corresponds to an excess of electrons in the band gap close to the conduction band and, therefore, one speaks of n-type SC; the majority carriers are electrons. In the second case acceptor levels are added in the band gap close to the valence band; here one speaks of p-type SC and the majority carriers are holes. For $T > 0\,\text{K}$ or under illumination, ionization of the doping species occurs, leading to an electron transfer and the creation of electron-hole pairs as described in figure 2.3. The conductivity of doped SCs is much higher than the one observed for intrinsic SCs.

To know the number of charge carriers available per unit volume (i.e. the electron density), one has to evaluate the electron density n(E) in an incremental energy range dE. This is given by the product of the density of allowed energy states per unit volume N(E) and the probability of occupying that energy range P(E); the energy for which the probability of occupation is 0.5 is E_F. For an intrinsic SC E_F is situated in the centre of the bandgap, while for extrinsic ones it is a function of the donor impurity density, N_D:

$$E_F = E_C - k \cdot T \cdot \ln\left(\frac{N_C}{N_D}\right) \qquad (2.2)$$

where E_C is the bottom of the conduction band, N_C the effective density of states in the conduction band, k the Boltzmann constant, and T the temperature. Thus, E_F lies either just a few kT above the valence band (for a p-type SC) or slightly below the conduction band (for a n-type doped SC). The band structure of an intrinsic and of a doped SC is visualised in figure 2.3. For a more detailed introduction to the field of SCs please refer to [128].
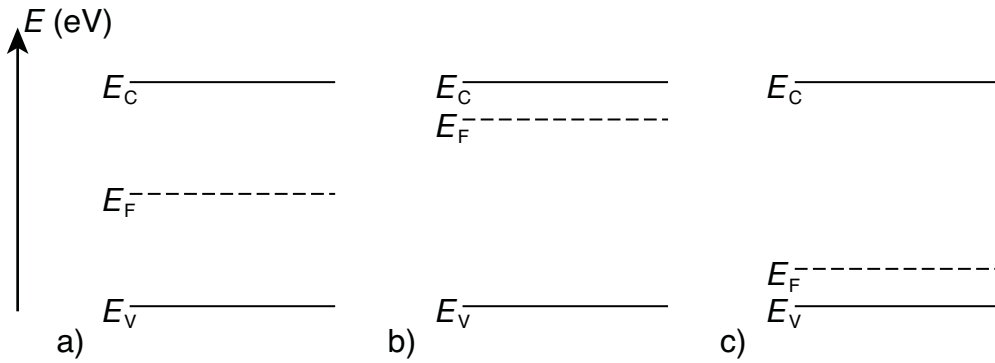
Fig. 2.3: Band structure in an a) intrinsic, b) n-type, c) p-type semiconductor

When two conducting phases are brought into contact, their Fermi energy levels will equalise at the point of contact by transferring electrons from one phase to the other. This electron flow gives rise to a contact potential ΔV. The direction of electron flow is determined by the work function: electrons flow to the phase with the higher work function until the Fermi levels at the point of contact are equal. In a SC this electron movement leads to a region where the atoms become ionised, the space charge region or space charge layer, SCL. The width of the space charge region, W_{scl}, depends on ΔV, the donor concentration and other parameters but is typically in the region of 10^{-3} to 10^{-4} mm. The potential difference between the bulk Fermi energy level, $E_{F,b}$, and the surface's Fermi energy level, $E_{F,s}$, is called the Schottky barrier U_{Sb}.

If one brings into contact a metal and a SC two different kinds of contact may form depending on their relative work function. If the work function of the metal is higher than that of the SC, the electrons will move from the SC to the metal leaving back a region of positively charged ions, the so-called depletion region (since it is depleted of conducting electrons). This case is referred to as Schottky barrier (or blocking contact) since the depletion region acts as an actual insulator and is shown in figure 2.4. If, on the other hand, the metal has a lower work function than the SC, the electrons will flow from the metal into the conduction band of the SC leading to an ohmic contact. In either case a band-bending occurs at the interface [129].
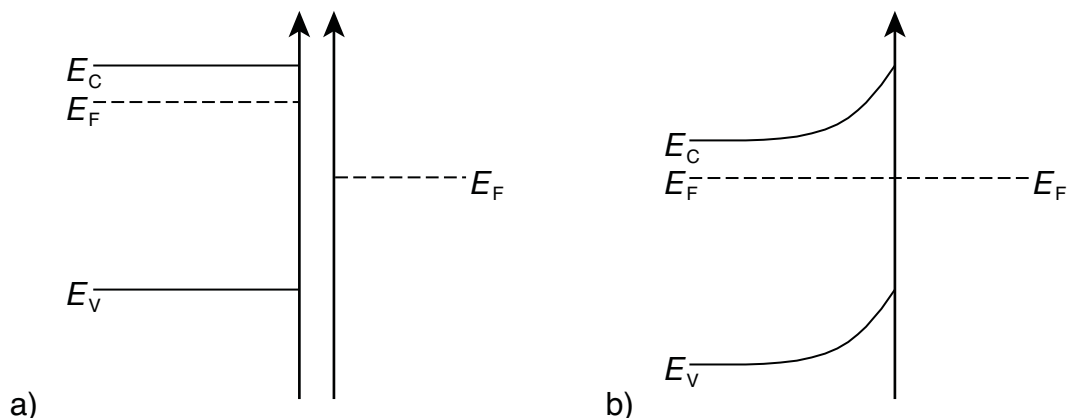
Fig. 2.4: Formation of a Schottky barrier between a metal and a semiconductor; a) before, b) after contact

The same reasoning used to describe contacts between a SC and a metal can be used to describe contacts between n- and p-type SCs of either the same or of different materials (homo- and heterojunction). Also the contact between a SC and an electrolyte can be described using the same approach.

2.1.3 The Electrolyte - The Marcus-Gerischer Model

The electronic properties of electrolytes have been studied by Marcus and Gerischer [51, 130-132]. In their model, the electrolyte is treated in analogy to a solid, where the energy bands are replaced by concentrations of ions. Oxidized and reduced species present in the electrolyte do not have the same energy due to a different degree of solvatation. The oxidized species are acceptors which correspond to the empty electronic levels, while the reduced species are donors which correspond to the occupied electronic levels. The density of states $D(E)$ is given by [51, 130]:
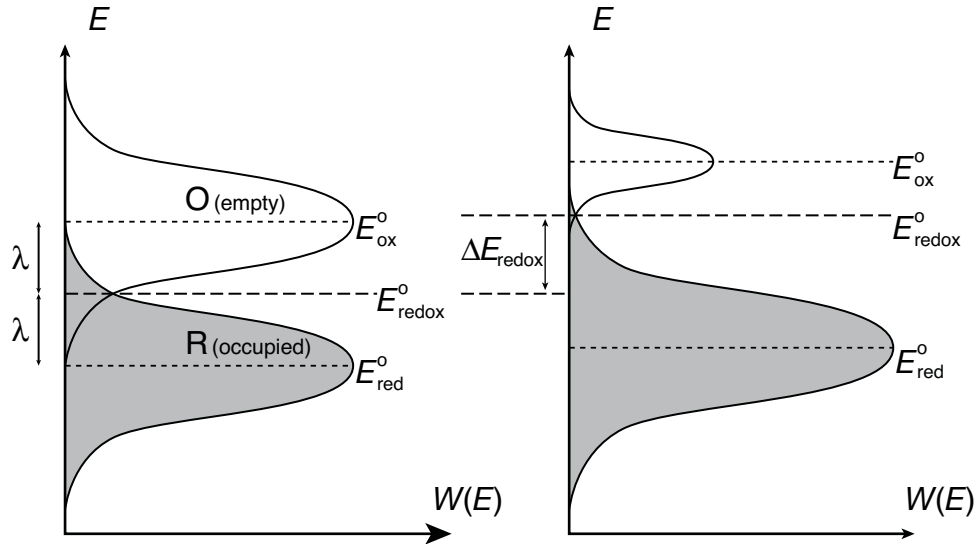
$$D_{ox}(E) = c_{ox} W_{ox}(E) \qquad (2.3)$$

and

$$D_{red}(E) = c_{red} W_{red}(E) \qquad (2.4)$$

where c_{ox} and c_{red} are, respectively, the concentrations of the oxidized and reduced species

and $W_{\mathrm{ox}}(E)$ and $W_{\mathrm{red}}(E)$ are the probability to find an empty (oxidized) state or an occupied (reduced) state. The Gaussian shape of $W(E)$ shows the distribution of electronic levels of the redox system schematically depicted in figure 2.5.

Fig. 2.5: Energy diagram of an electrolyte a) under standard conditions ($c_{\mathrm{ox}} = c_{\mathrm{red}}$) b) $c_{\mathrm{ox}} \ll c_{\mathrm{red}}$. λ is the reorganization energy of the solvatation layer. $\Delta E_{\mathrm{redox}}$ is the variation of the redox potential in function of the concentration given by the Nernst equation, see Eqs. (2.5).

Since the electronic structure is concentration dependent, a change in concentration will lead to a shift in the redox potential (E_{redox}); the Nernst equation describes this:

$$E_{redox} = E_{redox}^{\circ} + \frac{RT}{zF} \ln \frac{c_{ox}}{c_{red}} \Rightarrow \Delta E_{redox}^{\circ} - E_{redox} \tag{2.5}$$

where E_{redox}° is the standard redox potential, ΔE_{redox} the variation, R the gas constant, z the number of electrons involved in the reaction and F the Faraday's constant.

2.1.4 The Semiconductor-Electrolyte Interface

In order to describe the semiconductor-electrolyte interface, the concepts of energy-bands in the SC and probability distributions in the electrolyte, introduced previously, have to be combined. To facilitate understanding the terms that are used to describe both metal-semiconductor and *p-n* junctions (Schottky diode, [23, 133]) will be adapted. The model, called Schottky-model, is based on two assumptions: the doping concentration is homogeneous and the dopants are completely ionized at room temperature under flat band conditions (this term will be defined further down).

The redox potential, E_{redox}, of the electrolyte will be associated with the Fermi level of the electrolyte $E_{\text{F}}^{\text{redox}}$ (where $E_{\text{F}}^{\text{redox}} = e \cdot E_{\text{redox}})^2$. $E_{\text{F}}^{\text{redox}}$ is considered constant or only negligibly variable because adsorbed species are regenerated from the electrolyte at the electrode surface; as the number of charge carriers in the solution is much higher than their concentration in a SC (an electrolyte concentration of 1 M corresponds to 10^{20} carriers/cm^3, a typical SC's doping lies at 10^{14} to 10^{19} carriers/cm^3) this is a continuous process.

When SC and electrolyte are brought into contact, the Fermi levels equalize across the interface. Since the electrolyte's Fermi level is fixed at $E_{\text{F}}^{\text{redox}}$, the Fermi level of the SC (E_{F}^{SC}) will adjust to $E_{\text{F}}^{\text{redox}}$. According to the Gerischer model, the SC's surface band edges ($E_{\text{v,s}}$ and $E_{\text{c,s}}$), which are in direct contact with the electrolyte will be pinned by adsorbed species. However, the bulk band edges, $E_{\text{v,b}}$ and $E_{\text{c,b}}$, are free to move. Therefore a band-bending will occur at the interface.

The adjustment of E_{F}^{SC} to $E_{\text{F}}^{\text{redox}}$ is driven by a charge transfer through the semiconductor-electrolyte interface; this leads to the formation of a SCL in the SC and a counteracting charge in the solution. Depending on the relative positions of the SC's Fermi level and the electrolyte's redox potential, this charge transfer can be from the SC to the electrolyte or vice-versa.

---

2. For simplicity we will be using the term 'redox potential' for $E_{\text{F}}^{\text{redox}}$ even though it is actually an energy.

To illustrate we will be considering the case of a p-type SC[3], whose $E_F^{SC} > E_F^{redox}$ (see figure 2.6a). E_F^{SC} and E_F^{redox} will align at the energy level of E_F^{redox}; as E_F^{SC} had initially a larger value, the SC's bands will be bent upwards at the interface (figure 2.6a) by the value $\Delta\Phi^{\circ}_{SC}$ ($\Delta\Phi^{\circ}_{SC} = |E_F^{SC} - E_F^{redox}|$). This is achieved by a hole transfer from the electrolyte to the SC's valence band, where the charge carriers accumulate and form the SCL; this is situation is therefore called accumulation condition.
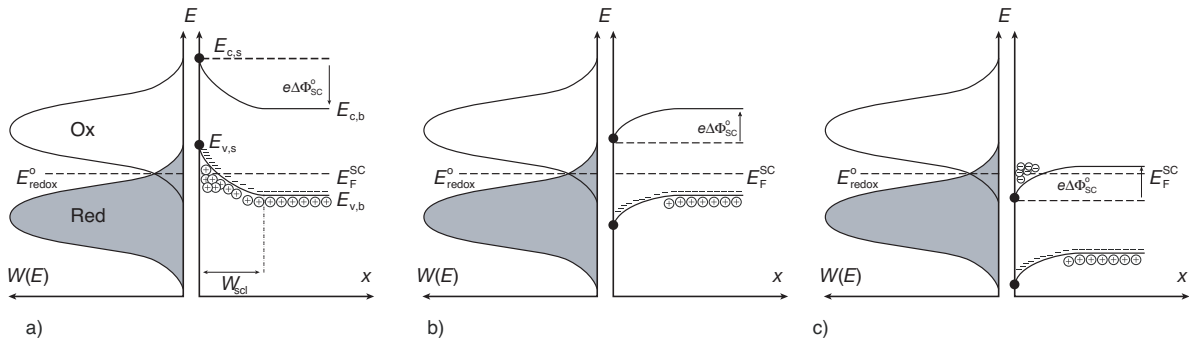
Fig. 2.6: p-type semiconductor in contact with an electrolyte. Different scenarios with no externally applied bias: a) accumulation as $E_F^{SC} > E_F^{redox}$, b) depletion ($E_F^{SC} < E_F^{redox}$), and c) inversion condition. Band edge pinning is illustrated by black circles (●).

In analogy, holes are transferred from the SC to the electrolyte if the SC's Fermi level is superior to the electrolyte's redox potential. As charge carriers are transferred from the SC to the electrolyte the SC is under depletion condition (figure 2.6b). A particular situation occurs when the electrolyte's redox potential is much higher than the E_F^{SC}, if E_C is close to E_F^{redox}, or under externally applied cathodic bias: the surface band edge of conduction band will be lower than E_F^{redox}. Therefore minority carriers (i.e. electrons) will accumulate in the conduction band by charge transfer directly through the conduction band.

---

3. As all our experiments were carried using p-Si, we will only treat the case of a p-doped SC. However, the same formalism with reversed signs (and e⁻ instead of h⁺) can be applied for an n-type SC.

Under the correct external bias, a SC and an electrolyte can be brought into contact without any occurrence of bend-bending; the energy of the electrons is constant from the bulk to the band edges. This potential, called flat band potential, V_{fb}, can be measured experimentally by performing capacity measurements of the SC (more specific a plot of $1/C^2$ vs. the applied bias) as it follows the Mott-Schottky relation [134, 135]:

$$\frac{1}{C_{SC}^2} = \frac{2}{\varepsilon \varepsilon_o e N_D}\left(V - V_{fb}\right)$$
(2.6)

where ε is the dielectric constant, ε_0 the vacuum permissivity, N_{D} the SC's doping concentration, V the externally applied bias, and V_{fb} the flatband potential. By extrapolating $1/C^2$ towards 0, V_{fb} as well as N_{D} can be obtained. These values can in turn be used to calculate the width of the SCL, W_{scl}:

$$W_{scl} = \sqrt{\frac{2\varepsilon \varepsilon_0 \left|V - V_{fb}\right|}{e N_D}}$$
(2.7)

2.1.5 Charge Transfer at Semiconductor Surfaces

If no external bias is applied oxidation and reduction reactions occur at the same rate; in this situation the oxidation current, i_{ox}, and the reduction current, i_{red}, will be equal but of opposite sign, i.e. no current flow can be measured in the system. If however an external voltage, V, is applied, a current will forcibly flow; depending on the sign of the applied potential, this current can be either cathodic or anodic.

Therefore, we need to know the condition of the electric field at the semiconductor-electrolyte interface in order to understand its charge transfer characteristics. It can be said that the potential at the interface, V, is composed of a constant term due to contributions from the reference electrode and an electric field across the interface, $\Delta\Phi$:

$$V = \Delta\Phi + constant$$
(2.8)

$\Delta\Phi$ is the sum of all contributions to this potential drop, caused namely the capacitance due to the SCL, $\Delta\Phi_{scl}$, the contribution of the Helmholtz layer in the electrolyte at the substrate surface, $\Delta\Phi_H$, and $\Delta\Phi_{GC}$, caused by the Gouy-Chapman diffusion layer. These can be described as capacitances aligned in a serial arrangement. Since C_{scl} is much smaller than the other contributions due to the relatively low charge carrier concentration in the SC compared to the electrolyte, we can make the following simplification:

$$\Delta\Phi \approx \Delta\Phi_{scl} - \Delta\Phi_{scl}^{\circ} \qquad (2.9)$$

Formula 2.9 shows that an externally applied bias will only have an influence on the SC's band structure while E^0_{redox} always remains constant. It is therefore possible to predict the effects of an applied bias on the energetic state of the semiconductor-electrolyte interface. As the electrolyte can not adapt its energy levels, an externally applied bias will induce band bending in the SC. For an externally applied cathodic bias and a p-type SC it follows that $E^{SC}_F > E^0_{redox}$ (figure 2.7a). Therefore positive charge carriers (i.e. holes) are supposed to flow from the electrolyte to the SC. Since the electrolyte is not able to yield any holes to the SC, a depletion situation in the SC results. Theoretically no current should flow at all in this situation, in reality a small current, corresponding to the leakage current of this particular diode, is measured.

Figure 2.7b shows the opposite case: an externally applied large anodic bias leads to an accumulation of holes and their flow from the SC to the electrolyte; an anodic current is measured. The third, and for us relevant case shows one possibility for breakdown. Under strong cathodic bias the insulating SCL can break down electrically; this may happen either due to an avalanche breakdown, or by direct tunnelling of electrons.
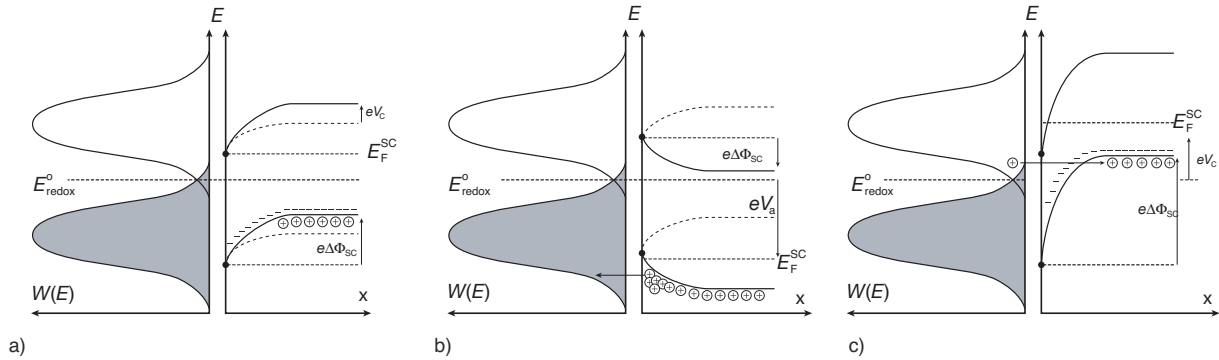
Fig. 2.7: Band diagram for a p-type SC under a) cathodic bias, b) large anodic bias, c) breakdown conditions.

Therefore a p-type SC will behave like a diode: under anodic conditions it conducts current, while the cathodic branch shows a blocking behaviour. The same is true for n-type SC's but the signs are reversed (see figure 2.8). Also, at some point, called breakdown potential, U_{bd}, the blocking behaviour will break down and show conducting behaviour again. This is an irreversible process and the diode is broken once U_{bd} has been reached.
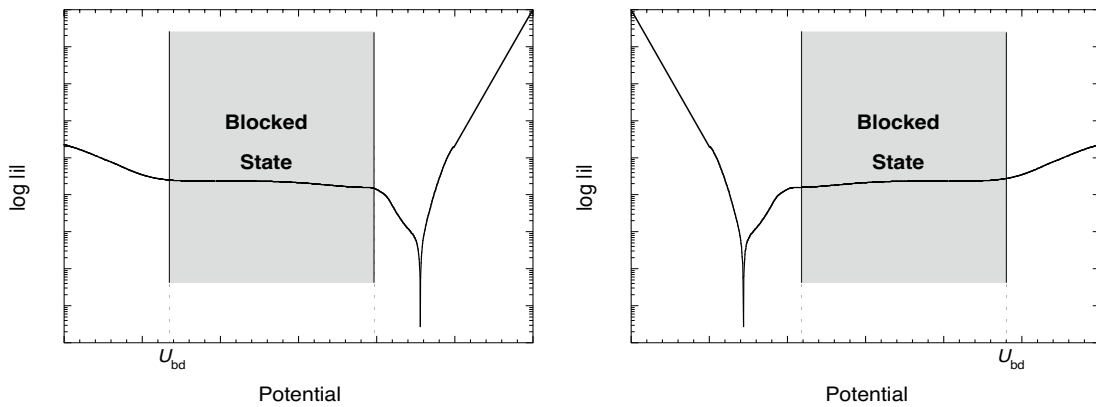
Fig. 2.8: Idealized current-density/voltage curves for left: a p-type SC, right: an n-type SC. The p-type SC exhibits a blocking behaviour for cathodic potentials, while it conducts current on the anodic side; the behaviour is reversed for n-type SCs.

2.1.6 Surface and Bulk Defects and the Semiconductor-Electrolyte Interface

We have seen previously that the semiconductor-electrolyte interface can be compared to a Schottky diode with its current blocking and passing behaviour and its breakdown properties. Breakdown can occur either by direct tunnelling or by avalanche breakdown. In the first case and electron tunnels directly from the valence band through the energy bandgap to the conduction band. Tunnelling usually only occurs at high applied electric fields and for highly doped SCs. In the second case, avalanche breakdown or multiplication, a thermally generated electron gains kinetic energy from the applied electric field. If the field is sufficiently high, the electron can gain enough kinetic energy that, upon collision with an atom, it can break the lattice bonds, creating an electron-hole pair. The newly created electron and hole both acquire kinetic energy from the field and, in turn, create additional electron-hole pairs. This process is therefore called avalanche breakdown. Obviously, breakdown, either by tunnelling of by avalanche multiplication, is facilitated if additional energy states exist in the bandgap, as the initial energy needed to overcome the bandgap is much smaller.

There are different kinds of imperfections present at or near the surface even of an apparently perfect substrate [136] either as donors or acceptors (see figure 2.9). These may include surface defects such as dangling bonds and adsorbed species, as well as crystalline defects in the form of interstitials and kinks. The sites of these defects will be more active (electro-)chemically [50] and electronically [137]. Therefore, a surface which is otherwise clean, will show a different behaviour on different crystal faces, point defects, sites of adsorbed species etc. These 'imperfections' lead to the creation of additional energy levels or bands in the forbidden bandgap of the SC acting as additional doping and thereby facilitate charge transfer [136].

Bulk defects exist too; these include foreign atoms, vacancies, interstitials, and dislocations. All of these introduce new energy levels in the SC in their proximity. If these additional energy levels lie close to either the valence or the conduction band, they may act like dopants and enable charge transfers. Defects close enough to the surface may also act as initiation sites for surface reactions as they allow charge transfer from the SC to the electrolyte while the intact SC surface would not allow for such reactions to occur.
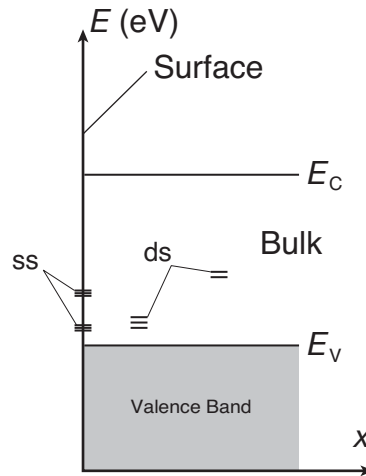
Fig. 2.9: Schematic representation of defect states in a SC. Surface defects lead to additional surface states, designated ss), while bulk defects lead to additional defect states (designated ds).

If enough additional states are present, breakdown of the diode is facilitated as charge carriers can pass more easily through the forbidden bandgap even under depletion conditions due to the new energetic states in the surface. Once breakdown has occurred, charges can flow freely across the interface and enable electrochemical reactions at these defect sites. Therefore, by locally introducing surface defects, it is possible to lower the breakdown potential, U_{bd}, and locally activate the electrode (see gray box in figure 2.10).
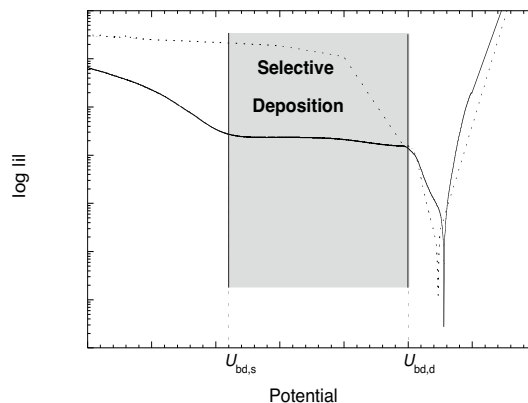
Fig. 2.10: Idealized current-density/voltage curve for an intact (——) and a defective (···) p-type SC. $U_{bd,s}$ denotes the bulk surface breakdown potential, whereas $U_{bd,d}$ is the breakdown potential at defect sites. In the potential range delimited by the gray box selective electrochemical reactions are possible.

2.2 Electrochemical Deposition of Metals on Semiconductors

The deposition of metals on conducting substrates has been studied for a long time due to its technological importance. Over the last thirty- or so years this has been extended to include semiconducting substrates, as chipmaking crucially depends on the ability to metallize SC substrates. In this section we will briefly overview the basic principles governing the deposition –consisting of nucleation and growth– of metals on SCs.

Nucleation and growth mechanisms depend on the interaction energy between the adsorbed metal ion and substrate and the respective lattice spacing of the substrate and the metal to be deposited. As interactions between metals and SCs are often weak, their deposition usually follows a 3D island formation mechanism [52, 138] called Volmer-Weber growth [139]. As the growth characteristics strongly depend on the nucleation and growth mechanism, we will be looking at these in some more detail.

2.2.1 Nucleation of Metallic Clusters

First theories of electrochemical growth of crystals considered the substrate to be perfect on an atomic scale. The problem was that perfect surfaces do not offer nucleation sites; nevertheless, a theory was proposed by Erdey-Gruz and Volmer in 1930 [140, 141]. When it was discovered that surfaces did indeed contain surface defects, acting as nucleation sites [142], new models arised [143-145]. Figure 2.11 shows the steps involved in adding a metal ion to a substrate surface: the solvated metal-ion is adsorbed to the surface; once adsorbed, it will diffuse along the surface until it 'hits' an existing metal cluster (or a surface defect). It will then add itself to the cluster, contributing to its growth.
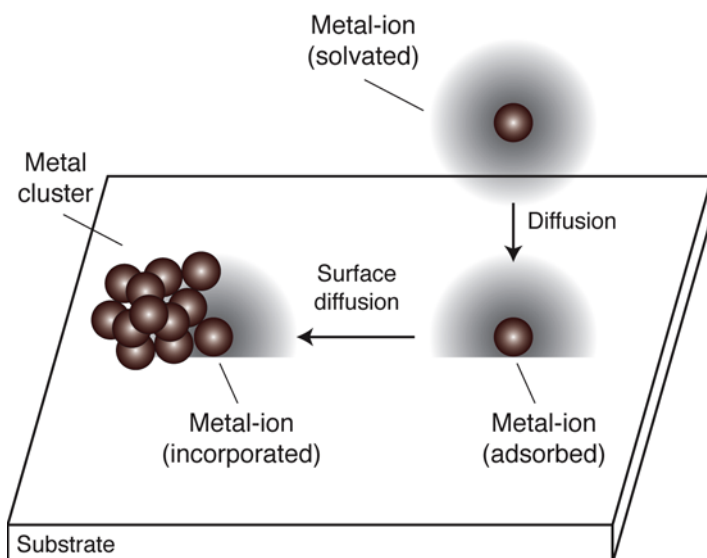
Fig. 2.11: Addition of a metal ion to a crystal surface.

Nucleation mechanisms are described as being either instantaneous or progressive. In the case of instantaneous nucleation all possible nucleation sites give rise to initial nuclei as soon as a potential is applied; all nuclei grow simultaneously (in a 3D fashion) until their respective diffusion spheres overlap. This case is encountered if nucleation rate is high, i.e. all nucleation sites are being used very quickly; nucleation is fast compared to growth. During progressive nucleation, new nuclei are created over time and no distinction can be made between a nucleation and a growth phase. In other words, growth is fast in comparison to nucleation. In the most simple case of progressive nucleation, first order nucleation mechanics are observed, i.e. the number of nuclei increases linearly with time.

Thermodynamics of electrochemical nucleation is similar to that of nucleation from the gas phase. Both cases are based on the fact that nucleation occurs in a supersaturated regime. In the case of electrochemical nucleation, supersaturation can be described in terms of the difference of the electrochemical potential of the bulk metal, $\mu_{M,b}$, and that of the solvated metals ions, $\mu_{M,solv}$. Experimentally, the difference, $\Delta\mu$, can be controlled directly, according to:

$$\Delta\mu = \mu_{M,b} - \mu_{M,solv} = -ze|\eta| \qquad\qquad (2.10)$$

where z is the number of charges transferred, e the elementary charge, and $|\eta|$ the overpotential[4]. In SC electrochemistry, the term overpotential is usually not used since the applied potential is distributed between the SC's SCL, the Helmholtz layer and the Gouy-Chapman diffusion layer (see chapter 2.1.5).

For successful metal deposition the following has to happen: once an ad-ion has adsorbed to the surface, a metallic cluster has to nucleate and to grow. As said above, this only takes place in a supersaturated regime. Even so the nucleus has to reach a critical size until further growth becomes energetically more favourable than dissolution (due to the surface energy of the cluster). This process is governed by the Gibbs free energy for the formation of a cluster of N atoms:

$$\Delta G(N) = -Nze|\eta| + \Phi(N) \qquad\qquad (2.11)$$

where η is the overpotential and $\Phi(N)$ is the energy associated with the creation of new interfaces. While the first term $(-Nze|\eta|)$ is related to the volume, the second term $-\Phi(N)-$ is a function of the surface energy (and therefore depends on $N^{2/3}$). It follows that for small clusters, $\Phi(N)$ is the dominating factor, while for larger ones $-Nze|\eta|$ becomes dominant. The critical cluster size, N_{crit} is reached, when the influence of these two factors are equal, i.e. $d\Delta G(N)/dN = 0$. Allowing for some simplification[5], equation 2.11 can be differentiated with respect to N. It is then possible to determine the dependence of the overpotential on critical cluster size:

$$N_{crit} = \frac{8bV_m^2\sigma^3}{27(e|\eta|)^3} \qquad\qquad (2.12)$$

where b is a shape-dependent constant (36 for spheres), V_m the atomic volume, and σ the specific surface energy. According to formula 2.12 N_{crit} strongly depends on η, the overpotential.

---

4. Note that η is negative for metal deposition.
5. $\Phi(N)$ is dominated by the surface energy terms and an arbitrary 3D shape of the cluster is assumed.

Now that critical cluster size has been determined, kinetic considerations become impor-
tant. The nucleation rate, J_{nucl}, is given by the Volmer-Weber equation [139]:

$$J_{nucl} = A_{3D} \exp\left(-\frac{\Delta G_c}{kT}\right)$$
(2.13)

where A_{3D} is shape dependent and can be considered to be potential-independent. By sub-
stituting ΔG_C with equation 2.14 it is possible to obtain equation 2.15.

$$\Delta G_c = \frac{4bV_m^2\sigma^3}{27(e|\eta|)^2}$$
(2.14)

leads to:

$$\frac{d\ln(J_{nucl})}{d|\eta|} = -\frac{1}{kT}\cdot\frac{d\Delta G_c}{d|\eta|} = \frac{e}{kT}N_{crit}$$
(2.15)

Experimentally, the nucleation mechanism can be determined using potentiostatic cur-
rent-time transients. By applying a potential-step from a potential with negligible cluster
formation rate to a fixed overpotential, the nucleation and growth of metallic clusters can be
monitored directly analysing the current. The density of nuclei as a function of time, N(t), is
usually described in terms of a linear growth law with a nucleation rate constant, A_n:

$$N(t) = N_\infty\left[1 - \exp(-A_n t)\right]$$
(2.16)

where N_∞ is the final density of nuclei. Two limiting cases are interesting when discussing
equation 2.16: if A_n is large enough for $A_n t \gg 1$, all clusters form very quickly as N(t) = N_∞
even directly after the pulse has been applied; this case is called instantaneous nucleation. On
the other hand, if A_n is small enough for $A_n t$ to be close to 0 even for a large t, it follows that
$\exp(-A_n t) \approx A_n t$ and therefore N(t) = $N_\infty A_n t$; we then speak of progressive nucleation. The
limiting factors for the growth of the nuclei can be controlled, by kinetics, diffusion, or by
intermediate states. In situations where deposition occurs, the overpotential is generally
large and diffusion of ions to the surface can be assumed to be the limiting factor. Only for

very short timescales kinetic limitations may be encountered. In the diffusion limited case, the diffusion spheres of individual nuclei will begin to overlap as they grow, leading to linear diffusion to the surface. In this case –which corresponds to a progressive nucleation– the individual and combined diffusion fields may have a shielding influence on other, smaller nuclei on the surface.

2.2.2 Growth of Metallic Clusters

The growth rate of a nucleus is determined either by the lattice incorporation step or by the diffusion of ions from the solution to the nucleus[6]. In the first case (i.e. in the early stages of nucleation when diffusion spheres do not yet overlap) and assuming a 3D hemispherical growth process, the growth rate, i, is given by:

$$i = \left(\frac{zFk_{\mathrm{r}}^{3} 2\pi M^{2}}{\rho^{2}} \right) \cdot t^{2} \tag{2.17}$$

where M is the molecular weight, and ρ the density of the deposit. Similar models exist for 2D cylindrical growth processes, the main difference being that they depend linearly on the time, t.

In practical applications, nucleation and growth of nuclei usually happens at the same time and therefore more complex models have to be used:

$$i = \left(\frac{zF\pi M h_{\mathrm{n}} A k_{\mathrm{r}}^{2}}{\rho} \right) t^{2} \cdot \exp\left(-\frac{\pi M^{2} A k_{\mathrm{r}}^{2} t^{3}}{3\rho^{2}} \right) \tag{2.18}$$

The exponential term represents overlap and can be ignored if nuclei grow independently (i.e. on a surface with a very low defect concentration or very early after the potential has been applied). For the formation of a monolayer (either by instantaneous or by progressive nucleation) the reduced current-time transients of figure 2.12 left will be observed. In practical applications a multilayer is usually formed. This can happen either by a the repeated for-

---

6. It is assumed that the charge transfer at the nucleus-electrolyte interface is fast and can be neglected.

mation of monolayers on top of one another or, more likely, by multinuclear multilayer growth. In this case many 'monolayers' are formed simultaneously and at different levels, and the resulting current-time transient is the sum of many individual monolayer-transients (figure 2.12 right).
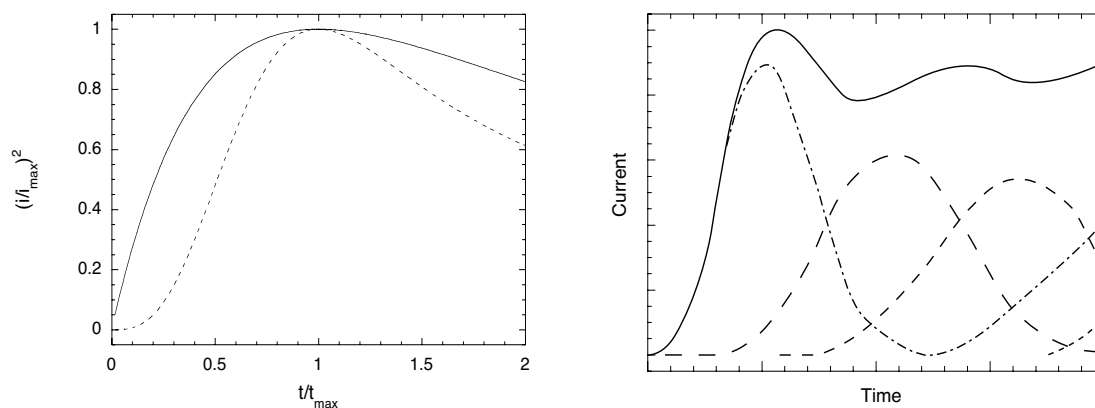
Fig. 2.12: Idealized current-time transients for instantaneous (——) and progressive (···) nucleation; left: formation of a monolayer, right: progressive 2D-nucleation (both according to [146]).

2.2.3 Formation of a Coherent Deposit

Up to now we have only been considering the formation of mono-atomic layers, or of multilayers comprised of only a few such mono-layers. In practical applications these cases are often irrelevant as massive coherent deposits are desired. These can grow by two distinct mechanism, namely either by layer growth or by growth of 3D crystallites (nucleation followed by coalescence of nuclei). In the first case, crystal growth progresses by lateral spreading of discrete layers and one layer forms after the other. In the latter case, individual 3D crystallites appear as islands (nucleation) and grow on the surface until they join one another (coalescence) to form a coherent massive deposit. Due to the strong dependence of nucleation and growth on the applied overpotential, the growth mechanism also depends strongly on η.

2.3 Ion Beam Lithography

2.3.1 Historic Overview

The interaction of charged particles with solids has been of interest to the scientific community for more than a hundred years. Every since the discovery of radioactivity, there was interest in how these particles were slowed down and eventually stopped when traversing matter. The first publication in the field was by M. Curie, where she stated, that 'alpha particles are projectiles composed of matter and will therefore be slowed down when traversing matter' [147]. However, it was not until a basic understanding of the atomic structure was established, that it became possible to understand or even predict the behaviour of particles in matter, specifically the '*Stopping and Range of Ions in Solids*' [148]; this book by Ziegler *et al.* is still *the* treatise of the field and most of what follows is derived from there.

Once it was understood that ions are charged particles and that atoms consist of a positively charged core surrounded by negatively charged, shielding electrons, it became possible to integrate other theories such as Thomson's treatment of scattering of two point charges [149]. When Bohr published his analysis of how charged particles were stopped by matter, he already used the model of an atom to illustrate his ideas [150, 151]. His work was the first attempt at creating a unified theory of stopping and illustrates well the problems such a theory must overcome: How does a charged particle (point charge) lose energy to the quantized electron plasma of a solid (inelastic energy loss)? This is complicated by the fact that the interaction simultaneously distorts the electron plasma (target polarization) and that the interaction is not between a charged point and the plasma but by a finite and moving atom and a plasma. Furthermore, the degree of ionization has to be estimated for the moving ion while it is moving within an ionized electron plasma. Also, screened Coulomb scattering of the moving atom with each target nucleus it passes has to be taken into account and relativistic corrections have to be included.

One of Bohr's original conclusions was that charged particles passing through solids loose energy by two distinct mechanisms, namely nuclear stopping (due to the medium's atomic cores) and electronic stopping (caused by the medium's light electrons). He concluded that electronic stopping would be dominant for energetic light particles (such as the

ones emitted from radioactive sources) and nuclear stopping for slower heavy ions. He also introduced the atomic structure into stopping theory by giving target electrons orbital frequencies.

The next breakthrough occurred when Bethe [152, 153] and Bloch [154, 155] treated the problem under quantum mechanical considerations and derived in the Born approximation the fundamental equations for stopping of very fast particles in a quantized electron plasma. For fast particles (10 MeV to 2 GeV) this remains the basic approach up to today[7].

The discovery of nuclear fission and the resulting heavy particles renewed interest in the subject. The problem presented by these heavy ions was how to treat the fact that they were partially stripped. It was hoped that if the degree of ionization of the projectile could be estimated, the earlier findings could be applied. Bohr suggested that –based on the Thomas Fermi atom– the ion could be considered stripped of all electrons with energies lower than the ion velocity [156, 157]. Others tried to apply similar ideas with limited success and most of these relationships could only be used to scale data obtained from light ions to heavier ones.

In the 1950's papers evaluating both the energy transfer from slow particles to quantized electron plasmas and the energy loss to target nuclei were published. Lindhard *et al.* published a paper [158] which has been widely used as the basis for calculating the electronic stopping of ions in matter [159-162].

The problem of energy loss to a target nucleus can be summarized as the study of screened Coulomb collisions between two colliding atoms. Bohr used the Thomas Fermi model to estimate the screened Coulomb potential, $V(r)$, between atoms [163]:

$$V(r) = \frac{Z_1 Z_2}{r} \exp\left(-\frac{r}{a}\right)$$
(2.19)

where Z_1 and Z_2 are the atomic numbers of the two atoms involved, r their separation and a a 'screening parameter'.

---

7. For higher energies relativistic aspects have to be taken into account.

For *a* Bohr suggested the following approximation:

$$a = \frac{a_0}{\left(Z_1^{2/3} + Z_2^{2/3}\right)^{1/2}} \qquad (2.20)$$

Others have used numerical techniques to tackle the problem and Firsov suggested the following relationship for calculating the Thomas Fermi screening function [164, 165]:

$$a = \frac{a_0}{\left(Z_1^{1/2} + Z_2^{1/2}\right)^{2/3}} \qquad (2.21)$$

To calculate the degree of ionization of the ion as it passes through matter Bohr and others suggested, that the ion would loose electrons whose orbital velocities would be less than the ion velocity. To calculate the ion charge fraction, Z^*/Z, the following approximation could be used:

$$Z^*/Z = \frac{v}{v_0 Z_1^{2/3}} \qquad (2.22)$$

2.3.2 Interactions of Ions with Solids

Interactions between an incident ion and the substrate can be divided into two mechanisms: if collisions occur with the target nuclei one speaks of nuclear stopping, if they occur with the electrons it is called electronic stopping. In the first case the energy of the incident ion is transferred to a static atom as a whole (which may in the process be moved from its original position in the crystal) whereas in the case of electronic stopping target electrons may be excited or ejected (i.e. the target may become ionized). Since both effects are independent from one another we can divide the energy loss of an ion, dE, per distance, dx, into an electronic (e) and a nuclear (n) part:

$$\left(\frac{dE}{dx}\right) = \left(\frac{dE}{dx}\right)_e + \left(\frac{dE}{dx}\right)_n \qquad (2.23)$$

Depending on the projectile's energy, mass, and charge as well as the target composition either mechanism may be dominant. In general it can be said that at low ion energies nuclear energy loss is predominant while electronic stopping prevails at higher energies. At low energies ($0.1 v_0 < v_{ion} < Z^{2/3} v_0$, where v_0 is the Bohr velocity) electronic stopping is proportional to the ion velocity; the ion carries its electrons and tends to be neutralized by electron capture. For higher energies ($v_{ion} >> Z^{2/3} v_0$) the ion becomes fully stripped and the energy loss, dE/dx, is proportional to the charge of the ion. According to the Bethe-Bloch formula [152, 154, 166]:

$$\frac{dE}{dx} = N Z_2 \left(\gamma Z_1 e^2 \right)^2 f\left(v_1^{-2} \right) \tag{2.24}$$

where N is the substrate atom density, γ the effective charge parameter, Z_1 and Z_2 the atomic number of ion and target respectively, e the elementary charge and $f(v_1^{-2})$ a fitting function depending on the substrate material.

At intermediate velocities, the ion is only partially stripped and the charge of the ion can not be obtained straightforward. In the literature different formulations are presented to calculate the effective charge γZ_1 for ions at these velocities [148, 167-170].

dE/dx is called the stopping power, $S(E)$; by including the atomic density, N, the stopping cross section, $\varepsilon(E)$, can be obtained according to:

$$\varepsilon(E) = \frac{S(E)}{N} \tag{2.25}$$

Stopping powers and cross section can now be obtained easily by computer simulation (e.g. TRIM [167, 171]). The ion range, R_t, i.e. the total path length an incident ion covers in the target material, is defined as:

$$R_t = \int_{E_0}^{0} \frac{1}{S(E)} dE \tag{2.26}$$

where E_0 is the energy of the incident ion. In practical applications, the projected range, R_p, is usually used instead of R_t; R_p is the actual penetration depth of the ion into the material. As incident ions will randomly collide with the target material, they will not follow a

straight path into the target but will deviate in all directions; this behaviour is called straggling and can be simulated: figure 2.13 shows straggling in both y and z direction parallel to the substrate's surface.
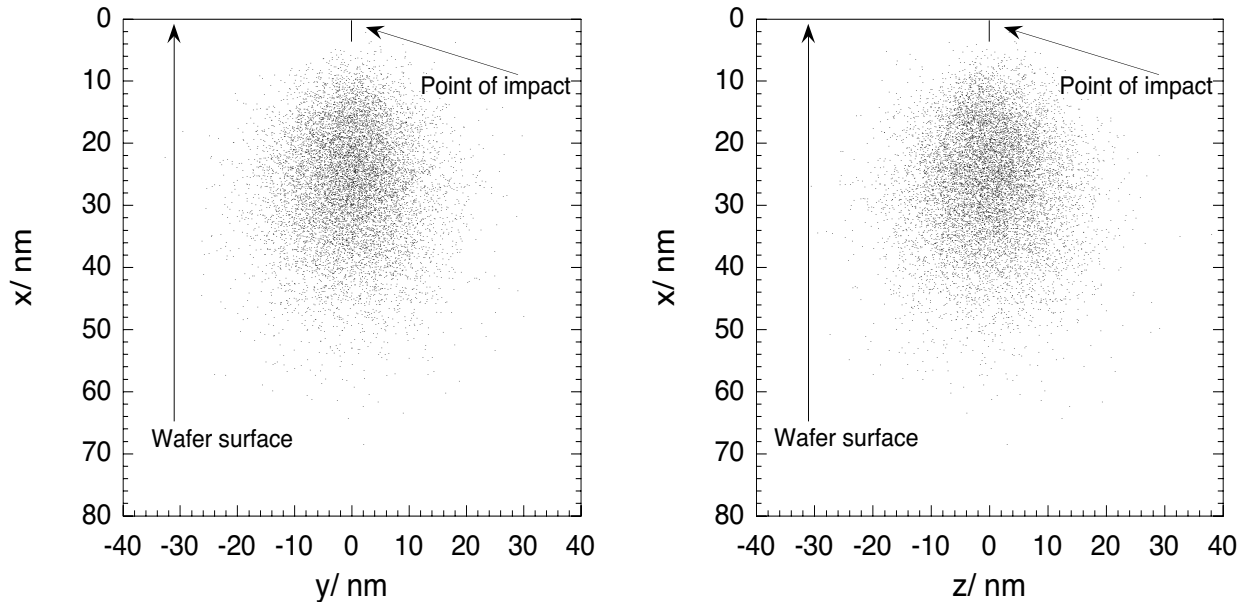
Fig. 2.13: Straggling of Ga^+ ions in a Si substrate in y and z direction –x being the beam direction; energy 30 keV, angle of incidence 0° (all calculations performed using SRIM-2000 code and 10'000 impinging ions).

2.3.3 Defect Creation by Ion Beams

Ion implantation not only introduces foreign atoms into the target material, but they also create defects. Due to their high energy, the impinging ions may be energetic enough to displace target atoms from their lattice sites, creating interstitials and vacancies in the process. If enough energy is transferred from the ion to the lattice atom, it may displace further target atoms, leading to a cascading displacement reaction which may involve several hundred to thousand atoms. After roughly 10^{-13} s the incoming ion will be completely stopped. Once the kinetic energy is no longer sufficient to displace target atoms, the remaining energy will be dissipated by creating lattice vibrations, i.e. phonons, in the target leading to a thermal spike in its direct vicinity [172, 173]. This process is fast and the excess heat is dissipated at a rate of $\approx 10^{14}$-10^{15} K/s [174, 175].

According to Kinchin and Pease –using a model based on solid spheres– the number of displaced target atoms N(E) is given by [176]

$$N(E) = \frac{E}{2 \cdot E_d} \qquad (2.27)$$

where E is the ion energy and E_d the energy needed to create a stable Frenkel pair (for Si $E_d \approx 25$ eV [177]). By using a more realistic atomic model, Sigmund finds for N(E) [178]

$$N(E) = \frac{\xi v(E)}{2 \cdot E_d} \qquad (2.28)$$

where $\xi < 1$ is a function of the scattering potential and $v(E)$ is the part of the ion's energy not used for electronic stopping. Using the same computer code as before, the stopping mechanism of the incident ion (figure 2.14) as well as the distributions of various defects (vacancies, interstitials) and of the implanted ions (figure 2.15) can be calculated as a function of the energy, the incident ion, the substrate, etc. Figure 2.14 shows how nuclear and electronic stopping are influenced by the incident ion's mass and energy.
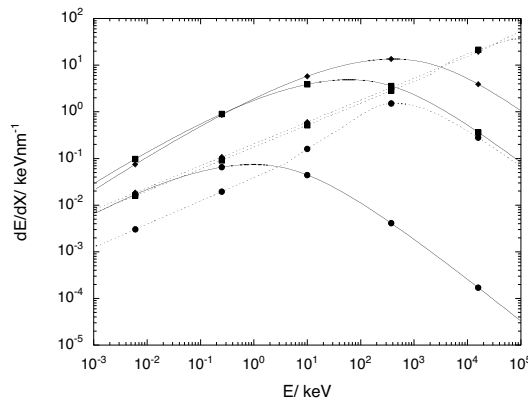
Fig. 2.14: Electronic ($\cdots$) and nuclear (——) stopping cross sections of He ($\bullet$), Ga ($\blacksquare$), and Au ($\blacklozenge$) ions in silicon (all calculations performed using SRIM-2000 code [171]).

The following observations can be made with respect to figure 2.14:

- At low energies, nuclear stopping is dominant; at high energies, electronic stopping becomes the important factor.
- The heavier the ion, the more important the stopping powers become; i.e. heavier ions do get stopped earlier in the substrate
- The heavier the ion, the longer nuclear stopping remains the dominant factor.

These findings have to be considered when using ion beams for different applications: sputtering for example depends on nuclear stopping, i.e. heavy ions at low energies may be preferable. If an ion beam is used to expose polymeric resists, electronic stopping is needed in order to break bonds within the resist-molecules; light ions are therefore preferable.

Figure 2.15 shows the distribution of various defects induced by incident ions in a Si crystal. These calculations are important in order to understand the electrochemical changes caused by the ion bombardment. As it has been explained before, imperfections in the crystal lead to additional states in the bandgap and may facilitate charge transfer from the conduction to the valence band. However, for electrochemical reactions to be easily possible at the substrate surface, these defects need to lie within rather close distance of the surface.
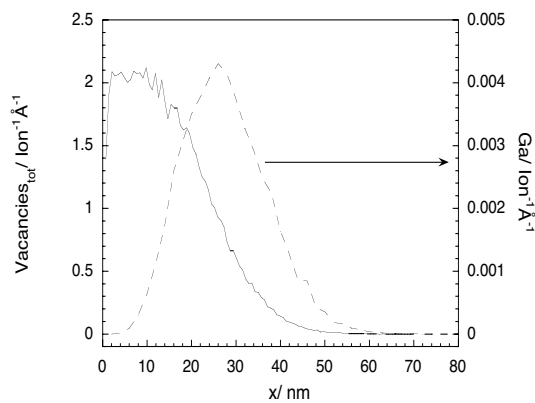
Fig. 2.15: Distribution of vacancies (——) and implanted Ga^+ ions ($\cdots$) in Si after 10'000 impinging Ga^+ ions at 30 keV (all calculations performed using SRIM-2000 code).

According to figure 2.15 mainly vacancies are created by the incident ions. We have there-
fore plotted the influence of ion energy and ion type on the depth distribution of the vacan-
cies created (figure 2.16).
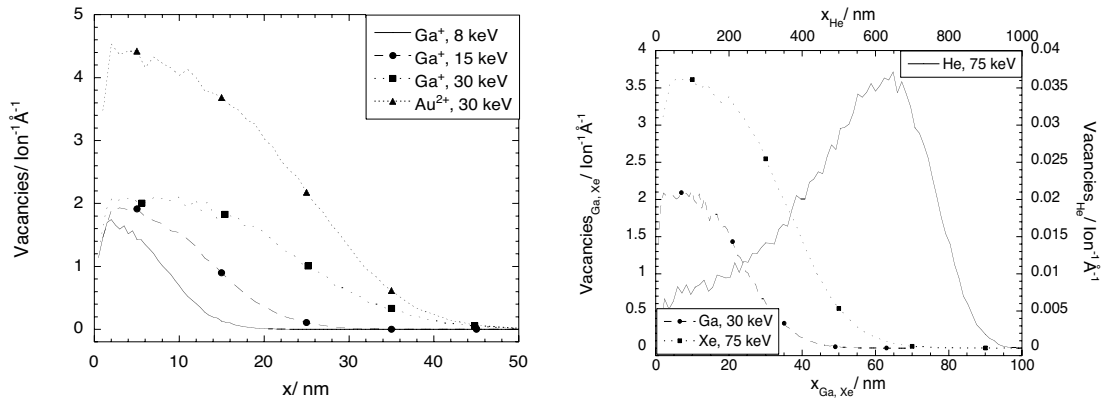
Fig. 2.16: Distribution of vacancies for various implanted species at various energies in Si. The left figure shows
Ga$^+$ions at varying energies as well as Au^{2+}ions at 30 keV; the right figure shows He$^+$ and Xe$^+$ions at 75 keV as
well as Ga$^+$ions at 30 keV (all calculations performed using SRIM-2000 code and 10'000 impinging ions).

Figure 2.16 shows that heavier ions create more damage and that the damage lies closer to the
substrate surface. We can therefore assume that heavier ions need lower doses than light ions
to achieve the same effect for electrochemical sensitization. Also, it seems that lower ener-
gies may be preferable as defects should lie closer to the sample surface and therefore the
perturbations they introduce into the crystal structure (and the additional energy levels)
should extend to the substrate surface.

The results presented are all based on static models, i.e. changes in the substrate's crystal-
line structure due to defect accumulation or heating effects are not taken into account. At
low temperatures all the defects are immobile and accumulate. Therefore, a certain critical
dose, D_{crit}, exists beyond which the target becomes fully amorphous. Higher temperatures,
either due to target heating or due to very high ion fluences may lead to an increased mobil-
ity; defects can recombine and may be 'healed' over time. At elevated temperatures (or very
high current flux) D_{crit} may therefore be higher or not be reached altogether [179].

According to Gibbons [180, 181] an incident ion creates an amorphous zone of cylindric shape with a diameter $\sigma_0 = \pi \cdot R_0^2$ (values for σ_0 can be calculated [182]). The change of the degree of amorphization df_a during a time interval dt is then given by:

$$\frac{df_a}{dt} = (1 - f_a) \cdot i \cdot \sigma_0 \qquad (2.29)$$

where f_a is the degree of amorphization ($0 < f_a < 1$) and i the current density. The term ($1 - f_a$) assures that an area that is already amorphous will not be 're-amorphised' if it gets hit again by an ion. f_a can be calculated according to

$$f_a = 1 - \exp(-i \cdot \sigma_0 \cdot t) \qquad (2.30)$$

This model can be further refined for systems where the incident ion is not heavy or energetic enough to amorphize the substrate with one 'hit'. For the case where n impinging ions are needed to fully amorphize the substrate, the following formalism can be used:

$$f_a = 1 - \left(\sum_{k=0}^{n-1} \frac{(\sigma_0 \cdot \Phi)^k}{k!} \cdot \exp(-\sigma_0 \cdot \Phi) \right) \qquad (2.31)$$

According to formula 2.30 and 2.31, the degree of amorphization increases with the current density; but if the implant ion dose, d, remains constant, so does the product $i \cdot t$ as well as f_a. However, for high current densities the probability for two impinging ions to 'hit' the same zone in a given interval of time increases. If the time between two ions hitting the same area is short enough the two ions will behave as one; high current densities will therefore rather decrease than increase amorphization of the substrate.

a) Sputtering vs. Implantation

In the previous paragraphs different damage creation mechanisms were discussed. To clarify we will briefly summarise our previous description:

- The stopping mechanism of ions in solids can be divided into two distinct categories: electronic and nuclear stopping.

- Electronic stopping is predominant for high ion energies and for light elements. The incident ion is stopped by elastic scattering at the target atom's electrons. The target atom may become excited or even ionized, chemical bonds may be broken; this effect is used in ion beam based lithography systems (see chapter 1.2.2, a).

- Nuclear stopping is predominant for lower energies and heavier elements. The incident ion is stopped by elastic collisions with the target atom's nuclei. These collisions may cause different kinds of defects.

- If enough energy is transferred to the target atom for it to completely leave its previous position in the crystal lattice, a vacancy in the crystal results. If the target atom was part of or close to the target's surface, it may even be ejected entirely from the target. In this case one speaks of sputtering and mass is effectively removed from the substrate (especially if the incident ion bounces back as well).

- If the target atom leaves its initial position but not the target (e.g. because its energy was insufficient to reach the target's surface or because it was displaced in an angle parallel to the surface) a vacancy-interstitial pair is created. The result is a defect in the crystal structure, introducing some amount of strain.

- If the incident ion does not 'bounce' off the surface, it will also be implanted into the target where it will act as an interstitial, i.e. it will occupy a position in the crystal lattice normally not occupied by atoms. In this case, additional strain is introduced into the crystal.

- If enough defects accumulate in the crystal (vacancies and interstitials), long term order of the crystal breaks down and one speaks of an amorphous state.

- As the incident ions are highly energetic, they may collide multiple times and transfer enough energy to the target atoms for them to create further damage. Therefore, one speaks of a defect cascade. This defect cascade may involve several hundred or thousand target atoms for a single incident ion.

Chapter 3

EXPERIMENTAL

This chapter provides a brief overview of the techniques and equipment used for our work. We begin by describing sample preparation, followed by a short description of the FIB and ion beam tools used, continue by presenting the electrochemical techniques employed and finish with different surface analytical techniques.

3.1 Sample Preparation

All experiments were carried out on p-type Silicon(100) with a resistivity of 1-10Ωcm; the wafers were polished on one side, had a thickness of 500 µm and were purchased from WaferWorld Inc. For implantations carried out at the Fraunhofer Institute for Silicon Technology (ISiT) equivalent wafers were used. Wafers were cleaved into samples roughly 1 x 1 cm^2.

Samples were degreased prior to ion implantation and electrochemical experiments by subsequent sonication in acetone, isopropanol, and methanol, followed by a rinse in deionised water; they were blown dry with argon or nitrogen. To remove any native oxide and to obtain a H-terminated surface [183, 184], a HF 1 % dip was performed for 1 min, followed by another rinse/dry cycle; this was also done prior to ion implantation and electrochemical experiments. To obtain an ohmic back-contact for electrochemical DC experiments, InGa eutectic (99.99%) was smeared on the back side of the wafer; for AC measurements, Al coated samples were used (Al layer −1 µm− was deposited by e-beam evaporation, followed by an annealing at 400 °C in reducing atmosphere for 15 min).

Scratched samples were scratched using a Leitz micro-indenter Durimet IC. Scratches were applied over a length of 1 mm and with a force corresponding to an applied weight of 5 g. The sample was placed under the diamond and moved against the stationary indenter.

3.2 Ion Beam Tools

Different ion beam tools were used during our work: a FIB, a broad-band ion implanter, and an ion projection lithography tool. The main features of these machines are described in the following section.

3.2.1 Focused Ion Beam (FIB)

Due to the development of the liquid metal ion source (LMIS) in the early 1960's probe sizes of less than 10 nm and current densities of more than 100 A/cm^2 are now available, which make these beams suitable for many applications. When compared with optical lithography systems the advantage of FIBs is that the beam's resolution, r_m, is not limited by the wavelength, λ, of the incident beam as given by Rayleigh's equation:

$$r_m = 0.4 C_S^{1/4} \lambda^{3/4} \qquad (3.1)$$

where C_s is the spherical aberration of the lens due to imperfections. Unfortunately, problems associated with ion optics, a lack of suitable resist systems, and the general trend in the semiconductor industry to 'never change a winning team' (in this case photolithography) have so far impeded the introduction of such systems into larger scale applications.

A FIB system and a scanning electron microscope, or rather an electron beam lithography tool, are similar in many respects (see figure 3.1). In order to be able to focus an ion beam onto a surface smaller than 100 nm^2, a point ion source is needed. In most cases a liquid metal or liquid alloy ion source (LMIS/LAIS) is used for particle generation[8]. A fine tungsten tip (tip radius ~1-10 µm) onto which a droplet of the metal/alloy is deposited acts

---

8. Gaseous field ionization sources are also used (for the generation of gas ions); however, as our system was equipped with a LMIS, we will be limiting our attention to these.

as emitter. During operation of the FIB system, the tip is electrically heated to liquify the metal[9]. A source material with high surface tension and low vapour pressure is desirable. An extraction electrode is placed in front of the tip and a potential of 4 - 7 kV is applied between the two. The surface tension in the metal droplet and the force of the applied electric field counteract each other and lead to the formation of a fine cone of liquid metal –with a typical half angle of 49.3 deg and a tip radius of some 10 nm– called Taylor cone [185]. At the tip of the Taylor cone ions are emitted by field ionisation. A LMIS is characterized by its brightness B:

$$B = \left(\frac{\mathrm{d}^2 I}{\mathrm{d}A \cdot \mathrm{d}\Omega} \right) \qquad\qquad (3.2)$$

where $\mathrm{d}I$ is the differential current element emitted from an infinitesimal source area, $\mathrm{d}A$, into an angle $\mathrm{d}\Omega$. A typical value for a LMIS is around $10^6 \, \mathrm{A/cm^2 \, sr}$ [66]. Next to the brilliance, energy spread in the beam is the most important parameter for good spatial resolution. It is caused by the ionization process itself and amounts to roughly 5 to 25 eV.

The ion optical column is similar to that of an e-beam lithography tool, with the main difference being that ions are used instead of electrons. Cations are emitted across the extraction aperture and accelerated up to 30 keV on their way to the condenser lens. The beam is then collimated and passes the blanker, where a field can be applied to divert the beam into the wall of the vacuum tube. The stigmator allows to control the shape of the beam. After the aperture an E x B field (Wien filter) can be used in conjunction with the mass separating aperture to select ions of a desired mass/charge ratio; this allows for the selection of well defined ionic species even if a complex alloy ion source has been used originally. For metal ion sources neither the Wien filter nor the mass selecting aperture are needed. Therefore a crossover of the beam is avoided, leading to a better resolution. The x/y scanning unit is computer-controlled and deflects the beam to write previously defined patterns. At the objective lens the final focalisation onto the sample surface takes place. Close to the sample

---

9. For metals with high melting points, alloys are used. This prevents excessive heating of the tip, which would lead to more wear (intermetal corrosion between tungsten tip and alloy) and an increased scattering of the ions.

surface a secondary electron detector collects electrons generated by the impinging ion beam; the secondary electron image is used for fine positioning and focusing the beam on the sample. In some systems (dual beam set-up) an additional e⁻-gun is placed close to the sample, this allows to monitor changes on the sample surface while sputtering.
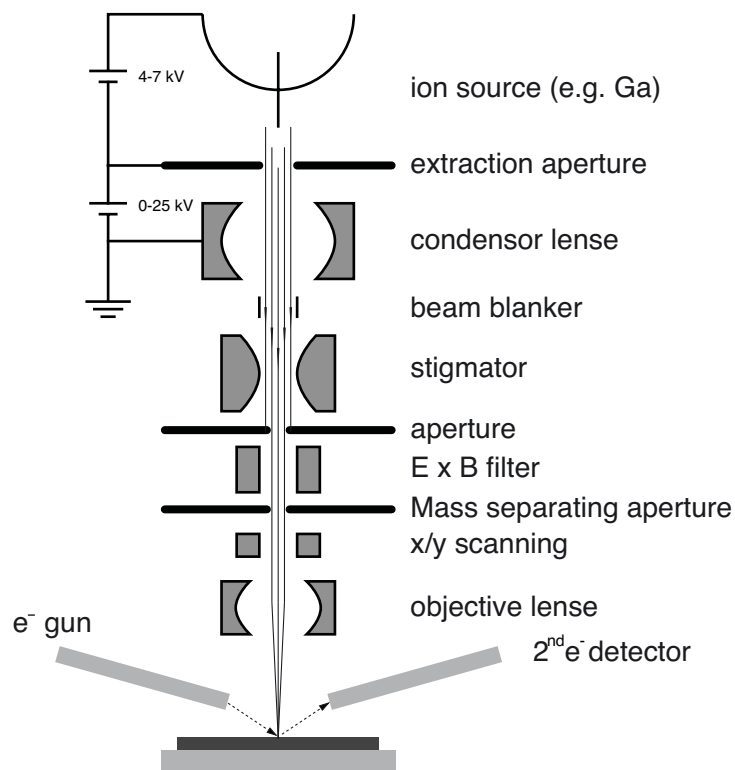

Fig. 3.1: Schematic representation of a FIB system

For the current work a single beam Raith-Orsay Physics FIB –installed in the cleanroom of the Laboratory for Micro- and Nanotechnology (LMN) at the Paul-Scherrer Institute (PSI) in Villigen, Switzerland– was used for the implantation of both Au^{2+} and Ga^+ ions.

The Raith-Orsay Physics FIB is a versatile single beam machine, equipped with a LMIS. Most experiments were carried out with a Ga-ion source produced in-house and operating slightly above room temperature[10]. Between the LMIS and the extraction aperture a poten-

---

10. Some preliminary experiments were carried out using a Au-Er-Si ion source, out of which the Au^{2+}-ions were selected.

tial of 4-7 keV was applied. Since a mono-atomic ion source was used, the ExB filter as well as the mass-separating aperture were not used; this allowed to work in parallel mode (no second cross-over in the beam) leading to slightly enhanced resolution.

The beam passes a computer-controlled deflector that allows to scan the beam over the surface; the maximum writing field is roughly 180 µm at 30 keV and correspondingly higher for lower acceleration voltages. A stigmator can be used to correct aberrations in the beam shape by use of an octupol field. The system is also equipped with a blanker that allows to deflect the beam away from the sample surface in some 100 ns. Close to the sample surface a secondary electron detector is installed to yield an image similar to a SEM image −if the beam is *scanned* over the surface. Beam-current measurements (needed to calculate the ion dose) were performed by directing the ion beam into a Faraday cup[11] connected to a Keithley nano-amp meter.

Fig. 3.2: Picture of the Raith-Orsay Physics FIB-tool

Figure 3.2 shows the entire Raith-Orsay Physics FIB tool. On the left are the vacuum controllers, the heating- and the beam-deflector unit, and the high-voltage equipment needed for the beam acceleration (1). Next follows the FIB-tool, mounted on a vibration-absorbing table (2); the ion-beam column is visible at the top. Partially covered is the sample-stage con-

---

11. A Faraday cup is an opening deep and narrow enough for secondary electrons not being able to escape, thereby not falsifying the current measured.

trol unit, the PC, and the beam control panel (focus, magnification, current, acceleration, etc.) (3). Next follows the SEM-imaging unit (4) and finally the computer controlling the sample stage and the beam deflection (5).

3.2.2 Plasma Source Ion Beam Systems

Unfocused plasma ion sources (PIS) are mainly used for the doping of large wafer surfaces; if used in conjunction with a stencil mask, one speaks of ion projection lithography (IPL) [8], which is one possible competitor for sub 100 nm lithography applications. As IPL uses a mask for pattern reproduction it offers the advantage of large sample throughput (up to several cm^2 are irradiated with one 'shot'), but is less flexible in its applications. When used in conjunction with a photoresist, patterns of 50 nm have been exposed [8]. A more recent approach is to use IPL for direct surface modification, e.g. for the production of structured magnetic storage devices [99].

While a FIB system can be compared to an e-beam lithography tool, IPL is analogous to 'traditional' photolithographic equipment. Instead of a photon source, a PIS is usually used to project the desired pattern from a mask directly onto the substrate. Due to the particular nature of the ions, a stencil mask has to be used. In order to obtain good resolution, it is imperative that the axial energy spread of the beam be minimized. Recently, multicusp ion plasma sources (MIPS) have been produced, which offer a large volume of uniform and quiescent plasma with minimal axial energy spread [186, 187]. For this reason, they are suitable for the generation of single or multi ion beamlets for lithography applications.

MIPS use permanent magnets of alternating polarity to produce a multicusp magnetic field. Magnetic filter rods reflect high energy electrons so that ion production occurs mainly in a region with uniform plasma potential and the extracted ion beam will have a low axial energy spread below 2 eV [188]. The broad ion beam from the source is accelerated to 30 - 70 keV, penetrates an open stencil mask, and the resulting image is demagnified 4 to 8 times by an electromagnetic lens system onto the sample (figure 3.3). The demagnification of the mask image allows the use of masks with slightly larger features, making them more affordable. Obviously, these systems are limited to gaseous species.
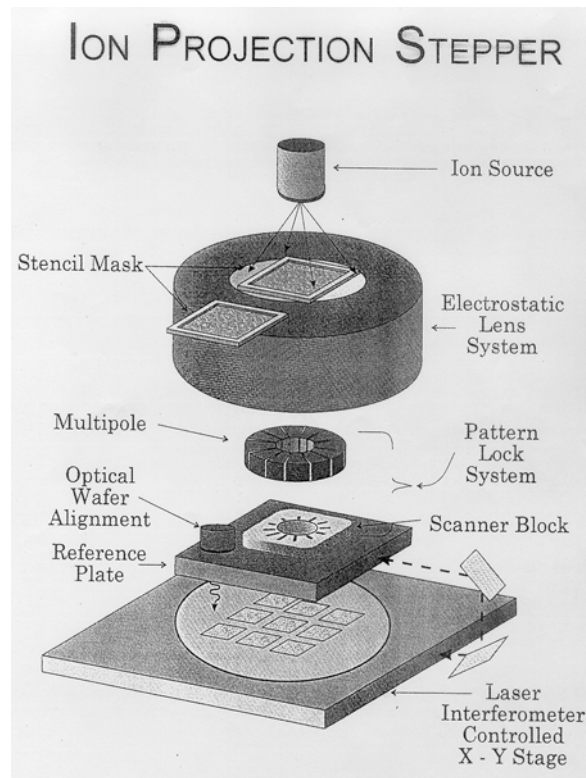
Fig. 3.3: Schematic representation of an IPL system [189]

All ion projection implantations were executed at the Fraunhofer Institute for Silicon Technology (ISiT) in Itzehoe, Germany by Dr. Brünger on an IMS, Vienna, Austria, prototype. Both IMS and ISiT have large experience building and optimizing IPL systems based on open stencil masks. This particular prototype system is equipped with a multicusp plasma ion source operating with a low energy spread, and a pattern lock system to guarantee precision in the 5 nm range for subsequent ion beam exposures. The stencil mask is produced by e-beam lithography and exhibits features as small as 200 nm [190]. The pattern from the mask is further reduced by ion optics by a factor of 3 - 8 times to finally produce features in the sub 100 nm range.

3.3 Electrochemistry

3.3.1 Electrolytes

Different electrolytes were used during this work. None of the electrolytes was deairated. To deposit Cu, the following electrolytes were used:

- $0.01\,M\ CuSO_4 + 0.05\,M\ H_2SO_4$ (electrolyte 1)
- $0.01\,M\ CuSO_4 + 0.05\,M\ H_2SO_4 + 100\,\mu M\ BTA$ (electrolyte 2)
- $0.05\,M\ CuSO_4 + 0.5\,M\ H_2SO_4 + 100\,\mu M\ BTA$ (used only in few experiments)

For Au deposition the electrolyte was $0.01\,M\ KAu(CN)_2 + 1\,M\ KCN$ (electrolyte 3). All solutions were prepared from analytical grade chemicals and deionised water.

Benzotriazole, BTA, was used in some experiments in order to determine if its beneficial influence on Cu deposition could be reproduced in our experiments. BTA is being used as a brightening additive in sulphuric acid based electrolytes for Cu deposition [191-193] as well as corrosion inhibitor [194-196]. It is thought that it adheres to active surface sites preferentially [192, 193], effectively decreasing both nucleation and growth during the deposition process. It has been shown that BTA forms an insulating layer on Cu surfaces [197-199]; this layer acts both as a corrosion inhibitor and as a brightener.

The recent change in device production from Al to Cu interconnects has renewed interest in BTA as a suppressor. Suppressors slow down deposition reactions by blocking active surface sites and by inhibition of charge transfers across the interface; they subsequently reduce the deposition rate at the entrance of a vias and trenches. These properties are required to promote super-filling of deep trenches where it is important that cavities are filled preferentially.

The addition of even small amounts of BTA should have a marked influence on deposition characteristics [192, 193]. Considerably smaller grains and a slower grain growth is to be expected. Furthermore, the grains should be of a more random orientation.

3.3.2 Macroscopic Electrochemical Measurements

To measure on a clearly defined, known surface area, a standard electrochemical cell was used for all macroscopic experiments: the sample is pressed against an o-ring by a Cu plate for electric contact (the Si samples had liquid InGa alloy smeared on their backside to assure ohmic contact). The cell is then filled with electrolyte and the reference electrode (equipped with a Haber-Luggin capillary to minimize ohmic drop) as well as a Pt-counter electrode are introduced from the top of the cell. A saturated calomel electrode (SCE) was used as standard and hence all potentials are with respect to the SCE (unless noted otherwise). The setup is shown in figure 3.4. In order to prevent any photoelectric effects, the sample was placed in a metallic blackbox which also acted as a Faraday's cage.
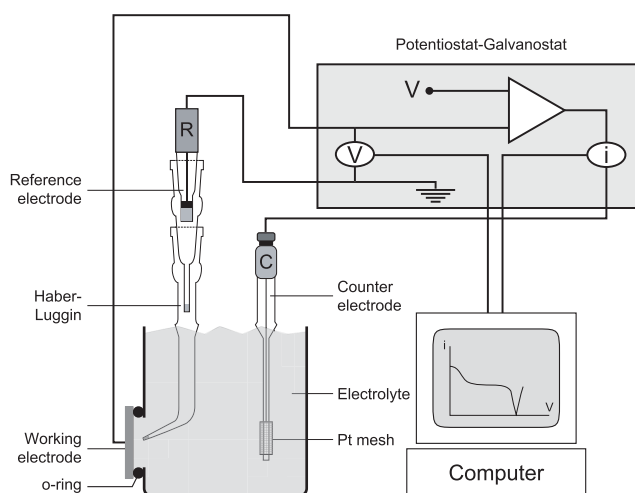
Fig. 3.4: Schematic view of the electrochemical setup

A Jaissle Potentiostat/Galvanostat 1002 T-NC was used together with a Burster Digistant 6706 voltage source and a Keithley 2000 Multimeter. The setup was piloted using custom-written software and run on a standard Dell PC equipped with a GPIB interface card.

3.3.3 Micro-electrochemical Experiments

Micro-electrochemical experiments were carried out on a setup shown schematically in figure 3.5 [200-202]. The electrochemical cell is similar to the one shown in figure 3.4 but shrunken to microscopic dimensions: the diameter of the investigated surface area can be varied from 2 µm to 1 mm by selecting appropriate glass capillaries. The glass capillary is filled with electrolyte and placed on the surface area of interest under an optical microscope. Measurements are performed only on the surface covered by the tip of the capillary it is therefore possible to investigate the electrochemical behaviour of small features such as grain boundaries, separate phases, intermetallic phases, or small defects (e.g. created by ion beam implantation) on Si surfaces.

Capillaries were prepared using a World Precision Instruments Pul-1 capillary puller and diameter was adapted by subsequent grinding using sandpaper. In order to prevent leakage of the electrolyte on the sample surface, a silicone rubber seal was applied at the capillary tip by repeated dipping in Dow Corning silicone 732. Capillaries in the 80 µm range (with a silicone seal of roughly 30 µm thickness) were used for all experiments.

Due to the small probe size, the measured currents are very small. By using specially shielded cables, custom made filters, and highly optimized components (Jaissle Potentiostat/Galvanostat IMP 83PC T-BC) currents down to 10 fA can be resolved. For precise control of the capillary positioning on the sample surface, the cell is mounted on an optical microscope and can be placed on the sample surface with an accuracy in the µm range.
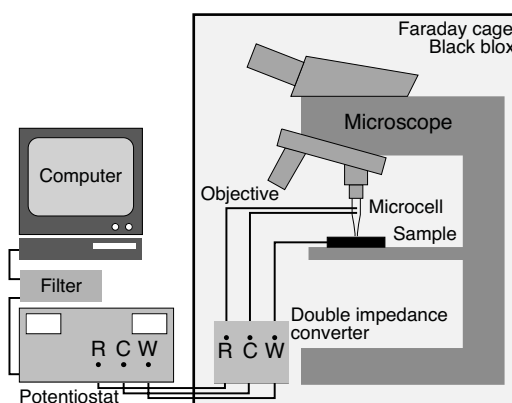
Fig. 3.5: Schematic view of the micro-electrochemical setup

A detailed view of the micro-cell is shown below in figure 3.6. Reference and counter electrode are connected to the capillary holder by an electrolyte bridge. The capillary holder also acts as an electrolyte reservoir; by applying a slight pressure at the reference electrode, electrolyte is forced out of the capillary to renew electrolyte between experiments without the need to disassemble the entire capillary holder.
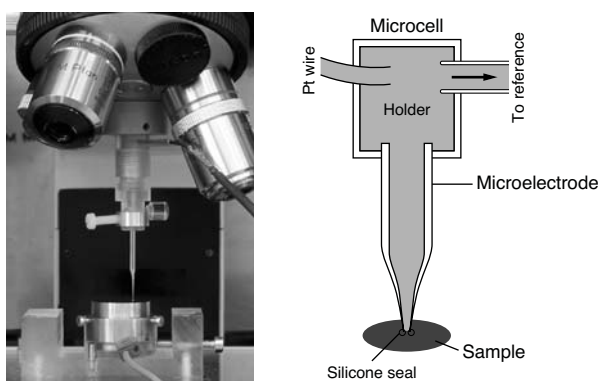
Fig. 3.6: Detail of the micro-cell in contact with the sample. Left: Photograph, right: schematic view.

3.4 Surface Characterization Techniques

In scanning electron microscopes (SEMs) an electron beam is focused into a fine probe and subsequently raster-scanned over a small rectangular area. As the beam interacts with the sample, it creates various signals (secondary electrons, internal currents, photon emission, etc.) all of which can be detected. These signals are highly localized to the area directly under the beam. By using these signals to modulate the brightness of a cathode ray tube, which is raster-scanned in synchrony with the electron beam, an image is formed on the screen. This image is highly magnified and usually looks like a traditional microscopic image but with a much greater depth of field. With ancillary detectors, the instrument is capable of elemental analysis. Pictures of implanted surfaces and deposits were taken using SEMs equipped with a field emission gun (CamScan CS 44 and Leo 1530) at an acceleration energy of 3 keV - 5 keV.

Atomic Force Microscopy (AFM) is employed when topological information of a sample surface is needed. In AFMs the sample surface is scanned with a sharp probe at a distance of less than a few nanometers, or in mechanical contact. For scanning either the tip moves against the fixed sample, or the sample moves against the fixed tip. In either case all movements are carried out by piezo-electric scanners. The probing interaction can be monitored with an appropriate detector. The detector signal is used for feedback control to adjust the tip-sample distance during the scanning process. Instrument operations are performed through a computer-controlled electronic unit, which allows to monitor the tip-sample approach, to record the strength of the probing interaction as a function of the tip position, to convert the collected information into an image on the screen, and to store the data. In this work a Topometrix TMX Explorer 2000 equipped with a 100 µm scanning unit was used. Images were treated using the Topometrix software and the free ImageSXM package (v1.69) on an Apple Macintosh. Only compensation filters were applied (x-y tilt correction, quadratic subtraction, 3-point compensation, as well as line-by-line compensations).

Raman spectroscopy is based on the Raman effect which may be described as the scattering of light from a gas, liquid or solid with a shift in wavelength from that of the usually monochromatic incident radiation. If the polarizability of a molecule changes as it rotates or vibrates, incident radiation of frequency ν should produce scattered radiation with an unchanged frequency, i.e. Rayleigh scattering. In addition, there should be Stokes and anti-Stokes lines of much lesser intensity and of frequencies $\nu +/- \nu_k$, respectively, where ν_k is a molecular frequency of rotation or vibration. The method is predominantly used for qualitative and quantitative analysis of covalently bonded molecules. Nevertheless, it can give information about the lattice structure of a crystal too. For our experiments, a Dilor XY800 system was used and a n excitation wavelength of 603nm was chosen. The spatial resolution of the system is <5µm.

Auger Electron Spectroscopy (AES) uses a focused electron beam to create secondary electrons near the surface of a solid sample. Some of these (the Auger electrons) have energies characteristic of the elements and, in many cases, of the chemical bonding of the atoms from which they are released. Because of their characteristic energies and the shallow depth from which they escape without energy loss, Auger electrons are able to characterize the ele-

mental composition and, at times, the chemistry of sample surfaces. When used in combination with ion sputtering to gradually remove the surface, Auger spectroscopy can characterize the sample in depth. The high spacial resolution of the electron beam and the process allows microanalysis of three-dimensional regions of solid samples. AES has high lateral resolution, relatively high sensitivity, standardless semi quantitative analysis, and may reveal chemical bonding information. In this work scanning Auger microscopy was used to investigate the metallic deposits on Si. A Physical Electronics PHI 670 system with a field emission gun was used for all experiments.

Chapter 4

RESULTS AND DISCUSSION

4.1 Preliminary Experiments

4.1.1 Current-Density/Voltage Curves on Intact and Scratched p-Si

In this section the investigation of the electrochemical behaviour of intact and scratched p-Si in various electrolytes will be presented; scratched samples are used as a model of damaged surfaces. The possibility of selective metal deposition on surface defects (i.e. scratches) will be considered. The goal is to limit the deposits to the scratched areas, either filling the scratches completely or at least by obtaining continuous lines. The optimization of the deposition process will focus on deposition potential and time; alternative electrolytes will also be considered. All experiments presented in this section were carried out using an O-ring electrochemical cell.

Figure 4.1 shows three typical current-density/voltage curves (CVCs) obtained on a scratched sample as well as on two different intact p-Si surfaces. Several remarks can be made with respect to these curves:

- The curves obtained under identical conditions on intact p-Si vary considerably: while one is almost identical to the one obtained on scratched p-Si, the other one shows currents roughly 50 times smaller. This indicates the likelihood of occurrence and the enormous impact of microscopic defects present at the wafer surface.
- A strong current increase occurs at roughly -400 mV; this current increase is due to the formation of Cu crystallites at the Si surface.

- At -500 mV the current decreases again. We assume that the crystal nucleation phase is finished at this point and growth is the predominant factor as nucleation leads to higher currents than diffusion limited growth.

- Optical examination of the samples shows that all of them exhibit Cu deposits; in the case of the scratched sample, the deposition process was initiated at the scratch and the deposit was massive. The intact sample with high current also shows massive deposits over the whole surface; a starting point can not be identified. The other intact sample shows light deposits without a clear starting point.

- While the behaviour of the scratched samples is reproducible, the intact samples vary widely in behaviour. The two samples presented here illustrate the two extremes: almost no deposition in one case and massive deposition in the other.
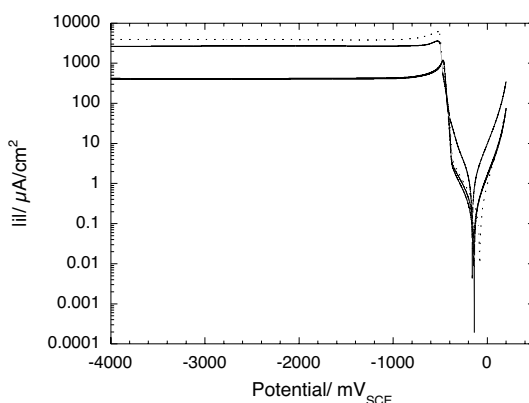
Fig. 4.1: Current-density/voltage curve of *p*-Si; the solid lines come from an intact surface, the broken line from a surface with a 1 mm long scratch. All curves obtained in 0.05 M H_2SO_4 + 0.01 M $CuSO_4$ (electrolyte 1), scanned at 15 mV/s.

It seems that defects on *p*-Si surfaces may be used to promote Cu deposition: on scratched surfaces Cu was always deposited starting at and around the defect site. On intact surfaces an incoherent behaviour was observed: while some surfaces showed a massive deposit, others show almost no deposits or an intermediate behaviour. We therefore assume that micro-

scopical defects introduced by surface contamination in a non-cleanroom environment, scratches due to inappropriate handling, and native defects may be sufficient to trigger Cu electrodeposition, especially at high voltages.

4.1.2 Potentiostatic Experiments on Scratched p-Si

The influence of electrolyte composition, deposition potential, and duration of the applied potential was investigated in a series of potentiostatic experiments; the figures in the following section are representative examples of the results obtained. Figure 4.2 shows SEM pictures of a series of experiments carried out on equivalent samples where the deposition potential was varied. While the deposition seems to be roughly selective to the scratched sites, the deposited structures are of poor quality: the crystallites are large and the scratch is not completely covered. An influence of the deposition potential can be seen: for low potentials (-500 mV) hardly any crystallites have developed while at -2500 mV large and better connected deposits prevail.
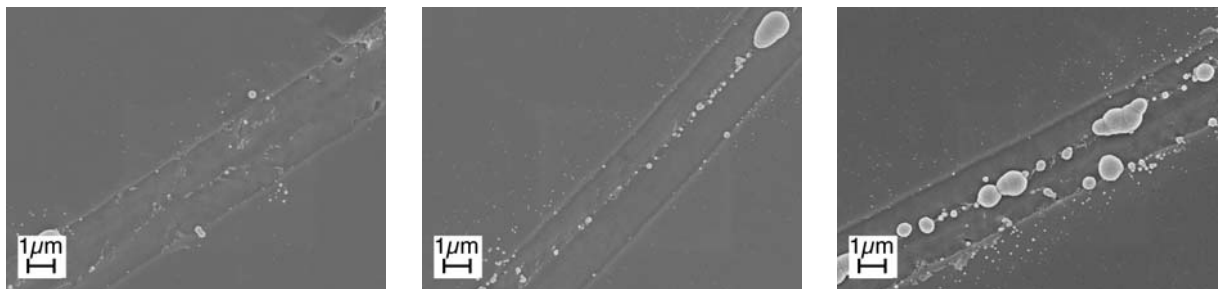
Fig. 4.2: SEM pictures of Cu deposits on scratched p-Si. All samples deposited from electrolyte 1 during 15 s at left: -500 mV, middle: -1500 mV, right: -2500 mV.

A next experiment tried to determine the influence of the deposition time. Increased deposition was expected for longer deposition times. Figure 4.3 shows that the influence of the deposition time is as expected: the longer the deposition time, the more the scratch is covered by Cu crystallites. However, selectivity to the scratch is still insufficient and the crystallites are too large.
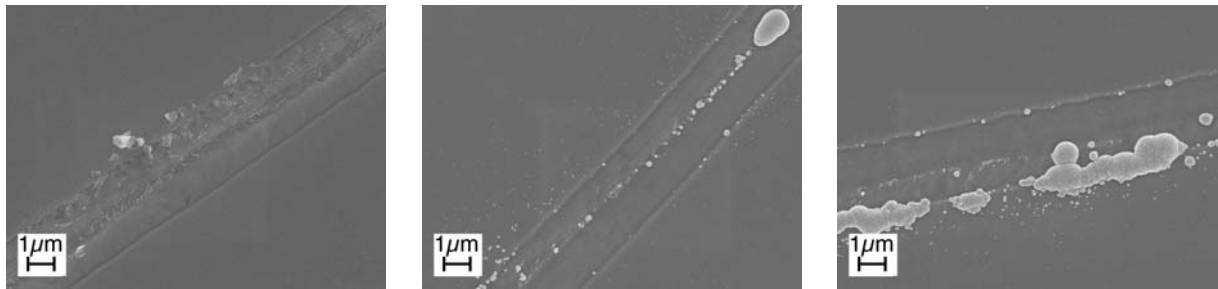
Fig. 4.3: SEM pictures of Cu deposits on scratched *p*-Si. All samples deposited from electrolyte 1 at -1500 mV during left: 2 s, middle: 15 s, right: 30 s.

Since the selectivity of the process, the spatial resolution, and the quality of the deposits left much to be desired, the possibility to improve these parameters by modifying the electrolyte was investigated. BTA –a 'classical' brightener– to was added to the Cu-based electrolyte and the results compared to a Au-based basic electrolyte.
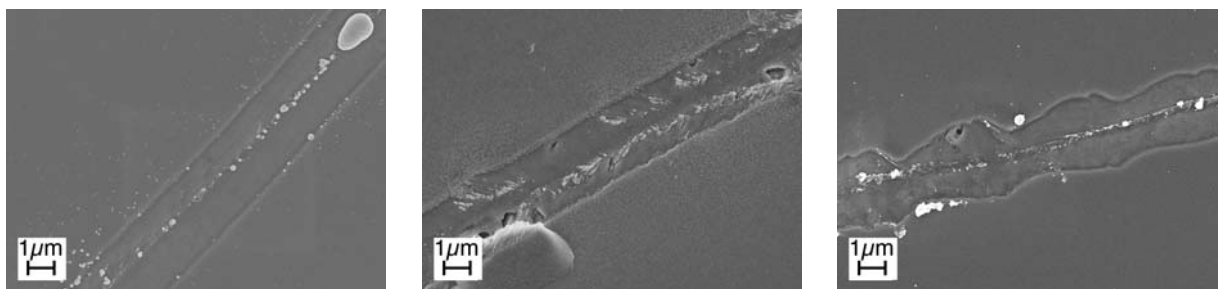
Fig. 4.4: Influence of electrolyte composition on deposit quality. All samples deposited for 15 s, left and middle sample at -1500 mV, right sample -2500 mV. Left: in electrolyte 1; middle: in 0.05 M H_2SO_4 + 0.01 M $CuSO_4$ + 100 µM BTA (electrolyte 2); right: in 0.01 M $KAu(CN)_2$ + 1 M KCN (electrolyte 3).

Figure 4.4 shows that while the addition of BTA leads to considerably smaller deposited crystallites, selectivity does not seem to have improved. For the Au-based electrolyte the situation is slightly better: deposits are smaller and only seem to have grown in or close by the scratch. However, in both cases coverage is still far from complete.

In conclusion it can be said, that selective electrodeposition of metals on scratched p-Si is only partially possible: while the deposition process seems to start in or close to the scratch, indicating that surface defects play a role in the electrochemical reactivity, selectivity is not satisfactory and coverage of the scratch is not sufficient. Santinacci *et al.* have reported similar results [55]. In the next section, surface defects were created in a more controlled manner using ion beam implantation.

4.2 Ion Beam Implantation

Experiments were performed with the goal of assessing and characterizing the damage created by both broadband ion implantation (BII) and FIB and to compare the two processes. For FIB implants it was also important to determine the resolution of the tool as well as the reproducibility of the process.

  p-Si samples were implanted with varying doses of Ga^+ and Au^{2+} ions[12] at 30 keV (BII) and 29.6 keV[13] (FIB). The samples were analyzed using optical microscopy, SEM, AFM, and Raman spectroscopy. The results obtained were compared with results obtained from samples implanted using the BII and with simulations performed using the SRIM software package [171].

  If the implantation current as well as the ionic species are known, it is possible to calculate the density of implanted ions per cm^2, D:

$$D = \frac{I \cdot t \cdot L}{n \cdot e \cdot A} \tag{4.1}$$

where I is the source-current, t the exposure time, L the number of scanning-loops, n the number of elementary charges per ion, e one elementary charge, and A the size of the implanted area; it is assumed that the focus size is much smaller than the implanted area and that, therefore, border effects can be neglected.

---

12. Au^{2+} ions were selected over Au^+ ions due to their higher yield. The Au-Er-Si ion source used allows to choose among a multitude of ionic species; however, their yield is often rather limited [203].
13. The Raith-Orsay Physics FIB used does not allow to freely choose the acceleration energy of the implanted ions. Available energies are 29.6 keV, 22.75 keV, 14.75 keV, and 8 keV.

For simple line scans the situation is slightly different, as the implanted area A is not known before the experiment but is given by the resolution of the FIB, w_B. While all other parameters can be measured with good precision, w_B can be measured with an accuracy of ~20% only [179], leading to an error of some 40% for the current density. Also, as figure 4.5 shows, the intensity distribution over the beam diameter is rather complicated. To simplify calculations, a Gaussian distribution is assumed and the beam width is approximated as the Gaussian's full width at half maximum.

During the experiments the beam-width was estimated using the so-called edge-method where the beam is moved over a solid edge on the substrate [179]. The beam width can then be estimated with satisfactory accuracy from the secondary electron image.
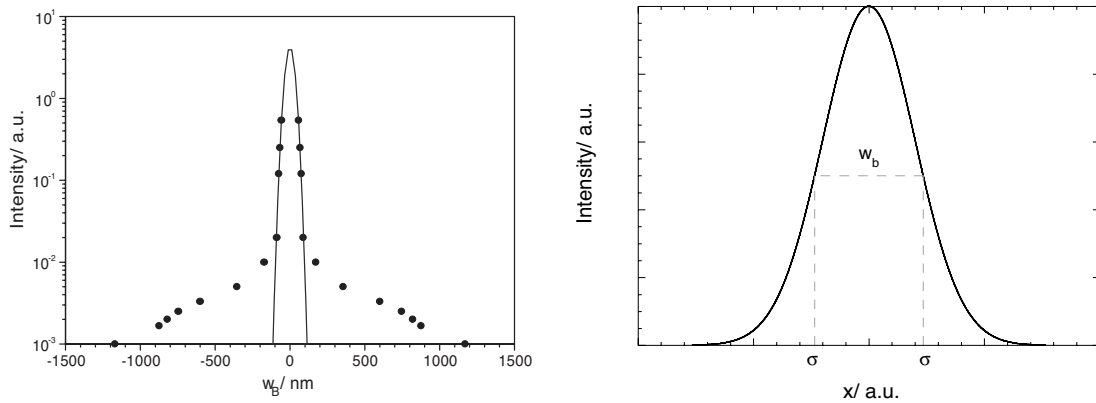
Fig. 4.5: Intensity distribution in a focused ion beam. Left: measured intensity distribution for a Co^+-ion beam at 35 keV [179]. Right: schematic representation of the Gaussian intensity distribution (σ denotes the full width at half maximum and w_b the approximated beam width).

Assessing damage due to ion implantation is rather difficult: while AFM offers a resolution in the nm-range, it is only capable of detecting surface damage, i.e. sputtering which occurs at high implant doses only. For low doses implantation is the prevailing mechanism. Optical techniques on the other hand, such as optical microscopy or Raman which may be more sensitive as they are able to detect changes in the refractive index in the implanted material,

are limited to a resolution of roughly 700 nm. As the only technique that's easily accessible to us is AFM, we will be using sputtering profiles as a benchmark of the implantation process, assuming that the trends observed for sputtering will be the same for implantation processes.

Sputtering profiles were measured by AFM for samples implanted by FIB with Au^{2+} ions at doses ranging from 10^{12} to 10^{15} ions/cm^2 and Ga^+ with concentration between $5 \cdot 10^{15}$ and $5 \cdot 10^{17}$ ions/cm^2 (all at 29.6 keV). Figure 4.6 shows the AFM profiles of FIB lines obtained at different doses and compares them to simulated implant profiles (figure 4.7). All FIB-lines were obtained with a nominal beam-width of roughly 200 nm by repeated scanning. The v, u, and w-shaped profiles have been described by other groups [204] and may be due to different factors:

- Re-deposition of sputtered ions occurs at the border of the sputtered trace. Depending on the implantation dose if two sputtered traces are parallel and close to one another, redeposition to form a W-shaped groove may occur.

- Stability problems in the FIB: For high doses, exposure times of several minutes have to be used even for narrow lines. Since the FIB is not equipped with a 'single line mode', the desired dose is obtained by scanning repeatedly over the same surface[14]. Furthermore, the ion source used as well as the extraction voltage rarely remained stable enough for sub-500 nm operation taking more than a few minutes.

---

14. Theoretically, longer pixel dwell times, t_d, might prevent this. However, experiments have shown that a longer t_d actually leads to a loss in resolution (especially at low implant doses where the best resolution was obtained). We assume that this is due to increased straggling and channeling.
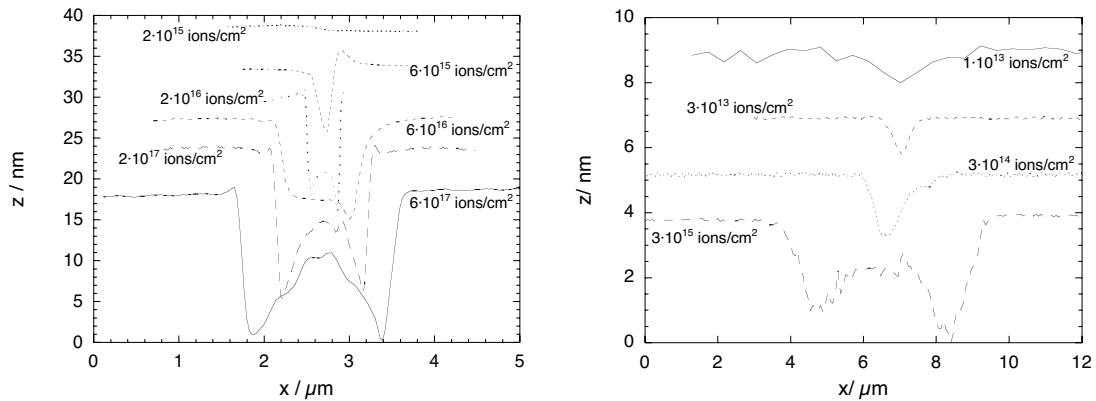
Fig. 4.6: AFM-profiles of FIB sputtered p-Si surfaces. Left: Ga$^+$ with FIB; right: Au^{2+} with FIB (both samples implanted at ~30 keV).

Figure 4.7 shows calculations for the depth distribution of various ions at different energies in p-Si. The effect of the ion mass both on the sputter profiles (and therefore the surface damage) as well as on the depth distribution of the defects can be seen very clearly:

- Higher ion doses lead to more sputtering (figure 4.6, left) while vacancy distribution remains virtually unaltered (not shown) for different implant doses (their total number does increase however).

- Heavier ions lead to more efficient sputtering (figure 4.6). Also, they create defects closer to the surface because nuclear stopping is prevalent (figure 4.7, right).

- Higher implant energies lead to a broader and deeper vacancy distribution (figure 4.7, left).
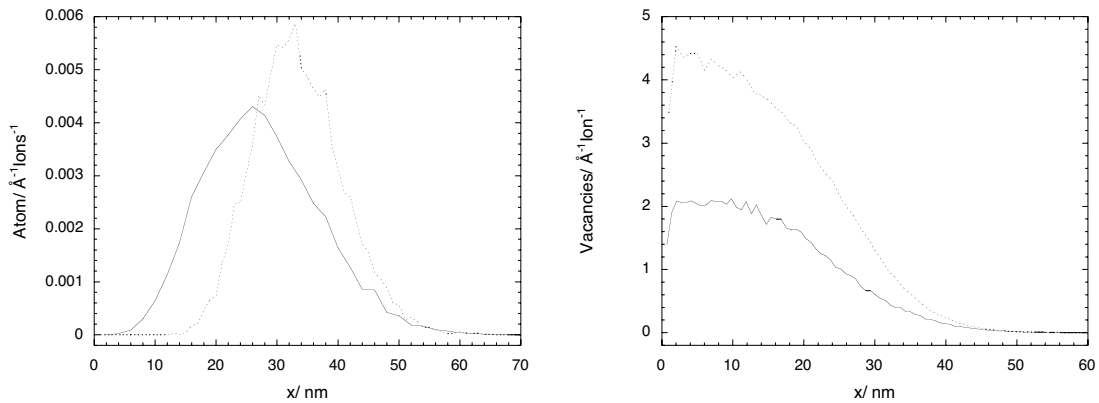
Fig. 4.7: Calculated depth distribution of implanted species and vacancies for Ga^+ (——) and Au^{2+} ($\cdots$) ions implanted in Si at 29.6 kV (i.e. 29.6 keV for Ga^+ and 59.2 keV for $Au2^+$; all calculations performed using SRIM-2000 code and 10'000 impinging ions).

While the SRIM-2000 code used to calculate the implantation profiles in figure 4.7 is well established and reliable, it is less reliable for predicting sputtering profiles as it does not consider the changes in the substrate induced by the impinging ions. While straggling can be simulated (figure 2.13), all ions are considered to lie at the sample surface as the code 'resets' the substrate conditions after every impinging ion. Making some basic assumptions (based on the FIB's pixel write size of 100 nm, an atom's size, the ions needed to actually sputter an atom, the number of vacancies created etc.) it is still possible to use these values for estimating a sputter profile (figure 4.8)[15]. While the width is predicted rather accurately, the depth is off by a factor of >2; we assume this is due to redeposition and high current density in the beam, both of which are not taken into account.

15. SRIM-2000 code allows to calculate the distribution of sputtered atoms for an incident ion beam. By attributing a volume to each of the sputtered atoms and by simply adding these volumes together, an estimate of the sputter profile can be obtained. However, as SRIM-2000 code is not a dynamic model, the estimates will not be precise; changes in the substrate such as strain-induced hardening, amorphization, the creation of interstitials and vacancies, as well as changes in the surface geometry due to sputtering and redeposition are not taken into account.
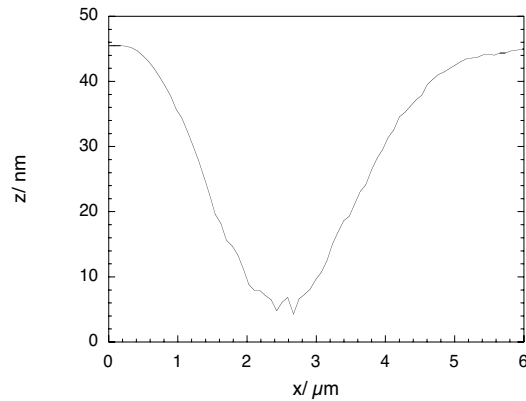
Fig. 4.8: Approximated simulated sputter profile (10^{15} Ga$^+$/cm^2 at 30 keV).

The question arises whether the electrochemical sensitivity depends on the ion species, their concentration, the sputter profile, or the implanted defects and their distribution. This point will be approached in experiments performed later on.

All AFM measurements were obtained from samples with rather high implantation doses. Due to the very shallow sputtering profiles for concentrations lower than 10^{13} Au^{2+}/cm^2 and 10^{15} Ga$^+$/cm^2 respectively, we were unable to detect any surface damage at all[16]. Also, SEM turned out to be a rather unsuited technique to observe ion-induced damage in p-Si; for high implantation doses SEM pictures can be obtained, but for doses below 10^{14} Ga$^+$/cm^2, the damage created was virtually indetectable by SEM analysis.

---

16. Other groups have reported a slight surface bulging due to ion implantation for low implantation doses of Si^{2+} ions in GaAs at 100 keV [205].
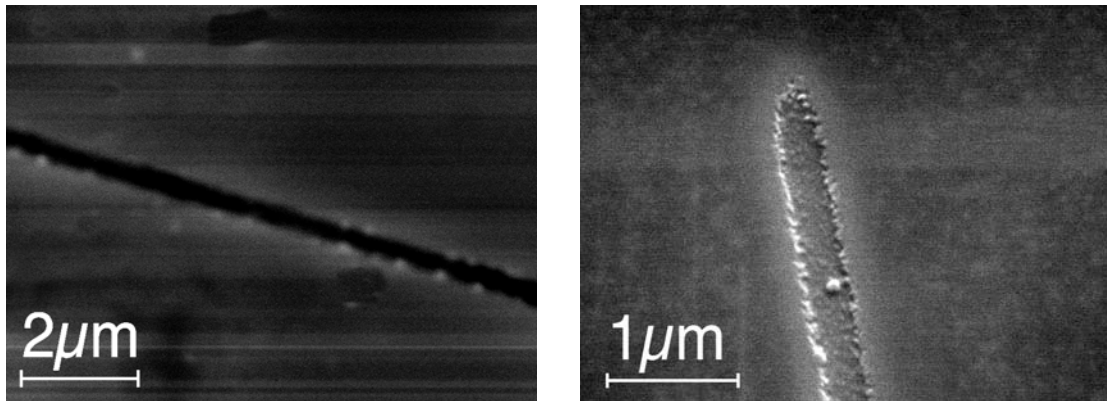
Fig. 4.9: SEM pictures of p-Si samples implanted with left: $9{\cdot}10^{14}\,\mathrm{Ga^+/cm^2}$, right: $10^{16}\,\mathrm{Ga^+/cm^2}$; both at $29.6\,\mathrm{keV}$ (pictures were taken on different SEMs).

As we have indicated before, optical microscopy is in fact well suited for the observation of ion-induced damage. Figure 4.10 shows that doses as low as $10^{13}\,\mathrm{Ga^+/cm^2}$ are still visible with an optical microscope. Due to the fact that ion implanted Si drastically changes its reflection index, it becomes possible to use optical techniques to asses the damage produced in a SC [206]. The drawback of this technique is its limited resolution.
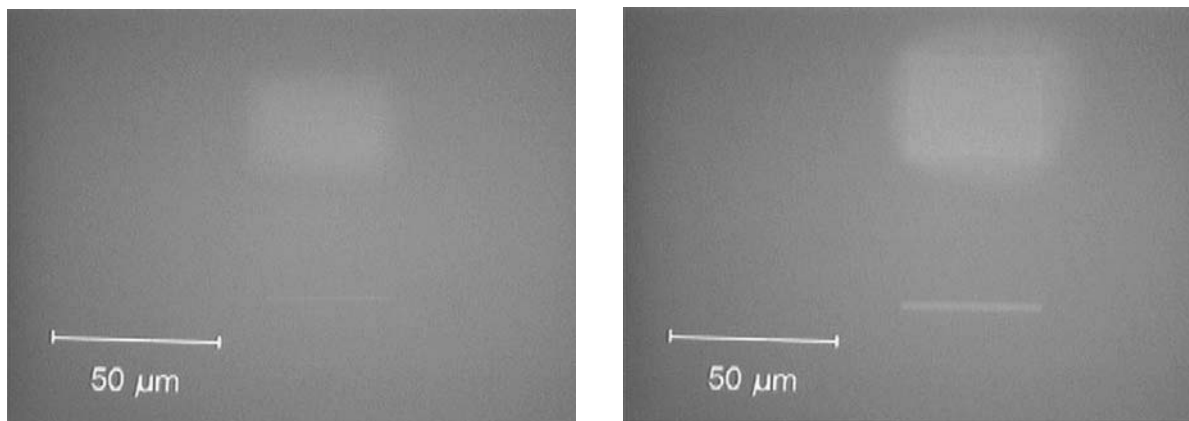
Fig. 4.10: Optical microscopy images of p-Si implanted with a) $9{\cdot}10^{13}\,\mathrm{Ga^+/cm^2}$ and b) $9{\cdot}10^{16}\,\mathrm{Ga^+/cm^2}$ (the implanted pattern is a square $40\mathrm{x}40\,\mathrm{\mu m^2}$ and –separated by $40\,\mathrm{\mu m}$– a line scan of $40\,\mathrm{\mu m}$).

One of the goals of these preliminary FIB-implantation experiments was also to determine the maximum resolution of the FIB tool used. Based on the pictures and figures shown above (Figures 4.6 to 4.10), the resolution seems to lie around 500 nm. However, on-screen resolution in scanning ion beam microscope mode showed a minimum beam width (with a Ga-ion source) of roughly 150 nm - 200 nm. When implanting with low doses, this resolution can be obtained, but not enough damage is created to be detectable by SEM and AFM. Optical techniques on the other hand are limited to a minimum size range of roughly 500 nm - 700 nm. The Ga-ion source proved to be the most stable one, it needed only little heating (reducing thermal scattering of the ions), and did not need a second mass-separating aperture (a second crossover that would introduce even more scattering is prevented) which allowed to work in parallel mode (see chapter 3.2.1).

To characterize the damage in the substrate's crystalline structure, Raman spectra were taken of samples implanted at different doses and with different implanters (figures 4.11 and 4.12). The results are quite surprising in that the dose needed for substrate amorphization is roughly 50 times higher for FIB implanted samples: Raman spectra show the characteristic humps for amorphous silicon at 480 cm^{-1} and at 140 cm^{-1} (barely shown at the left border of the spectra) [207] only at doses of 10^{16} Ga$^+$/cm^2 and above, while BII implanted Si becomes amorphous at doses as low as $5 \cdot 10^{14}$ Ga$^+$/cm^2, which is in agreement with earlier studies [208]. We assume that the increased noise in the data is due to surface roughening caused by the ion implantation.
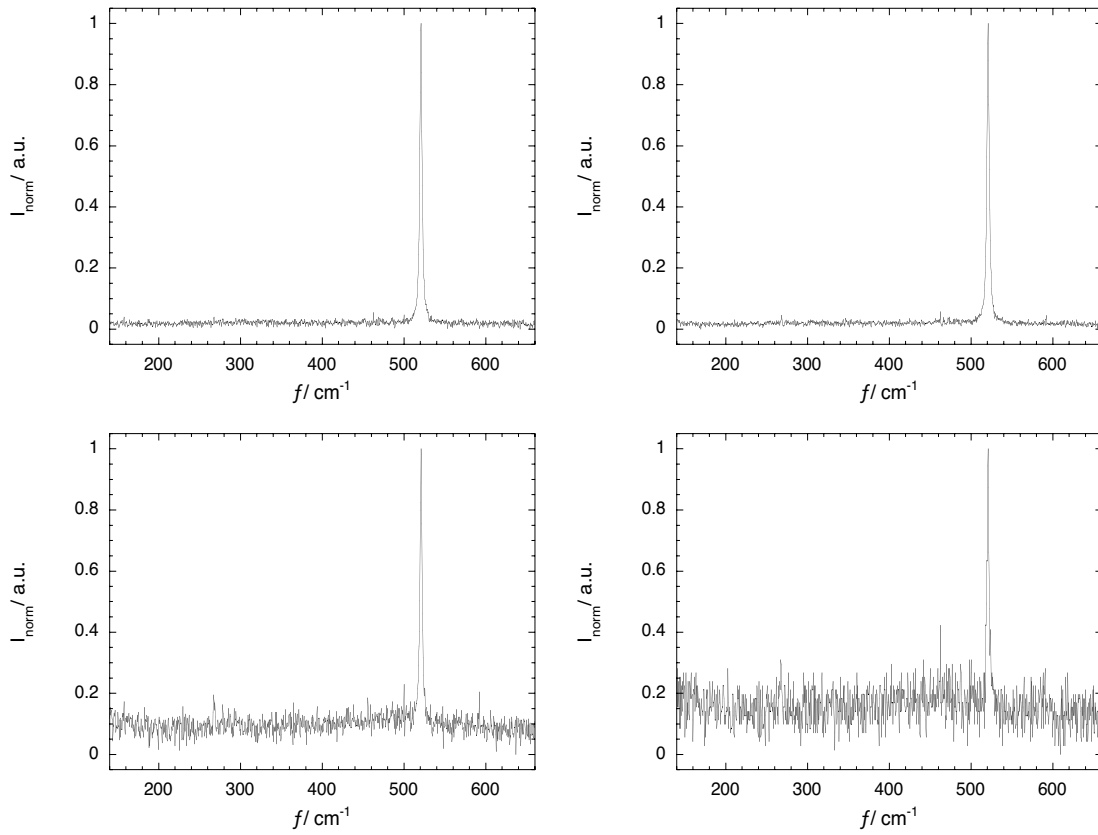
Fig. 4.11: Raman spectra of FIB implanted *p*-Si. From top left to bottom right the doses are as follows: reference sample (no implantation), 10^{15} Ga/cm^2, 10^{16} Ga/cm^2, 10^{17} Ga/cm^2.

To explain the difference in amorphization behaviour, one must keep in mind the different conditions under which these two samples were implanted. While one sample was exposed to a very high ionic current for a short time, the other one was exposed to a low ionic current for a long time.
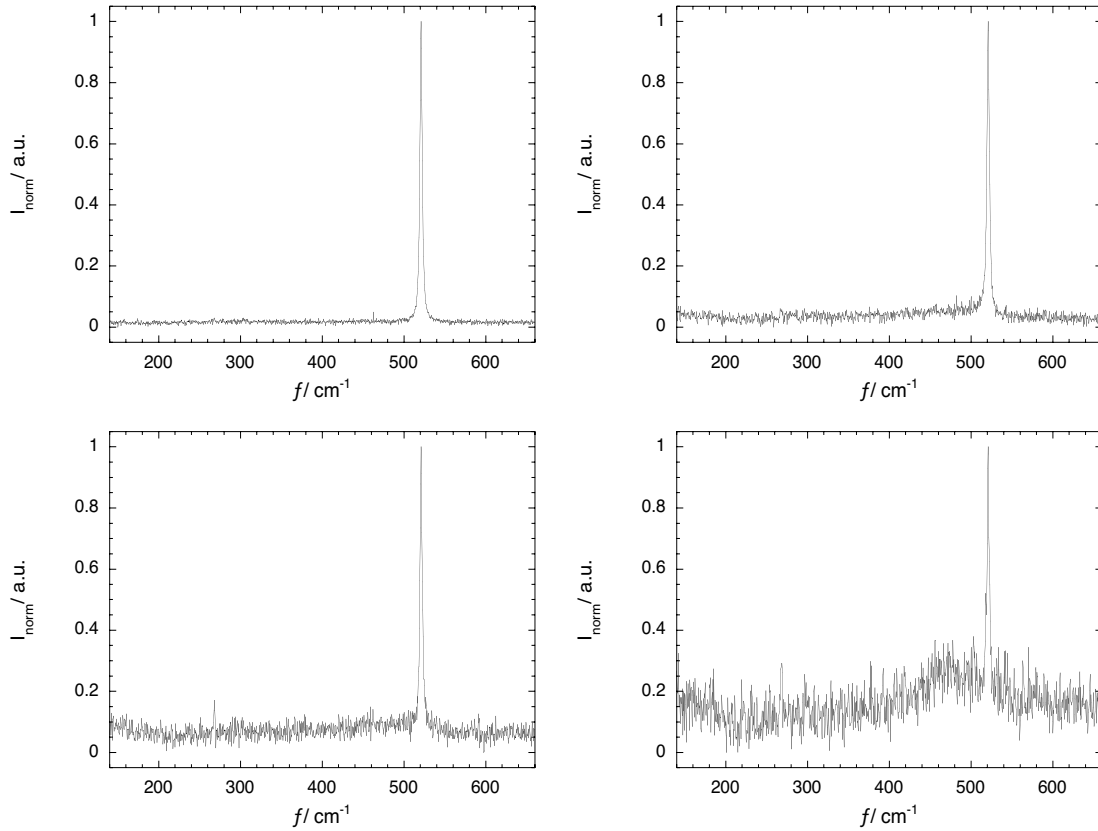
Fig. 4.12: Raman spectra of BII implanted p-Si. From top left to bottom right the doses are as follows: reference sample (no implantation), $10^{14}\,Ga/cm^2$, $5{\cdot}10^{14}\,Ga/cm^2$, $10^{15}\,Ga/cm^2$.

Hausmann *et al.* [179, 209-211] have shown the importance of both dwell time and current density of the ions delivered on the defect accumulation mechanism. According to their studies short dwell time ($< 1\,\mu s$) and high current density ($> 1\,A/cm^2$) both lead to increased 'tolerance' of the substrate for ion damage, meaning that a higher dose is needed until the substrate becomes amorphous. They explain this behaviour with the short healing time for ion-induced defects on one side (a short dwell time may leave enough time for the substrate to anneal the defects spontaneously) and the increased probability for 'annihilation' of impacts –i.e. the case where two ions hit the exact same atom on the substrate– at high cur-

rent densities. As the FIB samples were implanted using a short pixel dwell time of 50 µs (for better resolution) and at very high current densities of up to $> 10\,A/cm^2$ (compared to some $µA/cm^2$ usual for BIIs) significantly different amorphization doses are to be expected for FIB and BII implanted samples.

4.3 Electrochemical Deposition of Copper Structures on Ion Implanted *p*-Si

This section will be devoted to a detailed study of the electrochemical behaviour of Cu containing electrolytes on ion implanted *p*-Si. The influence of implantation parameters and electrochemical parameters will be looked at.

4.3.1 Implantation Dose

Based on the above Raman spectra, which indicated important differences between samples implanted with different ion doses we decided to first investigate the influence of the ion implant dose on the deposition process. Only BII implanted samples were used for this experiment due to their superior homogeneity and reproducibility compared to FIB implanted samples. A deposition potential of -1500 mV, applied for 15 s[17], was selected as this should assure massive deposition but no significant H_2 evolution (see figure 4.1).

---

17. To keep the text more readable, only a selection of the results is shown here. The appendix section (page 117) gives a complete overview over all the results obtained in this and the following series of experiments.
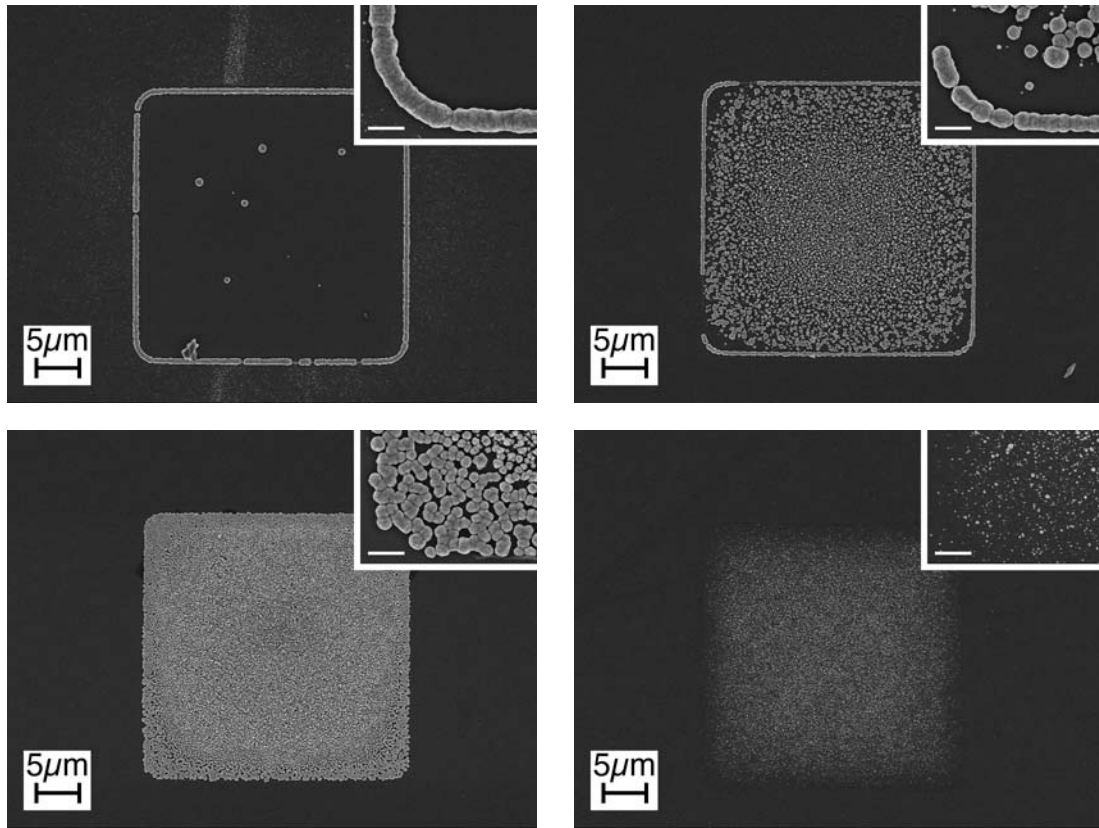
Fig. 4.13: SEM pictures of ion implanted p-Si. Samples implanted at 30 keV with varying doses of Ga$^+$ by BII. Electrochemical conditions: 15 s in electrolyte 1 at -1500 mV. Ion dose (from top left to bottom right): 10^{15} Ga$^+$/cm^2, $5 \cdot 10^{14}$ Ga$^+$/cm^2, $5 \cdot 10^{13}$ Ga$^+$/cm^2, 10^{12} Ga$^+$/cm^2. The insert shows a magnification of the bottom left corner, the marker is 1 μm.

Figure 4.13 shows the important influence of the implant dose. At the highest dose, the implant is almost completely deposit free, and only on the border a broad line of Cu has formed. The Raman spectra taken previously showed that, at this dose, the substrate becomes amorphous; it therefore seems that amorphous silicon (a-Si) acts almost like a mask. The large deposit at the implant border may be due to geometric effects influencing the current distribution as well as to a dose gradient. The sample implanted at $5 \cdot 10^{14}$ Ga$^+$/cm^2 shows an intermediate behaviour: a very strong deposit at the implant border and coarse-grained, widely spaced crystallites on the implant. At an intermediate dose of

$5 \cdot 10^{13}\,Ga^+/cm^2$ the deposit quality looks relatively best, although not good enough for sub 500 nm resolution. Also, the crystallites are still rather loosely arranged. For low implant doses $\leq 10^{12}\,Ga^+/cm^2$ only few and small crystallites develop. Clearly, not enough defect sites are available for successful deposit formation.

4.3.2 Deposition Potential

Based on the previous results samples implanted with a dose of $5 \cdot 10^{13}\,Ga^+/cm^2$ were exposed for 15 s to electrolyte 1. The following potentials were chosen (see figure 4.1):

- -500 mV; apparently the Cu-deposition onset potential.
- -1500 mV; massive Cu deposition seems to take place.
- -2500 mV; a potential low enough for H_2-evolution to occur.

Figure 4.14 shows the influence of different deposition potentials: at -500 mV crystallites are small, their density is low and they do not cover the implant completely. At -1500 mV the implant is well covered, the edges are well defined and no outgrowth occurs. At -2500 mV the structure is still well defined, however the border shows a rampart-like inhomogenous structure. The inserts further show that all the deposits are inhomogenous, rough, formed of large crystallites (several 100 nm) and that they do not fully cover the substrate.
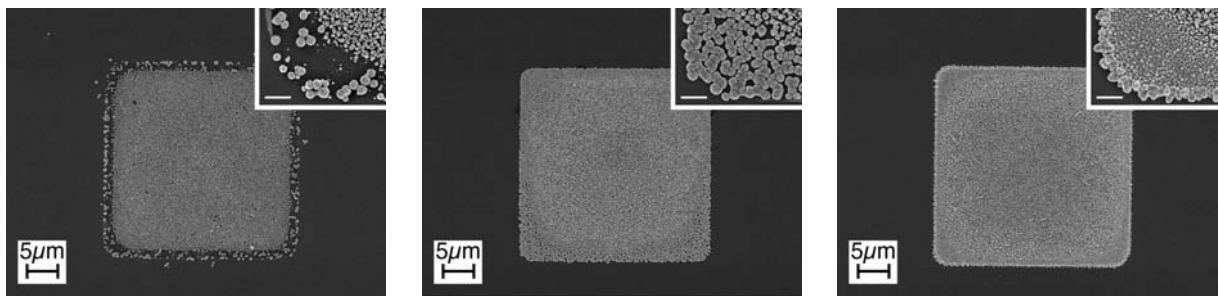
Fig. 4.14: SEM pictures of ion implanted *p*-Si. Samples implanted at 30 keV with $5 \cdot 10^{13}\,Ga^+/cm^2$ by BII. Electrochemical conditions: 15 s in electrolyte 1 at left: -500 mV, middle: -1500 mV, right: -2500 mV. The insert shows a magnification of the bottom left corner, the marker is 1 μm.

4.3.3 Deposition Time

In this section, we investigate the influence of the deposition time. All conditions are identical to before, the deposition potential is fixed at -1500 mV and the deposition time is varied from 2 s to 15 s to 30 s.
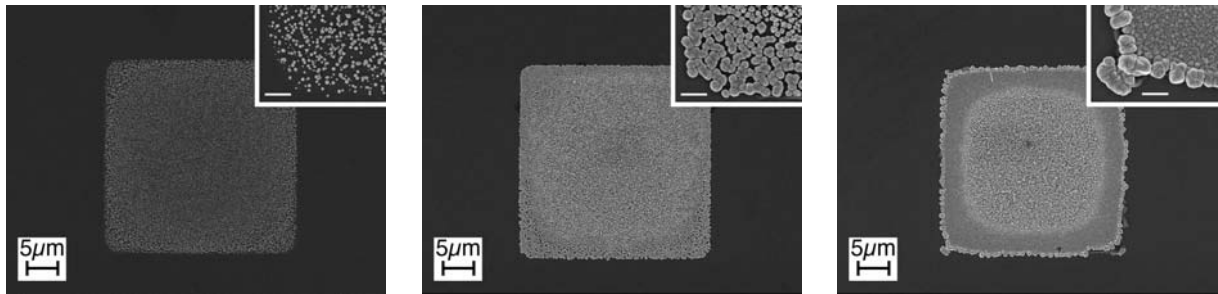
Fig. 4.15: SEM pictures of ion implanted *p*-Si. Samples implanted at 30 keV with $5 \cdot 10^{13}$ Ga$^+$/cm^2 by BII. Electrochemical conditions: At -1500 mV in electrolyte 1 for left: 2 s, middle: 15 s, right: 30 s. The insert shows a magnification of the bottom left corner, the marker is 1 µm.

Figure 4.15 shows that choosing the right deposition time is crucial for obtaining usable metal structures: With a deposition time of 2 s the implant is not completely covered with crystallites; while their size is small (≤ 100 nm), they are not fully interconnected and do not form a coherent deposit. At 15 s they still do not fully interconnect, while their size is already well beyond 200 nm. At 30 s –although interconnecting nicely– they are already too big for sub 500 nm resolution. Furthermore, they show dendritic growth in the centre of the implant.

The previous examples (figures 4.13 - 4.15) as well as the experiments in the appendix section (page 117) illustrate that deposits of high resolution, with sharp edges, complete coverage of the implants, and finely grained crystallites are difficult to obtain with the electrolyte chosen. Implant doses around $5 \cdot 10^{13}$ Ga$^+$/cm^2 seem to yield the best results. However, even then the results are not satisfactory: for short deposition times coverage is not complete, while long deposition times lead to dendritic growth. Similar effects are observable for the applied potential: at low potentials not enough crystallites form, while high potentials promote outgrowth and dendrites. Combinations of short deposition times at high potentials or

long deposition times at low potentials do not yield better results as, can be seen in the appendix section (page 117): short times (even at high potentials) do not lead to complete coverage; this is also the case for long times at low potentials (where the results were slightly better but still not satisfying).

4.3.4 Addition of BTA

The previous chapters show that selective electrodeposition of Cu structures is possible on ion implanted p-Si. However, in principle the deposits obtained are unusable for practical applications: the crystallites are too large (often due to dendritic growth), coarsely grained, and not well interconnected. It has been suggested (e.g. [191-193, 212, 213]) that the addition of brighteners such as BTA may improve the quality of the deposits. Experiments identical to the ones performed before were therefore carried out in a BTA containing electrolyte. Figure 4.16 shows the influence of the ion dose in the case of a BTA containing electrolyte.
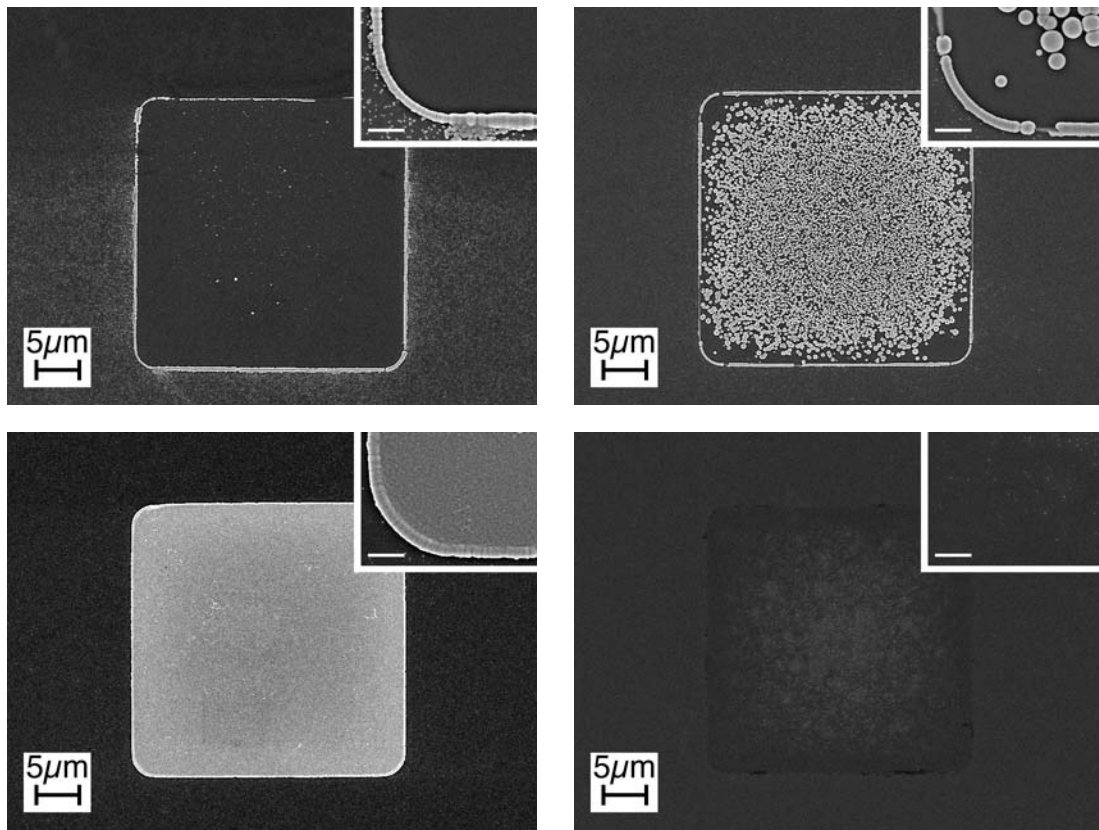
Fig. 4.16: SEM pictures of ion implanted *p*-Si. Samples implanted at 30 keV with varying doses of Ga$^+$ by BII. Electrochemical conditions: 15 s in electrolyte 2 at -1500 mV. Ion dose (from top left to bottom right): 10^{15} Ga$^+$/cm^2, $5 \cdot 10^{14}$ Ga$^+$/cm^2, $5 \cdot 10^{13}$ Ga$^+$/cm^2, 10^{12} Ga$^+$/cm^2. The insert shows a magnification of the bottom left corner, the marker is 1 μm.

Apparently, a-Si effectively acts as a mask and deposition only takes place at the border of the sample implanted with 10^{15} Ga$^+$/cm^2. Also, incomplete coverage is still observed for a dose of $5 \cdot 10^{14}$ Ga$^+$/cm^2, indicating that the implantation leads to a partial amorphization of the substrate. For doses of $\leq 10^{12}$ Ga$^+$/cm^2 almost no deposit can be observed; the crystallites are well below 50 nm and very scarce. The most interesting case occurs at an intermediate implant dose of $5 \cdot 10^{13}$ Ga$^+$/cm^2: the implant is completely covered by Cu crystallites, no outgrowth can be seen, and the crystallites are well below 100 nm.

The influence of the deposition potential is shown below in figure 4.17 and is more marked than for the BTA-less electrolyte: almost no deposit can bee seen at the highest deposition potential. At -2500 mV a rampart-like structure is formed at the border and some outgrowth occurs.
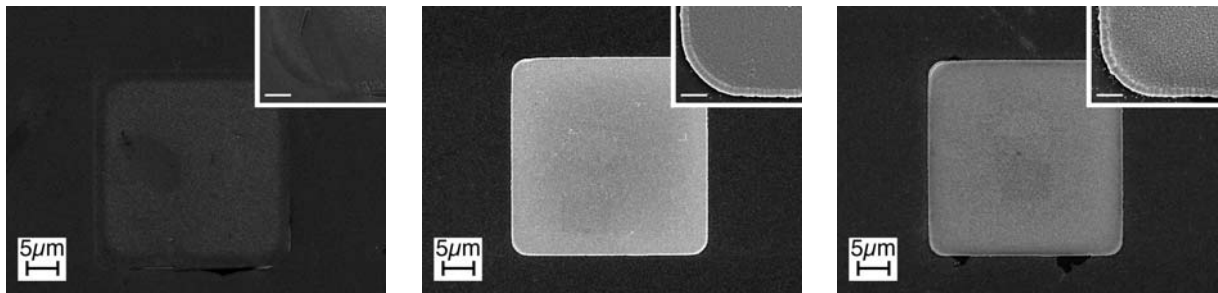

Fig. 4.17: SEM pictures of ion implanted *p*-Si. Samples implanted at 30 keV with $5 \cdot 10^{13}$ Ga$^+$/cm^2 by BII. Electrochemical conditions: 15 s in electrolyte 2 at left: -500 mV, middle: -1500 mV, right: -2500 mV. The insert shows a magnification of the bottom left corner, the marker is 1 µm.

The time dependence of the deposits is also straightforward (figure 4.18): for low deposition times the implant is not entirely covered and the edge is not very well defined. For long deposition times, a bulging occurs at the border caused by preferential deposition and crystallites begin to form even at distances several µm away from the principal structure.
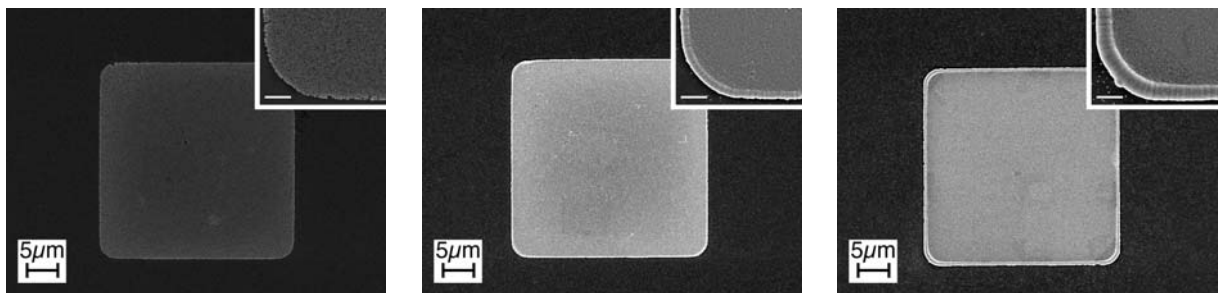
Fig. 4.18: SEM pictures of ion implanted *p*-Si. Samples implanted at 30 keV with $5 \cdot 10^{13}$ Ga$^+$/cm^2 by BII. Electrochemical conditions: At -1500 mV in electrolyte 2 during left: 2 s, middle: 15 s, right: 30 s. The insert shows a magnification of the bottom left corner, the marker is 1 µm.

The above examples as well as figure 4.19 (a 'worst-case', with deposition performed during 30s at -2500 mV) show the beneficial influence of the BTA-addition: the deposits are finely grained and do not show dendritic growth. Based on these results we are confident that a BTA containing electrolyte can be used to selectively deposit structures with a resolution well below 500 nm.
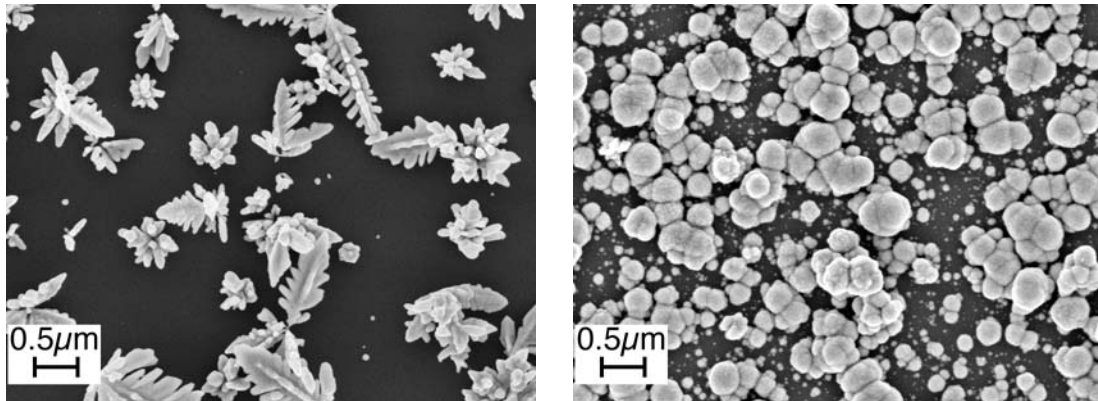

Fig. 4.19: High-resolution SEM pictures of ion implanted p-Si. Samples implanted at 30 keV with $10^{15}\,Ga^+/cm^2$ by BII. Electrochemical conditions: At -2500 mV during 30s; Left sample in electrolyte 1, right sample in electrolyte 2. Dendritic structures are clearly visible in the left sample and absent in the right one.

Traditionally, the smoothing action of BTA is explained by its capability to form stable complexes with Cu-ions present in the electrolyte, which then form a barrier layer at the electrode/electrolyte interface. This barrier layer inhibits 2D-diffusion of adsorbed species at the electrode surface, leading to decreased growth velocity of existing crystallites and smoother deposits. To verify if a similar mechanism exists in the case of Si substrates, impedance spectroscopy was used to determine the resistivity of the electrode/electrolyte interface.
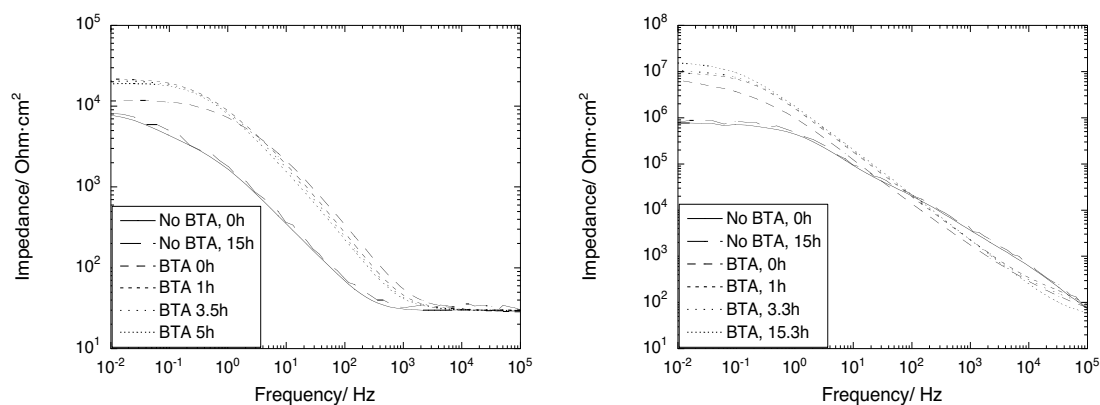
Fig. 4.20: Impedance spectra of left Cu 99.99 % and right *p*-Si in 0.05 M H_2SO_4 (taken at ocp –-77 mV on Cu, -259 mV on Si–, disturbance 10 mV). The left border of the spectra represent an approximation of the interface resistivity.

The impedance spectra of figure 4.20 show that BTA is indeed capable of forming a high resistivity barrier at the electrode surface. This effect is also observable on Si, which may explain why almost no Cu was deposited at -500 mV in the presence of BTA, since most of the surface defects would be 'blocked' by the barrier layer; we assume that this layer would only break down at more cathodic potentials. It is also worth noting that the addition of BTA produces an immediate effect, indicating that it forms indeed a barrier layer (and that the increased resistivity is probably not due to the formation of a surface oxide over time). The interface resistivity increases slightly over time, indicating that the barrier layer is not only quite stable in an acidic electrolyte but is even capable of growing. Experiments over long exposure times in BTA-free (see figure 4.20) as well as in deairated (see figure 4.21) electrolyte also seem to indicate that an oxide layer is not formed: no significant increase in resistivity is observed even after 15 h in a BTA-free electrolyte, while resistivity increased immediately even in a deairated electrolyte.
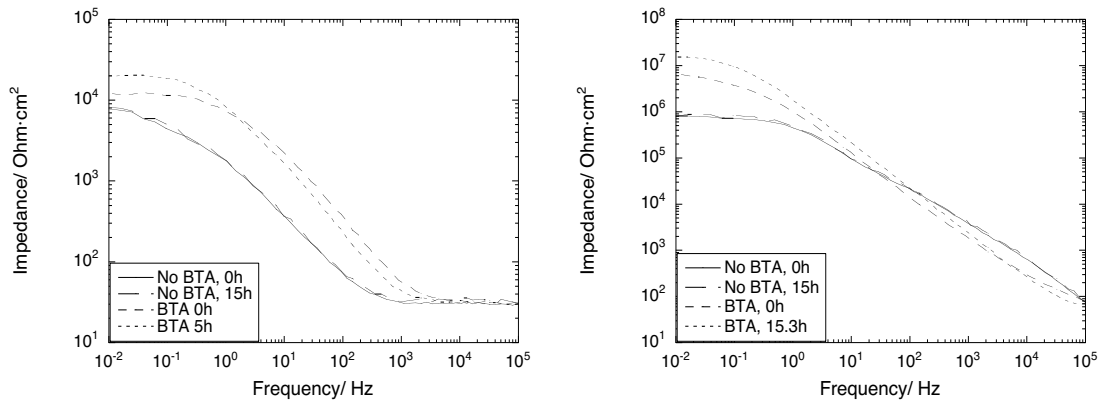
Fig. 4.21: Impedance spectra of left Cu 99.99 % and right *p*-Si in oxygen-free 0.05 M H_2SO_4 (taken at ocp −-75 mV on Cu, -260 mV on Si−, disturbance 10 mV). The left border of the spectra represent an approximation of the interface resistivity.

4.3.5 Microelectrochemical Investigation

The previous chapters have shown the great importance of the electrochemical conditions and the ion implant dose for the microstructure of the deposits. In this chapter deposition characteristics will be investigated using microelectrochemical techniques. A major problem when studying the electrochemical behaviour of ion implanted *p*-Si is the fact that the implanted surfaces are usually microscopic with respect to the sample surface. As we have seen previously (chapter 4.1.2), even the slightest scratch or even native defects may initiate the metal deposition process. Therefore, measurements obtained over a large surface area represent the average of all electrochemical events taking place on the whole surface whether intended or accidental. In order to obtain information on the electrochemical behaviour of the implanted surface only, microelectrochemical experiments are perfectly suited as they allow to measure on implanted sites specifically, excluding any undesired interference.
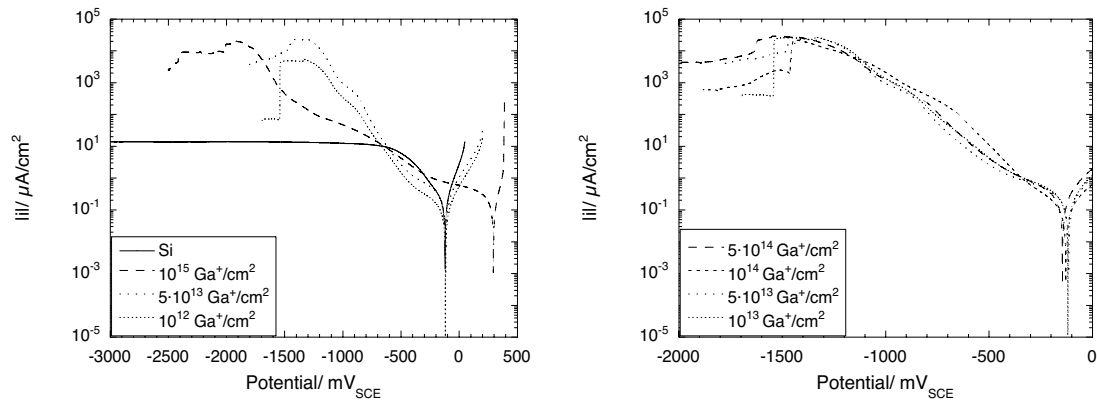
Fig. 4.22: CVC on BII ion implanted *p*-Si. Electrochemical conditions: in 0.05 M H_2SO_4, scanned at 15 mV/s.

The first experiments (figure 4.22) were carried out in a metal-free electrolyte (H_2SO_4) to clarify the effect of the implant dose on the general electrochemical behaviour of the surface. The influence of the ion dose on the CVC is clearly visible in figure 4.22. On unimplanted Si no current increase can be observed at potentials as low as -3000 mV. On the implant sites, however, the following effects are seen:

- Intermediate doses of 10^{13} up to $5 \cdot 10^{14} Ga^+/cm^2$ show a similar behaviour: a more or less constant current increase between -400 mV and -1300 mV, which is probably due to O_2 reduction. The current abruptly decreases at roughly -1500 mV due to the formation of a hydrogen bubble in the microcapillary. A bump in the curve is visible at ~-900 mV which may indicate the onset of H_2 formation.

- For low doses, i.e. $\leq 10^{12} Ga^+/cm^2$ a behaviour similar to the one for intermediate doses can be observed, with the difference that the currents are approximately 5 - 10 times lower. The form of the curve is the same, however.

- Another interesting behaviour is observed for amorphous silicon at $10^{15} Ga^+/cm^2$ (and presumably above): the ocp is shifted from -120 mV to 300 mV and the curve has a different shape. Currents are generally 10 - 100 times lower than those for lower doses. A bump which may indicate onset of H_2 formation is apparent at -1500 mV. The curve abruptly ends at -2000 mV due to the formation of a hydrogen bubble.

The CVC show that a-Si has a unique electrochemical behaviour compared to both unimplanted p-Si and Si implanted with lower doses. The shift of the ocp has –to our knowledge– not yet been discussed in the literature. The generally lower currents may be attributed to the increased resistivity of a-Si (the resistivity of a-Si is generally several orders of magnitude larger than that of crystalline Si [214-216]).

CVCs with electrolyte 1 (0.01 M $CuSO_4$ + 0.05 M H_2SO_4) result in a similar picture (figure 4.23): no current increase on unimplanted Si above what is probably the leakage current of the p-Si/electrolyte diode. In contrast, on a-Si the ocp is shifted towards more anodic potentials by several hundred mVs and the current increase – probably due to Cu-deposition– starting at ~-200 mV is smooth up to roughly -1300 mV. At this point H_2 seems to form as the curve finishes at -2000 mV due to a hydrogen bubble. Moderate implantation doses (figure 4.23, right) all show a similar behaviour: a very steep current increase at -300 mV –caused by the onset of Cu-deposition– and a bump at -400 mV which may be due to the change from crystallite formation to diffusion-limited growth of the crystallites. A second, moderate current increase is seen at -800 mV; this may be caused by H_2 evolution as all the curves end at roughly -1200 mV due to the formation of a hydrogen bubble.
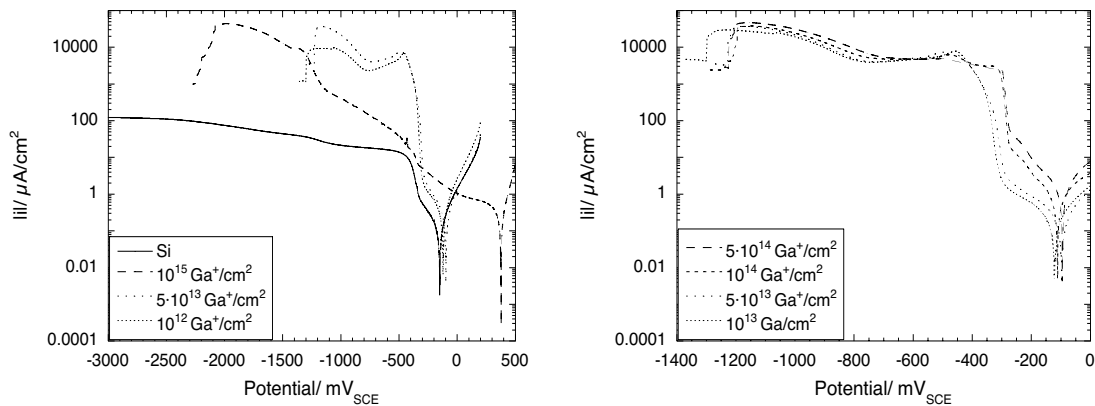
Fig. 4.23: CVC on BII ion implanted p-Si in electrolyte 1 (0.01 M CuSO4 + 0.05 M H_2SO_4), scanned at 15 mV/s.

For the next experiments BTA was added to the Cu-free electrolyte (figure 4.24). A slight shift of the whole curve towards more cathodic potentials as well as slightly decreased currents are the result. While the decreased currents could be expected due to the higher interface resistivity, the shift is rather surprising.
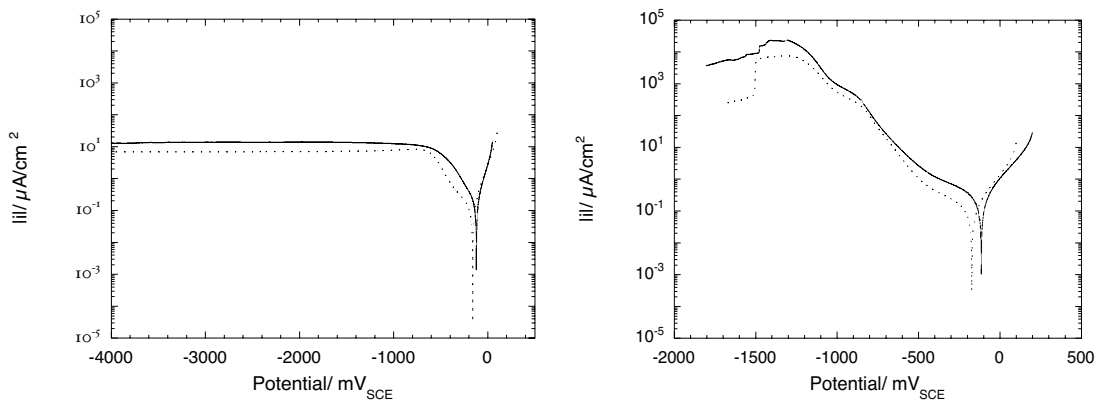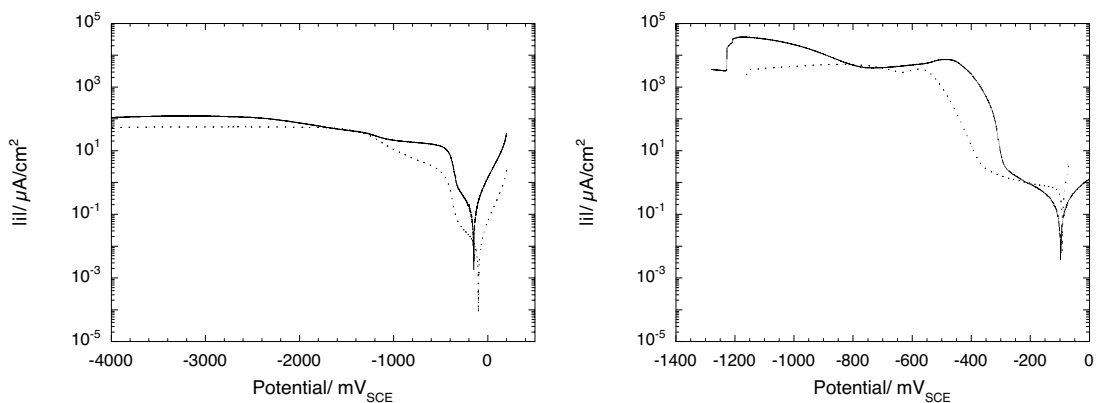

Fig. 4.24: CVC on intact *p*-Si (left) and BII ion implanted *p*-Si (right, dose: $5 \cdot 10^{13}\,Ga^+/cm^2$) in $0.05\,M\,H_2SO_4$ with ($\cdots$) and without (——) 0.1 mM BTA, scanned at 15 mV/s.

In a Cu containing electrolyte the behaviour is similar: the addition of BTA leads to slightly reduced deposition currents and a slight shift of the Cu deposition onset towards more cathodic potentials (figure 4.25).

Fig. 4.25: CVC on intact *p*-Si (left) and BII ion implanted *p*-Si (right, dose: $5 \cdot 10^{13}\,Ga^+/cm^2$) in electrolyte 1 (——) and in electrolyte 2 ($\cdots$), scanned at 15 mV/s.

In conclusion, microelectrochemical techniques made it possible to collect precise information on the influence of implantation doses and BTA on the deposition process. BTA has a weak albeit visible effect on the CVCs: the current densities are slightly reduced and Cu onset is shifted towards more cathodic potentials.

4.3.6 Current Transients

Current transients during potentiostatic experiments are a valuable tool to investigate the deposition (nucleation and growth behaviour) of metallic species on semiconductor surfaces [20, 52]. Figure 4.26 shows transients obtained with a microcapillary on implanted p-Si only. By means of combining current-transients with microelectrochemical techniques it is possible to study the nucleation and growth behaviour independently of any unintentional defects.

All transients show an initial current increase (due to nucleation), followed by a decrease caused by the diffusion limited growth of the individual nuclei. The deposition is slower after the addition of BTA to the electrolyte, as can be seen by the lower and broader peaks in figure 4.26right compared to the transients in BTA-less electrolyte (figure 4.26, left). Only after ~ 2 - 5 s the diffusion limited current is reached.
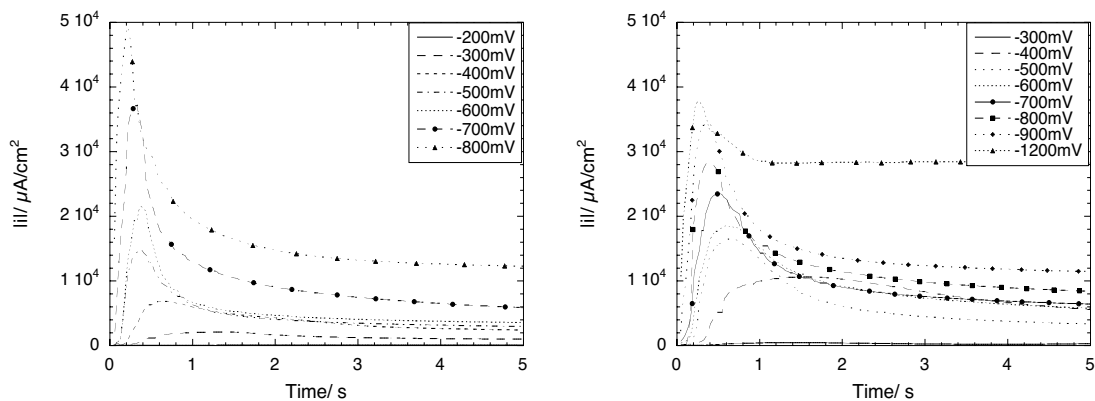
Fig. 4.26: Current transients for the deposition of Cu onto BII ion implanted p-Si (Dose: $10^{14}\,Ga^+/cm^2$). Left: electrolyte 1; right: electrolyte 2.

The shape of these current transients can be used to determine the nature of the nucleation process. Scharifker *et al.* [217] have developed a model for both instantaneous and progressive nucleation and have derived the following equations for the current transients in the case of instantaneous (formula 4.2) and progressive (formula 4.3) nucleation:

$$\left(\frac{i}{i_{\max}}\right)^2 = \frac{1.9542}{t/t_{\max}}\left\{1-\exp\left(-1.2564\frac{t}{t_{\max}}\right)\right\}^2 \quad \text{instantaneous nucleation} \quad (4.2)$$

$$\left(\frac{i}{i_{\max}}\right)^2 = \frac{1.22542}{t/t_{\max}}\left\{1-\exp\left[-2.3367\left(\frac{t}{t_{\max}}\right)^2\right]\right\}^2 \quad \text{progressive nucleation} \quad (4.3)$$

where $i_{\max}$ signifies the maximum current density and $t_{\max}$ the time of maximum current flow. i and t stand for current and time respectively.

We have plotted these values together with those measured for the above transients in the dimensionless form in figure 4.27; to make the graph more readable, the values for only two potentials (a low one and a high one) are shown. The experimental values follow approximately the curve predicted for the case of progressive nucleation. The graph further shows that, for more cathodic potentials, the model seems to break down in the case of electrolyte 1: while the curve first appears to follow that of a progressive nucleation behaviour it deviates considerably later on. In the case of a BTA containing electrolyte, more cathodic potentials lead to a more 'progressive' behaviour.
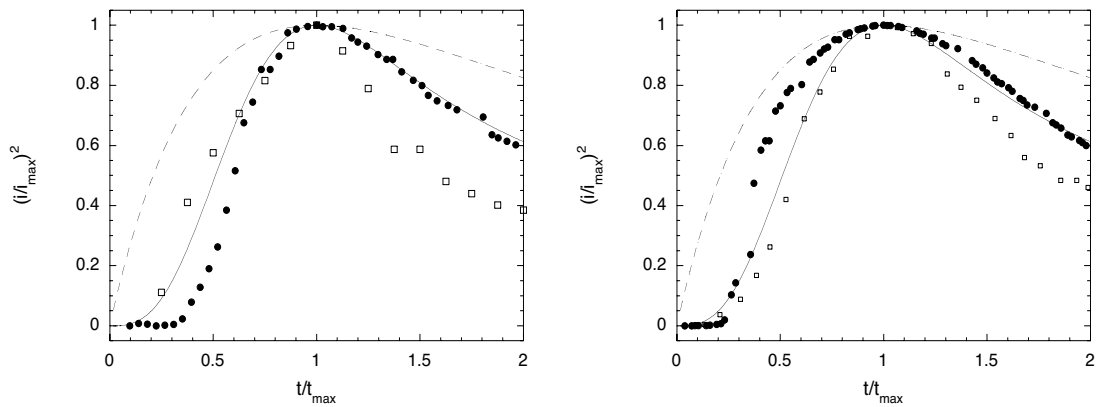
Fig. 4.27: Dimensionless plot of current transients from figure 4.26 at -400 mV (●) and at -800 mV (□); for comparison the model for progressive (——) and instantaneous (···) nucleation are shown. Left: in electrolyte 1; right: in electrolyte 2.

The development of i_{max} and t_{max} was plotted as a function of the applied potential in figure 4.28. While i_{max} varies linearly with the applied potential, t_{max} shows an exponential behaviour.
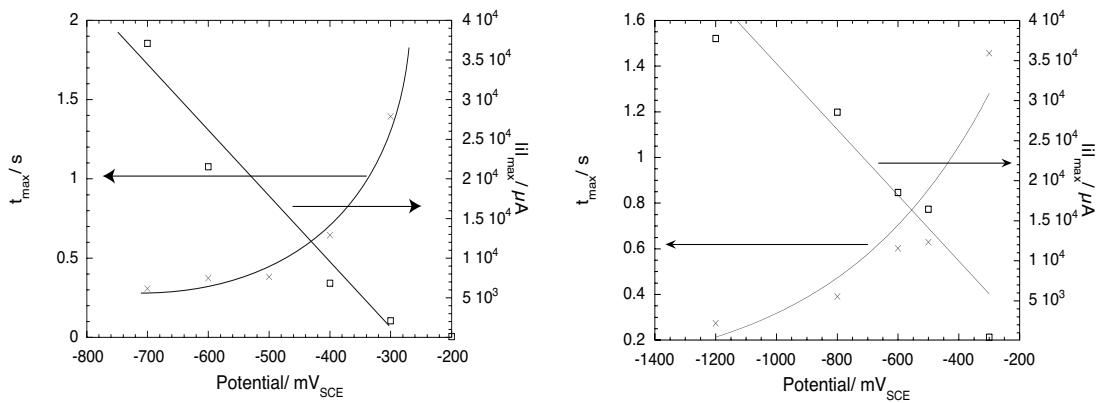
Fig. 4.28: Development of t_{max} and $|i|_{max}$ as a function of the applied potential in left: electrolyte 1 and right: electrolyte 2.

We can therefore assume that the diffusion coefficient depends on the applied potential and can be calculated according to [138]

$$D = \frac{i_{max}^2 t_{max}}{0.2598(zFc)^2} \qquad (4.4)$$

where zF designates the molar charge of the electrodepositing species and c the bulk concentration. The development of the diffusion coefficient, D, is shown below (figure 4.29). As expected, the diffusion coefficient increases exponentially over time [138]. Surprisingly, BTA seems to be effective only at more cathodic potential, while the previous results suggested a different behaviour. However, it may also be that, at potentials above -500 mV, deposition proceeds very slowly no matter whether BTA is added to the electrolyte or not, and that natural fluctuations in the deposition process are predominant.
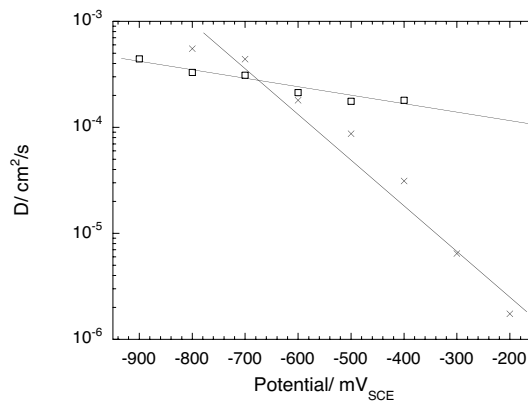
Fig. 4.29: Diffusion coefficient, D, as a function of the applied potential in electrolyte 1 (×) and in electrolyte 2 (□).

4.3.7 FIB vs. BII implanted p-Si

As seen in chapter 4.2 FIB and BII implanted p-Si show some fundamental differences with respect to amorphization behaviour. So far all the CVCs presented therefore came from BII implanted samples. In this chapter we will explore whether the differences found by Raman spectroscopy are reproduced by electrochemical experiments.

According to the findings in figures 4.11 and 4.12 one would expect a similar behaviour for FIB and BII implanted samples if the ion dose is 50 to 100 times larger in the FIB implanted samples. Figure 4.30 shows that this seems to be the case indeed: deposition is severely impeded due to the amorphization of the substrate. At an implant dose of $10^{15}\,Ga^+/cm^2$, where no significant deposition took place on BII implanted samples, one obtains perfect coverage of the implant combined with high selectivity. Only for samples implanted at $10^{17}\,Ga^+/cm^2$ and beyond the masking effect due to the amorphization of the substrate occurs.
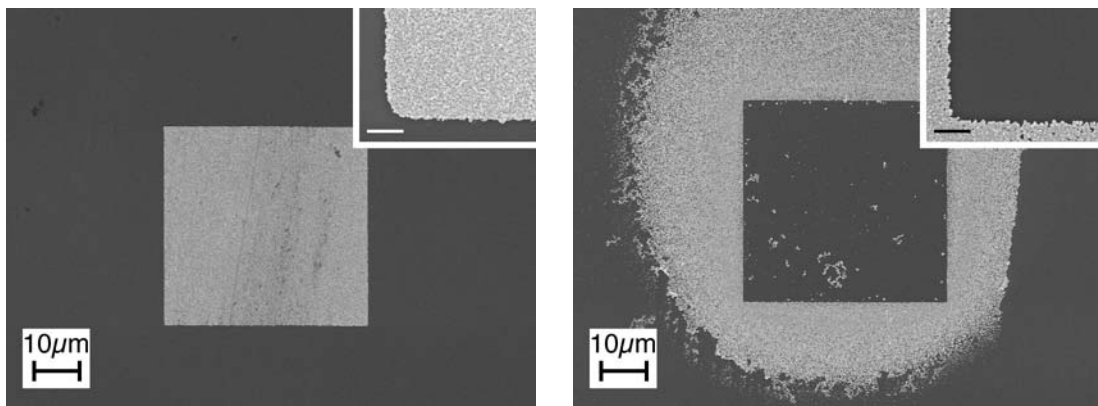
Fig. 4.30: SEM pictures of ion implanted p-Si. Deposition took place in electrolyte 2, 15 s at -1500 mV. Left sample implanted with $5 \cdot 10^{15}\,Ga^+/cm^2$, right sample with $10^{17}\,Ga^+/cm^2$. The insert shows a magnification of the bottom left corner, the marker is 1 μm.

Figure 4.31 further supports these results: for FIB implanted samples doses lie roughly 100 times above those of BII implanted samples when similar effects (i.e. good deposition at intermediate implant dose in the left figure vs. impeded deposition for a-Si in the right figure) are observed. Figure 4.31, left shows the characteristic CVC for good deposition: a marked current increase over several orders of magnitude at roughly -350 mV (due to the onset of deposition) followed by a slight decrease and a stable high-current phase (probably growth at the diffusion limited current). Figure 4.31, right shows the behaviour observed previously for a-Si: the ocp is shifted to more anodic values by several hundred mV and the

current increase is less marked and more continuous. The FIB implanted sample shows a more marked increase than the BII treated sample. We assume that this is due to the linear writing mode of the FIB: even for prolonged FIB exposure it is quite likely that overlapping of the beam is not always perfect, leading to zones of lower implant density.
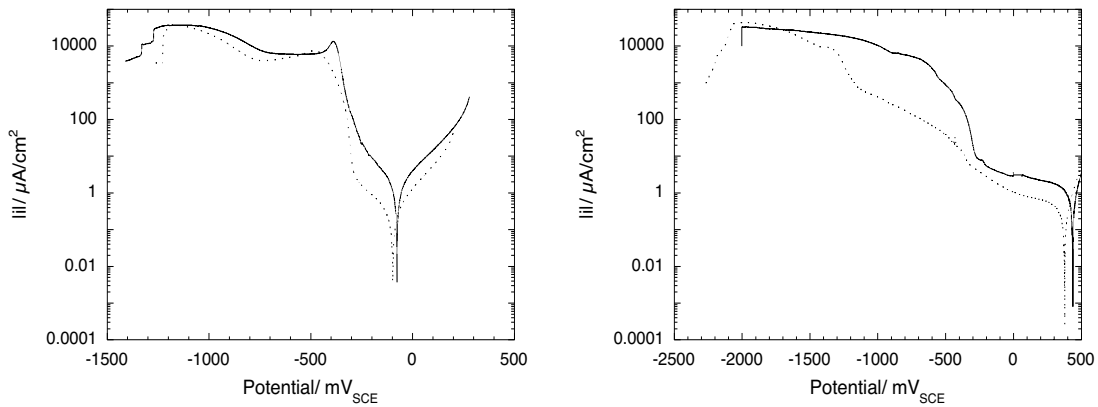
Fig. 4.31: CVCs of samples implanted by FIB(—) and by BII ($\cdots$) at 30 keV and at 29.6 keV respectively. Dose left: $5 \cdot 10^{15}\,Ga^+/cm^2$ (FIB) and $5 \cdot 10^{13}\,Ga^+/cm^2$ (BII); dose right: $10^{17}\,Ga^+/cm^2$ (FIB) and $10^{15}\,Ga^+/cm^2$ (BII)

4.3.8 Characterization of Cu Deposits

a)   Electrical Properties

Solid state I/V characteristics for Cu electrodeposited onto p-Si exhibit a Schottky diode behaviour (figure 4.32). For cathodic potentials a quasi blocked current can be observed while the anodic branch is in the passing state.
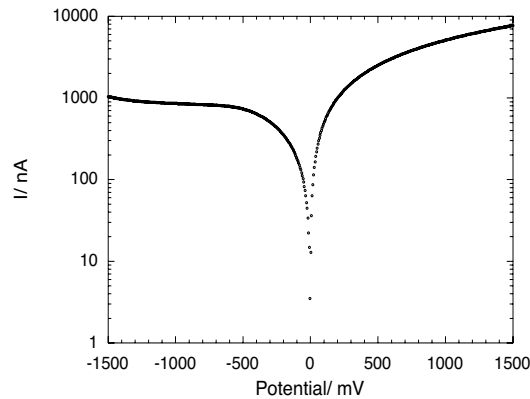
Fig. 4.32: Solid state *I/V* characteristics of electrodeposited *p*-Si/Cu junction (massive Cu deposition, 2 min at -3000 mV in electrolyte 2).

Conductivity measurements were performed on one sample with a 40 µm square and on a sample with a 400 µm square by four-point probe. Resistivity for these samples was similar (the small sample showed slightly higher values) and were roughly 20 % above those for pure Cu (15.4 nΩm); for comparison, Al has a resistivity of 24.2 nΩm.

b)   'Ultimate' Resolution

So far, only relatively large structures have been investigated. One of the goals of this work was however to determine the 'ultimate' resolution of the deposition process. The examples shown below represent our best efforts for Cu deposition on FIB implanted *p*-Si with respect to resolution. While it is likely that better results can be obtained with more sophisticated electrolytes, we are confident that the examples below are close to what is currently possible in terms of resolution with this system. In these cases a more concentrated electrolyte was used, which proved to be advantageous for small structures.

When using FIB implantation to produce damage, energy and dose have to be carefully selected. While theoretical considerations seem to suggest that electrochemistry works better on samples implanted at lower energy, resolution is drastically decreased in that case. Therefore, all high-resolution samples were implanted at 29.6 keV. After electrodeposition

tightly spaced Cu lines with a resolution of < 500 nm were obtained over several 10s of μm (figure 4.33). The lines are however rather coarse, although it is impossible to say whether this is due to shortcomings of the electrochemistry only, or if the implanted lines were not well defined to begin with.
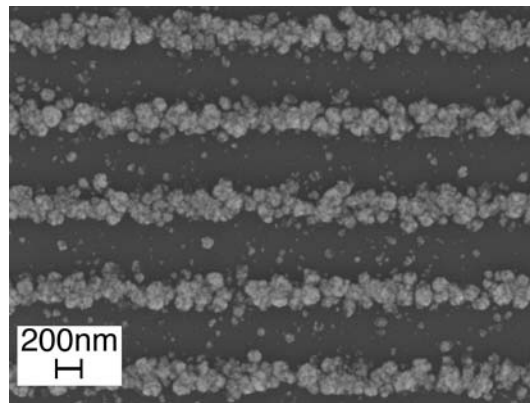
Fig. 4.33: Series of Cu-lines obtained on FIB implanted p-Si showing a resolution of 300 nm. Conditions: Sample implanted with $10^{15}\,Ga^+/cm^2$ at 29.6 keV, electrolyte: 1 M H_2SO_4 + 0.05 M $CuSO_4$ + 0.1 mM BTA, deposition at -1500 mV for 20 s.

Using lower implantation doses, even finer lines could be obtained with identical electrochemical parameters (figure 4.34). This might indicate that subtle effects occurring during ion-implantation, mainly the large intensity distribution over the beam diameter as shown in figure 4.5, probably plays a role for closely spaced implants. It is quite remarkable to see how the line width depends on the implantation dose. An increase by as little as a factor of 2 may also double the line width. These effects are not predicted by SRIM calculations and show how strongly the electrochemistry reacts to substrate changes.
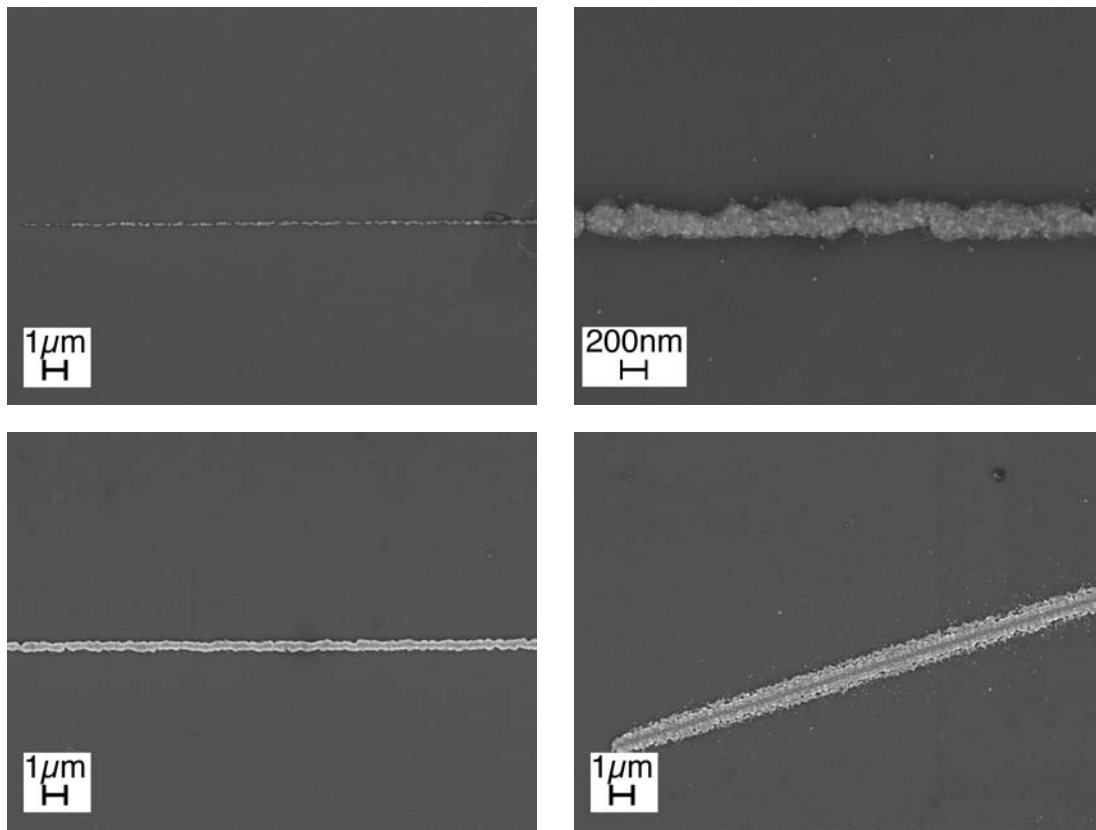
Fig. 4.34: Resolution dependence on implant dose. All samples implanted by FIB at 29.6 keV. Cu deposited from 1 M H_2SO_4 + 0.05 M $CuSO_4$ + 0.1 mM BTA at -1500 mV for 20 s. The implant dose is (from top left to bottom right): 10^{13} Ga^+/cm^2, $5 \cdot 10^{13}$ Ga^+/cm^2, 10^{14} Ga^+/cm^2, 10^{15} Ga^+/cm^2.

c)   Surface Analysis

The Cu structures obtained were characterized extensively by optical microscopy and SEM. These pictures have been shown and commented on before (e.g. figure 4.34) and will therefore not be taken into consideration in this section. We have also analysed some samples using AFM. The advantage of this approach lies in the fact that the height of the deposits, in addition to their width, can be measured precisely.
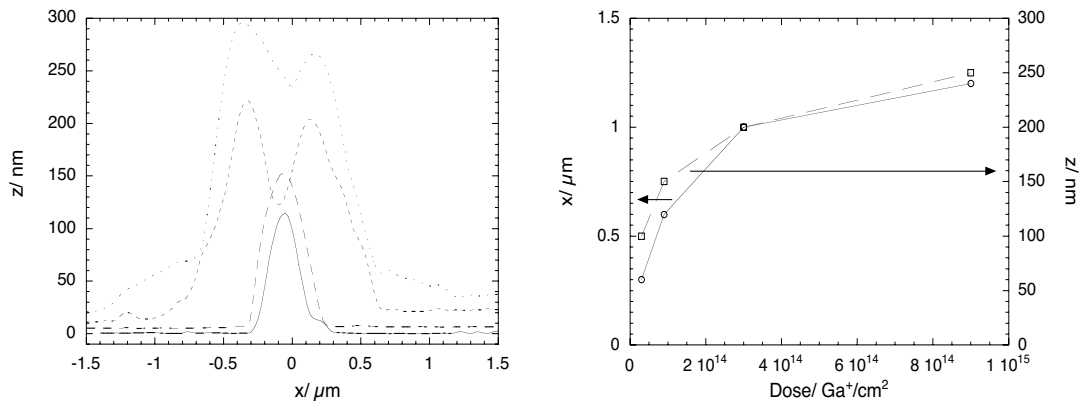
Fig. 4.35: AFM analysis of Cu lines presented in figure 4.34. Left: AFM profiles, right: variation of deposit thickness and width with implant dose.

Figure 4.35 shows how the thickness of a deposit varies with increasing implant concentration (all other factors remaining constant), indicating that growth occurs faster with higher implant concentrations. For implant concentrations higher than the ones shown in figure 4.35 (right) two phenomena usually occur: often outgrowth is observed –i.e. the implant width can no longer be assessed– and the implant is no longer fully covered as the substrate may become amorphous at these doses, effectively acting as a mask. Deposition starts at the borders of the implant but does not fully cover it, which is probably due to an uneven dose distribution over the implant surface: the concentration is highest at the centre, therefore amorphization is most complete and electrochemical reactions are severely limited[18].

Samples were also analyzed by scanning AES to determine whether Cu was deposited in small quantities at locations where SEM pictures would not indicate it (e.g. between the lines of figure 4.33). This might be the case for very thin Cu layers (one monolayer or less). AES analysis (figure 4.36) shows that this is not the case, i.e. Cu is only deposited at the ion implant sites.

---

18. While Raman measurements indicated amorphisation only at doses of 10^{16} - 10^{17} Ga$^+$/cm^2, the samples presented here were implanted with lower current fluences (for better resolution), which would probably lead to lower needed for amorphisation. However, measurements on single line scans did not yield any useful results, probably because the sample area was too small.
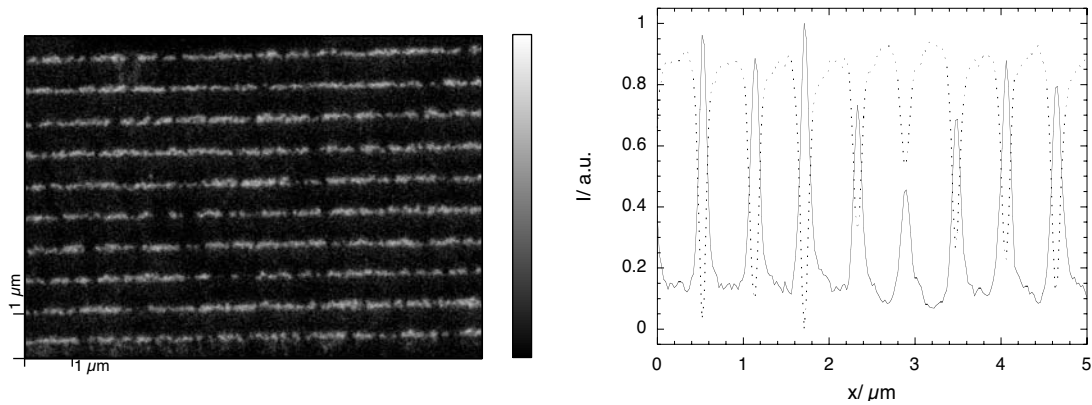
Fig. 4.36: Scanning AES image of sample showing closely spaced lines of Cu (white indicates high Cu concentration). Right: Scanning AES profile showing Cu (solid line) and Si (broken line) intensity.

d)   Energy Model of the Deposition Process

In order to establish an energy model of the deposition process, different values such as the flatband potential, V_{fb}, the Schottky barrier, U_{Sb}, the breakdown potential, U_{bd}, the deposition potential, U_{d}, and others have to be measured or calculated.

Mott-Schottky plots are a valuable tool to determine some of the solid-state characteristics of the silicon used; according to equation 2.6, both V_{fb} and the doping concentration, N_{D}, can be derived from it.
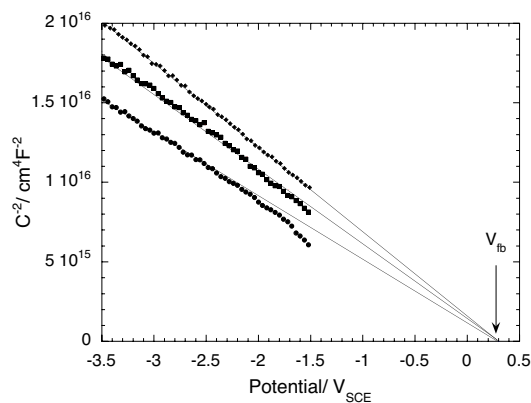

Fig. 4.37: Mott-Schottky plot for p-Si (100) in 0.05 M H_2SO_4 (◆ 50 kHz, ■ 10 kHz, ● 1 kHz); all experiments performed at a scanning speed of 1 mV/s (in cathodic direction) and a perturbation of 10 mV.

The interpolation of the plot (figure 4.37) to a value of $1/C^2=0$ provides the flat band potential. In our case $V_{fb}=0.3\,V$, which is in good agreement with values reported in the literature [218]. The doping concentration, N_D, can be obtained from the slope of the curve and is roughly $4\cdot10^{15}\,at/cm^3$; this is in agreement with values obtained from four-probe measurements which gave a doping concentration of $0.5\cdot10^{15}\,at/cm^3$ and a resistivity of $9.85\,\Omega cm$. Using the value of the flat band potential, it is possible to calculate the Schottky barrier, U_{Sb}, of the semiconductor-electrolyte interface according to:

$$U_{Sb} = E_F - E_{v,s} \text{ where } (E_{v,s} = E_{c,s} - E_g) \qquad (4.5)$$

E_F can be measured (it is equal to E_{redox}), E_g is known (1.12 eV for Si) and $E_{c,s}$ can be calculated according to equation 4.6:

$$E_{c,s} = eV_{fb} + kT\ln\frac{N_C}{N_D} \qquad (4.6)$$

where e is the elementary charge of an electron, k the Boltzmann constant, and N_C the effective density of states in the conduction band (according to Sze [128] N_C for Si is $2.8\cdot10^{19}\,at/cm^{-3}$). We therefore obtain for $E_{c,s}$ approximately -0.53 V and – according to formula 4.5– for $E_{v,s} = 0.59\,V$. From figure 4.25 we obtain a value for E_F^{SC} (which is equal to the redox potential for Cu^{2+}/Cu) of -0.173 V. If this is plotted along the energy axis we obtain figure 4.38.
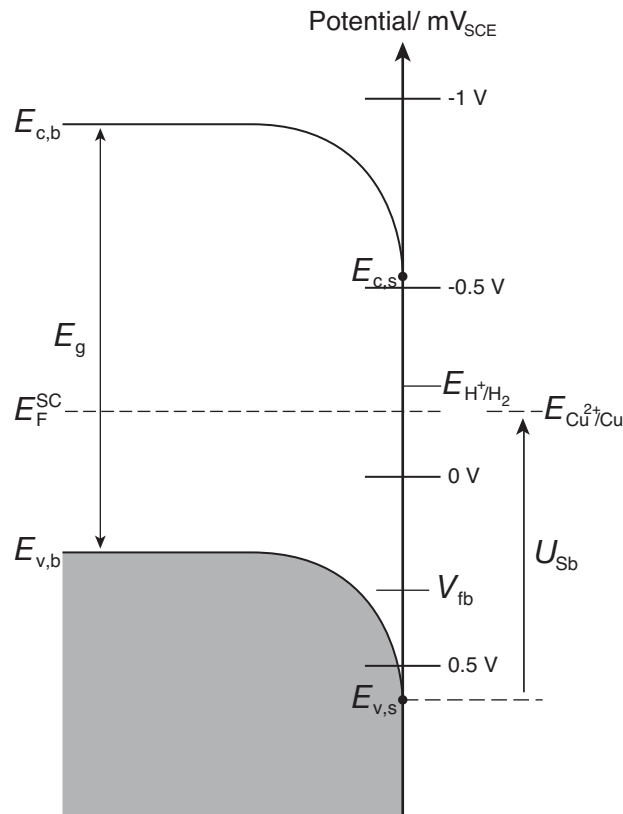
Fig. 4.38: Energy levels for the deposition of Cu on ion implanted p-Si ($5 \cdot 10^{13}$ Ga$^+$/cm^2 at 30 keV by BII in electrolyte 2).

According to figure 4.38 the Schottky-barrier is roughly 0.73 eV, which is rather high (and explains the high breakdown potential measured in figure 4.22). Therefore one would not expect any charge transfer (i.e. Cu deposition) at ocp. Figure 4.39 (which is a magnification of figure 4.25, right) shows, however, that deposition takes place at potentials close to ocp (in reverse scan direction). We can therefore assume that the Schottky diode has broken down and that charges are transferred from the SC's valence band to the electrolyte.
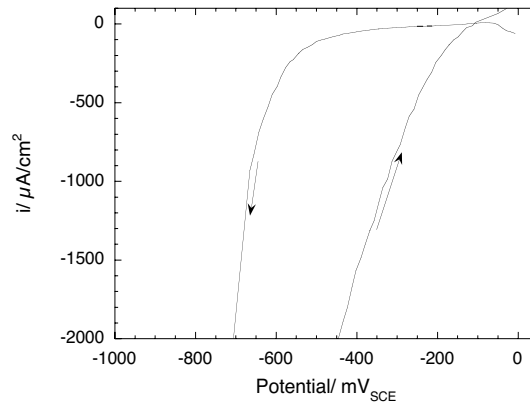
Fig. 4.39: Voltamogram of Cu deposition from electrolyte 2 onto ion implanted *p*-Si (implanted by BII at 30 keV, $5 \cdot 10^{13}$ Ga$^+$/cm^2)

4.4 Electrochemical Deposition of Gold Structures on Ion Implanted *p*-Si

In order to obtain a broader overview over the electrochemical behaviour of ion implanted *p*-Si, experiments were also performed in a basic, Au containing electrolyte. According to the literature [52], the following electrolyte allows to perform fundamental studies on the nucleation and growth behaviour of Au deposits on Si while allowing sub-micrometer resolution [219]: 0.01 M KAu(CN)$_2$ + 1 M KCN (electrolyte 3).

4.4.1 Macroscopic Current-density/Voltage Curves

The behaviour of an intact and of a scratched *p*-Si surface was investigated (figure 4.40) and compared to that in electrolyte 1 (figure 4.1). Some important differences are apparent:

- The ocp is slightly shifted towards more cathodic potentials by the scratches.
- A marked difference can be seen between the scratched and the intact surface; visual inspection reveals that only the scratched surface shows massive Au deposits.
- The onset of Au deposition does not take place at a well defined potential; it rather occurs over time.
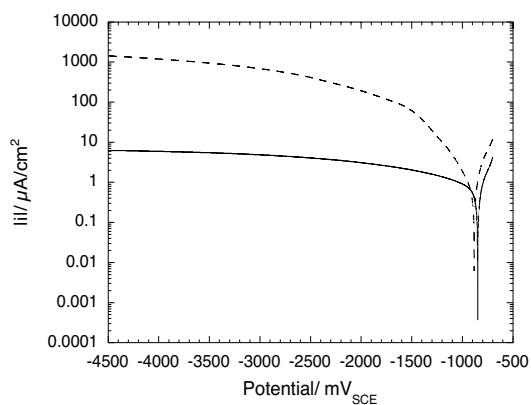
Fig. 4.40: CVC on intact (solid line) and scratched (broken line) *p*-Si in electrolyte 3 (scanning speed: 15 mV/s)

4.4.2 Influence of Implantation Dose, Deposition Time, and Potential

Similar to the experiments performed before (chapter 4.3.1) we first tried do determine the influence of the implantation dose, which was previously demonstrated to be the most important parameter for useable metal deposits. Figure 4.41 shows that the electrochemical behaviour in a Au-containing electrolyte is quite different from the Cu containing ones: while all the deposits are finely grained with crystallite sizes around 50 nm and less, selectivity is more difficult to obtain.
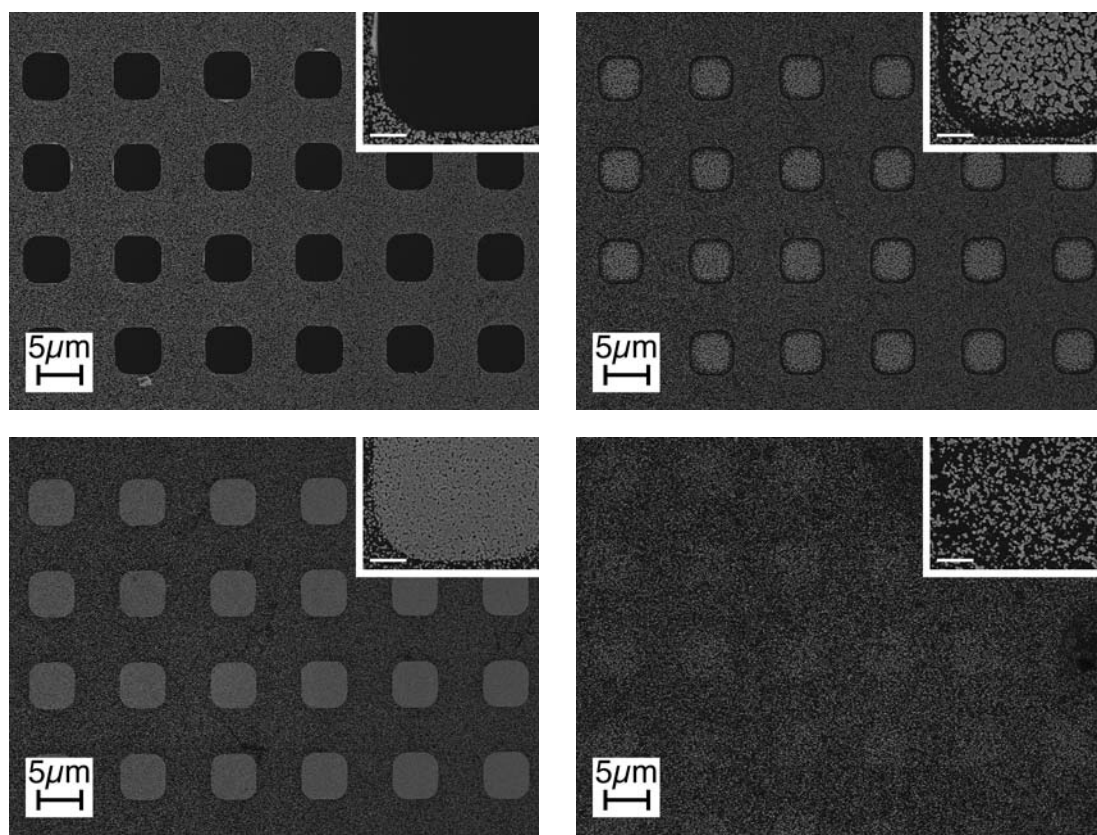
Fig. 4.41: SEM pictures of ion implanted *p*-Si. Samples implanted at 30 keV with varying doses of Ga$^+$ by BII. Electrochemical conditions: 15 s in electrolyte 3 at -2500 mV. Ion dose (from top left to bottom right): 10^{15} Ga$^+$/cm^2, $5 \cdot 10^{14}$ Ga$^+$/cm^2, $5 \cdot 10^{13}$ Ga$^+$/cm^2, 10^{12} Ga$^+$/cm^2. The insert shows a magnification of the bottom left corner, the marker is 1 μm.

Once the amorphization threshold has been reached, a masking effect can be observed. It also seems that the Au crystallites grow slower than the Cu ones: even under optimum conditions ($5 \cdot 10^{13}$ Ga$^+$/cm^2) the deposit does not fully cover the implant. It is therefore interesting to consider the influence of the deposition time on the deposited metal structure: As seen in figure 4.42, it is quite difficult in this system to obtain good deposit structure while maintaining selectivity. It seems that either Schottky barrier breakdown takes place much more easily in this system than in the Cu system (a hypothesis not necessarily supported by the CVCs in figure 4.40), or that the crystallites formed initially are more mobile and tend to diffuse on the surface.
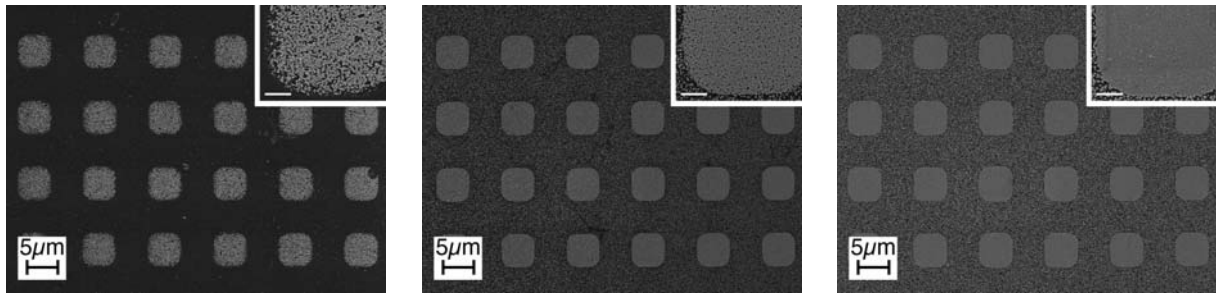
Fig. 4.42: SEM pictures of ion implanted p-Si. Samples implanted at 30 keV with $5 \cdot 10^{13}$ Ga$^+$/cm^2 by BII. Electrochemical conditions (from left to right): 2 s, 15 s, 30 s in electrolyte 3 at -2500 mV. The insert shows a magnification of the bottom left corner, the marker is 1 µm.

We then tested if longer exposure at lower potentials would lead to more satisfying results but –as can be seen below in figure 4.43, left– were not successful. In this system the balance between deposition potential and time is more difficult to determine than for a Cu containing electrolyte.

To test the masking effect of the amorphous silicon in this system, one sample was deposited at -4000 mV for 30 s. As can be seen in figure 4.43, right, the implant remains entirely deposit-free while the untreated substrate is covered by an almost perfect Au-layer. According to the CVC of intact Si (figure 4.40) Au should not be deposited at -4000 mV. We therefore assume that the deposition process started at the border of the implanted region, similar to the effect seen e.g. in figure 4.30, and proceeded from there. Experiments with more widely spaced implants under the same electrochemical conditions confirmed this assumption: outgrowth to some 15 µm away from the border was observed, which would be sufficient to completely cover the surface between the implants on the sample below.
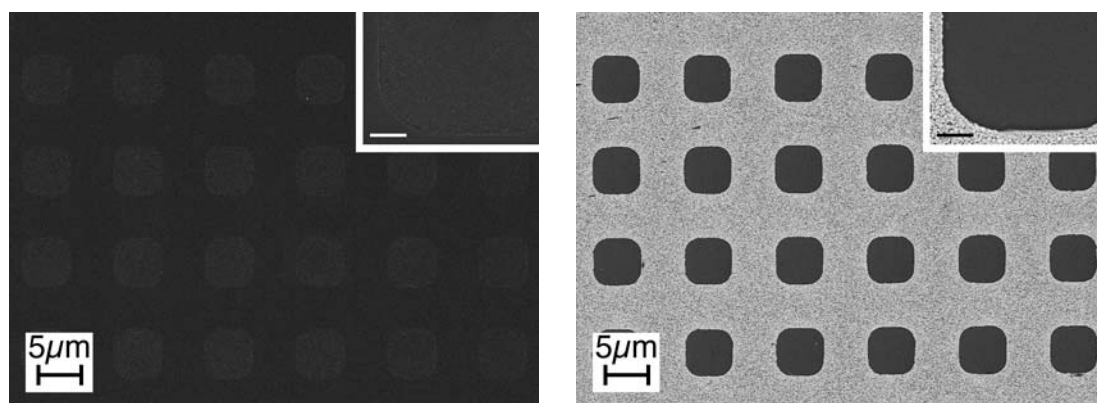
Fig. 4.43: SEM pictures of ion implanted *p*-Si. Samples implanted at 30 keV with $5 \cdot 10^{13}$ Ga$^+$/cm^2 (left) and 10^{15} Ga$^+$/cm^2 (right) by BII. Electrochemical conditions 30 s at -1300 mV (left) and 30 s at -4000 mV (right) in electrolyte 3. The insert shows a magnification of the bottom left corner, the marker is 1 μm.

4.4.3 Microelectrochemical Current-Density/Voltage Curves

Microcapillary measurements were again used to determine the influence of the ion implantation dose on the deposition behaviour (figure 4.44). Varying the ion implant dose has similar effects as seen before (figure 4.24): for an implant dose above the amorphization limit a moderate current increase stretching over several hundred millivolts is observed; the final currents are slightly lower than those observed for intermediate implant doses. At implant doses between $5 \cdot 10^{14}$ - $5 \cdot 10^{13}$ Ga$^+$/cm^2 a steep increase at a clearly defined potential (-1400 mV) takes place. We assume that Schottky barrier breakdown takes place at this potential, and that the strong current increase is caused by the massive nucleation and growth of crystallites while the almost constant current at potentials of -2000 mV and beyond is due to diffusion limited growth of the crystallites.
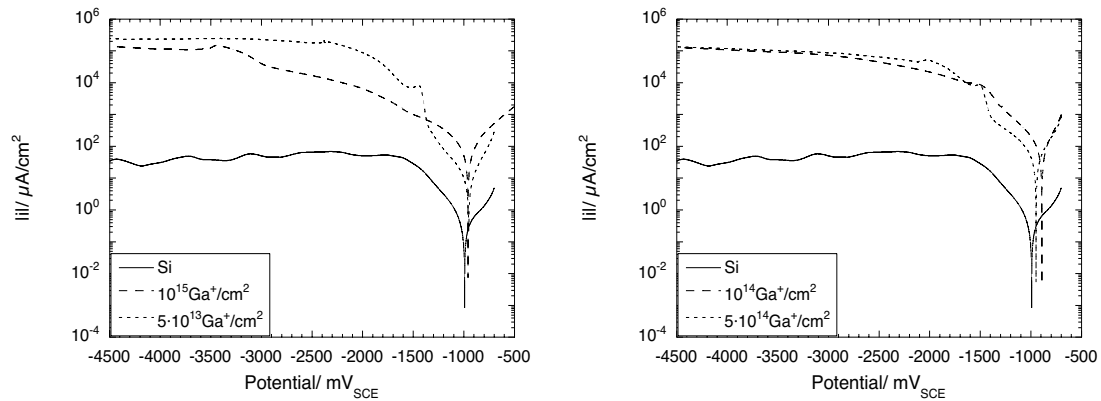
Fig. 4.44: CVC on BII ion implanted p-Si. Electrochemical conditions: scanned at 15 mV/s in electrolyte 3.

SEM pictures presented above seem to support this assumption: at $10^{15}\,Ga^+/cm^2$ no Cu was deposited on the implant but only around it. We assume that this is caused by a massive outgrowth starting at the implant border where an ion dose gradient must exist; the deposition process starts at these low implant dose regions and spreads from there. The almost perfect masking effect of the amorphous Si may be explained by its high resistivity: four point probe measurements showed that the amorphous zones had a resistivity roughly 100 times higher than that of crystalline Si.

4.4.4 Current Transients

Current transients were obtained on ion implanted Si in electrolyte 3 (figure 4.45, left). As expected, we observed higher currents and shorter peak times for higher applied potentials. The dimensionless plot (figure 4.45, right) further shows that, in the case of an Au containing basic electrolyte, deposition proceeds according to the model for instantaneous deposition. I.e. most of the crystallites are formed very early during the deposition process, and the whole surface is being covered at once. This may explain the very fine granularity of the Au deposits.
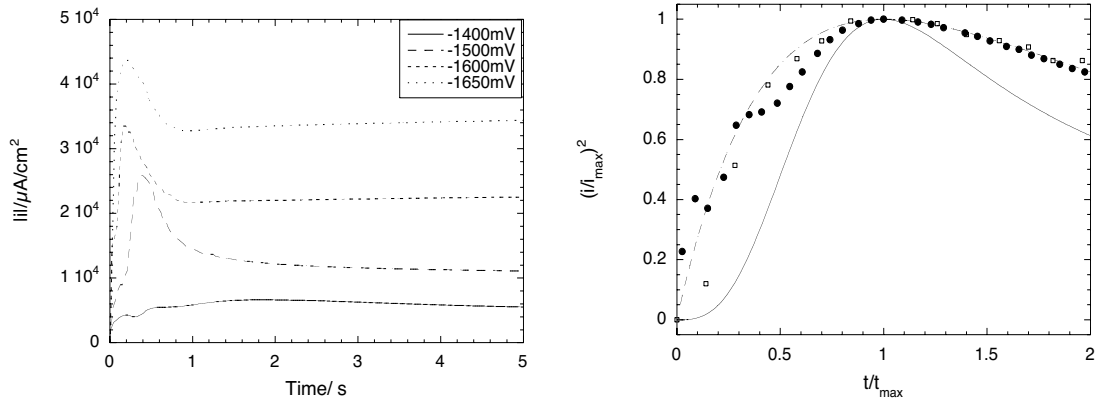
Fig. 4.45: Left: Current transients in electrolyte 3 on BII implanted p-Si, $10^{14}\,\text{Ga}^+/\text{cm}^2$; right: dimensionless representation of transients at -1400 mV (●) and at -1600 mV (□) as well as theoretical plots for progressive (——) and instantaneous (⋯) nucleation.

Figure 4.46 shows similar conditions as for Cu containing electrolytes: the time of maximum current-density, t_{max}, depends exponentially on the applied potential, while the maximum current-density, i_{max}, varies linearly. As the Au crystallites follow an instantaneous nucleation behaviour, the formula to obtain the diffusion coefficient, D, is slightly different from before [138]:

$$D = \frac{i_{\text{max}}^2 t_{\text{max}}}{0.1629(zFc)^2}$$

$$(4.7)$$

D varies with the applied potential and shows an exponential behaviour. The values obtained for D are comparable to the ones obtained in electrolyte 2.
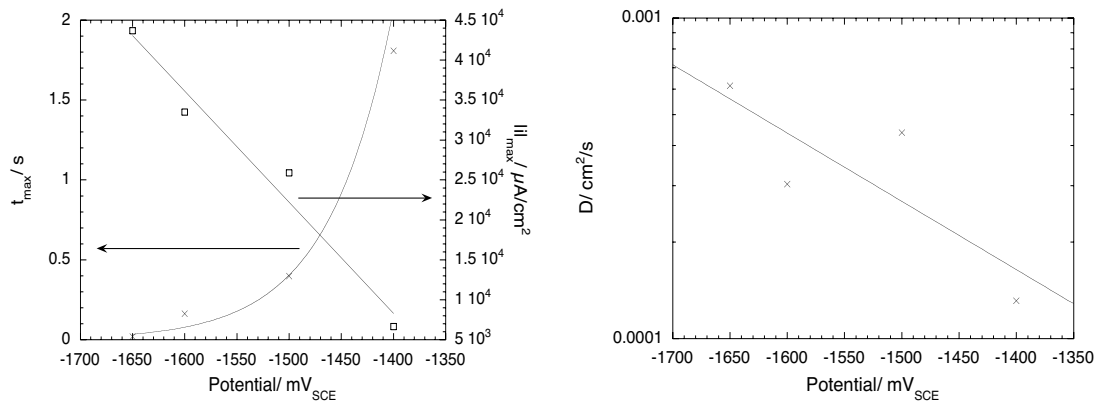
Fig. 4.46: Left: dependence of t_{max} and i_{max} on the potential; right: diffusion coefficient, D, as a function of the applied potential (all values derived from figure 4.45)

4.4.5 Comparison Between Gold and Copper Electrodeposition

The investigations of the electrochemical behaviour of ion implanted p-Si in Cu and Au-containing electrolytes presented in the previous chapters can be summarized as follows:

- While Cu shows a progressive deposition behaviour, Au is deposited in an instantaneous process. This may explain why Au crystallites are usually smaller than Cu crystallites and why Au deposition is more sensitive to the applied potential.
- Cu based electrolytes show massive dendritic deposits if no precautions are taken (i.e. if no BTA is added); Au containing electrolytes behave differently and seem to produce slowly growing spherical crystallites.
- Outgrowth is more of a problem with Au-structures, while Cu structures showed clean borders.
- In general, the BTA containing Cu-electrolyte yielded the best results with respect to resolution, coverage, and outgrowth.

4.5 Ion Projection Direct Structuring Based Pattern Generation

The last experiment was aimed at determining the potential for industrial applications of the selective electrochemical deposition process. The main drawback of this technique, as presented so far, lies in its linear writing approach which makes the production of complicated structures or large sample volumes time consuming. If the linear FIB writing process is replaced by a parallel method for pattern reproduction, such as ion projection direct structuring, IPDS, sample through-put can be increased significantly. It remains to be tested if this technique offers the same resolution as FIB-based operation.

The use of IPDS also provided an opportunity to determine the influence of the ion species used for defect creation. By comparing CVCs obtained for different ions and implant doses, it is possible to learn more about the influence of the damage created.

Figure 4.47 shows polarisation curves for Ar^+ and Xe^+ implanted samples. The same behaviour as for Ga^+implanted samples is observed: higher implantation doses lead to an increased current. Again, an optimum dose exists beyond which deposition currents become smaller again ($10^{14}\,Ar^+/cm^2$ and $5\cdot10^{13}\,Xe^+/cm^2$). Although Raman spectra were not taken of these samples, it is reasonable to assume that the mechanism responsible for the current decrease at high doses is amorphization of the substrate (refer to chapter 4.2).
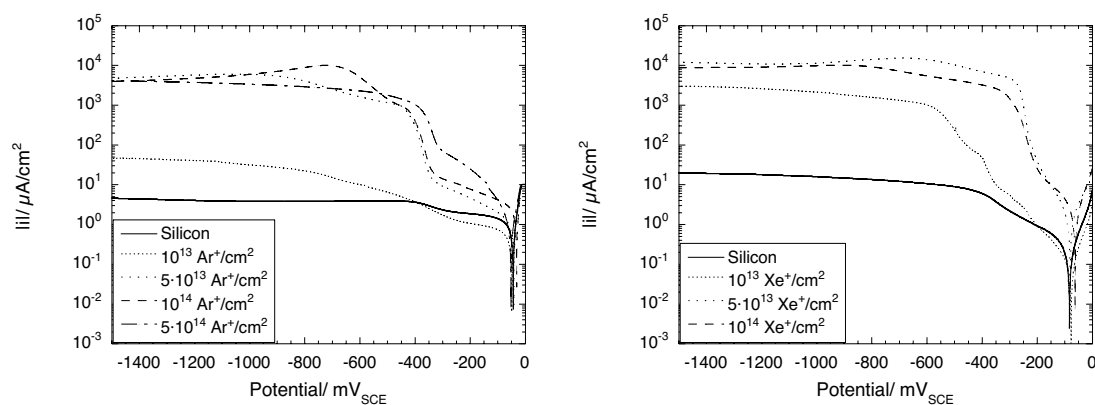
Fig. 4.47: Current-density/voltage curves for IPDS implanted p-Si. Left: Ar^+, right: Xe^+. Both samples implanted at 75 keV by IPDS, electrochemical conditions: electrolyte 2, scanning speed 15 mV/s.

We have tried to represent the current vs. implant dose behaviour in figure 4.48, where the current at -1500 mV is reported as a function of the ion dose. This potential was chosen because it is sufficiently far away from the onset of deposition to make sure that a slight shift in ocp would not have any effect. Higher potentials were not used, in order to minimize the influence of hydrogen bubbles which might begin to form.

The graph illustrates the following:

- An amorphization dose beyond which the deposition current decreases again can be determined for these systems. It lies at $10^{15} Ga^+/cm^2$ (at 30 keV), $5 \cdot 10^{13} Xe^+/cm^2$ (at 30 keV), and $10^{14} Ar^+/cm^2$ (at 75 keV) which is comparable to values found in the literature [208].

- Heavier ions need lower doses to achieve optimum deposition conditions. It can therefore be assumed that the implantation duration can be decreased by use of heavier ions. This effect has been used e.g. in ion intermixing experiments where the use of Xe+ instead of Ar+ has considerably decreased the time needed for intermixing of two adjacent metallic layers [190].

- Deposition currents directly reflect implant profiles: the deeper the main damage zone, the lower the current. Therefore use of light ions at high acceleration voltages is not desirable.

- Not the implant dose is determining the electrochemical behaviour but rather the defect profile, i.e. the concentration of defects and their distribution in the substrate. Therefore, similar behaviour can be obtained with low doses of heavy ions and high doses of light ions (provided that the energies are well adapted).
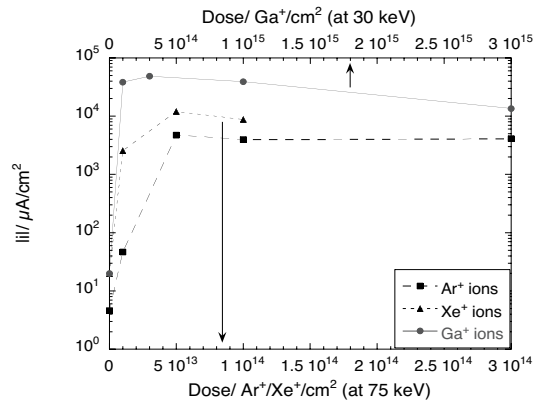
Fig. 4.48: Deposition current at -1500 mV for different implantation doses and different ions in electrolyte 2.

IPDS samples were also used to test the resolution of the process. Figure 4.49 demonstrates that IPDS followed by selective electrochemical metal deposition has the potential for sub-100 nm resolution. In our limited attempts 100 nm resolution was achieved over several 100 μm². The left SEM-micrograph shows a resist-covered sample after IPDS exposure; the sample was taken to measure the resolution of the IPDS tool. The Cu deposits match almost perfectly the resolution of IPDS as obtained in resist (figure 4.49, right).
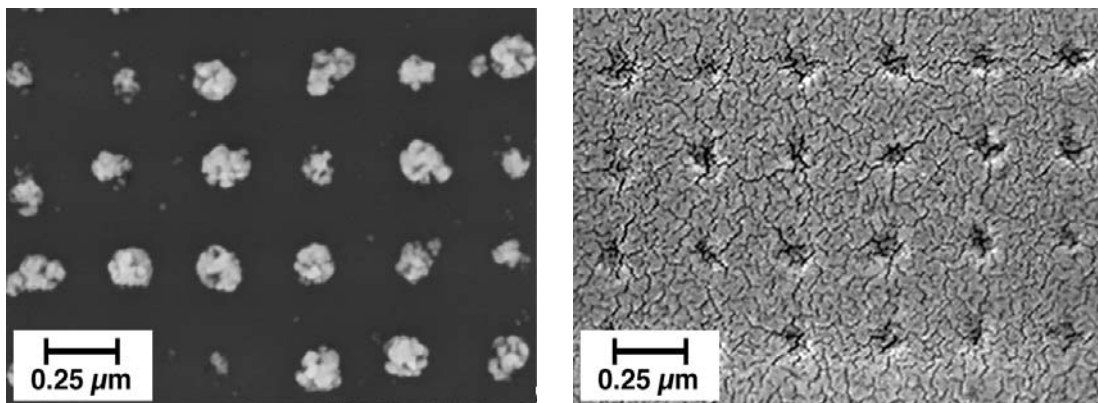

Fig. 4.49: SEM pictures of IPDS implanted samples. Left: Cu nanodots (implantation: $5 \cdot 10^{13}$ Xe⁺/cm² at 75 keV, deposition at -2500 mV for 3 s in electrolyte 2); right: implanted resist for 'benchmarking' purposes (the cracks are due to a Au sputter coat for enhanced SEM contrast).

While the structures are not perfect, they show great potential. Also, it seems that the implantation process itself can be further optimized as the implant in resist does not seem to be perfectly regular either. A peel-off test which was performed to test the adherence of the samples to the substrate also showed promising results: the Cu structure was not damaged and only undesired crystallites, which had developed at unimplanted sites, were removed (figure 4.50). It seems that ion implantation not only promotes electrochemical reactions but also increases adherence.
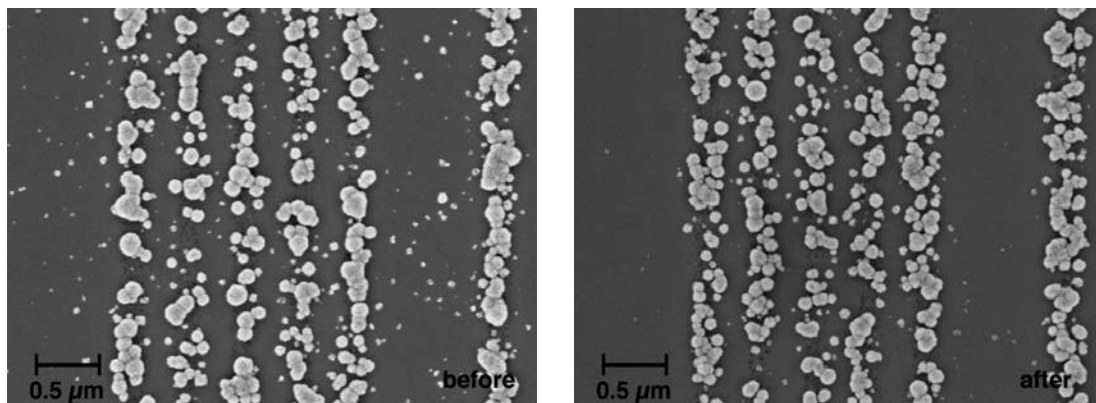
Fig. 4.50: SEM picture of Cu structure before (left) and after (right) peel-off test (implantation: $5 \cdot 10^{13}\,Xe^{+}/cm^{2}$ at 75 keV, 1.5 s at -3000 mV and 3 s at -1500 mV).

Chapter 5

CONCLUSION

In the present work we show that ion implantation of p-type Si may be used to selectively deposit different metals in a mask- and resistless process. Damage induced by implantation with different ionic species (Ga^+, He^+, Ar^+, Xe^+), energies, and doses creates enough additional states in the band gap to enable localized electrochemical reactions; on these localized damage zones metallic nanostructures in the 100 nm range were successfully deposited.

During our investigation we have characterized the influence of the main parameters both for ion implantation and for electrochemical deposition. Also, fundamental information on the deposition process itself was acquired, mainly by use of a microcapillary-based electrochemical method suited for the analysis of small surface areas

In the first part of our work we studied the ion implantation of Si; these results were used to 'benchmark' the FIB tool used. Sputter-profiles were obtained and compared with corresponding implantation profiles as calculated by numerical simulation. Good agreement was found between the simulated and the measured profiles.

In the second part we concentrated on optimizing the quality of the deposits both with respect to spatial resolution and deposit quality by identifying key parameters. For the study of factors influencing deposit structure, BII implanted samples were used due to their good homogeneity and the reproducibility of the results. Experiments were carried out in an acidic Cu containing electrolyte and in a basic Au based one. It was found that the implant dose is of great importance: for low doses ($< 10^{13}\,Ga^+/cm^2$) the damage created was not sufficient for the implant to be fully covered by the metal structure; in contrast for high doses

($\geq 10^{15}$ Ga$^+$/cm^2) a masking effect could be observed where no metal was deposited on the implant zone. We assume that this masking effect is caused by the complete amorphization of the substrate at these high doses (as confirmed by Raman spectroscopy) leading to a 100-fold increased electrical resistivity when compared with crystalline p-Si.

For Cu containing electrolytes the addition of BTA –a brightening agent also known for its Cu-corrosion inhibiting effect– proved crucial for high quality deposits. While BTA-less electrolytes lead to coarsely grained, uneven deposits with needle-like dendritic structure, the addition of BTA leads to small, spherical crystallites of 50 nm and less in diameter which coalesce to smooth, massive deposits. Also, selectivity seemed slightly increased leading to smaller deposits. We assume this effect is due to the formation of an insulating layer both at the Si surface and on the Cu deposits resulting in a general slow-down of the deposition. An increased resistivity of the electrode-electrolyte interface (as measured by impedance spectroscopy) seems to support this hypothesis.

The influence of deposition time and potential was studied both for Au and Cu (with and without BTA) containing electrolytes. The effects found were the same for all samples and can be summarised as follows. Short deposition times lead to small crystallites and do not allow the deposits sufficient growth to cover the entire implant area, whereas long deposition times often lead to massive outgrowth and, consequently, to reduced pattern resolution. Similar effects are observed for the applied deposition potential: at potentials close to the ocp the crystallites grow slowly and sparsely, while more cathodic potentials lead to faster and denser growth. For good deposits intermediate deposition potentials (-1500 mV for Cu and -2500 mV for Au) seem best, combined with intermediate deposition times (15 s). In general, Au samples showed less outgrowth and smaller crystallites, but coalescence was often more of a problem.

FIB implanted samples were used to obtain high resolution structures. Several interesting observations were made. FIB implanted samples were up to 100 times more tolerant with respect to the dose needed for substrate amorphization when compared with the BII implanted samples. We assume that this is due to the short pixel dwell times, combined with the high current fluences chosen for FIB operation; other authors have noted that these parameters play an important role for the defect accumulation in the crystal. Short dwell

times favour self-healing processes in the crystal, while high current densities may lead to overlapping ion-impacts on the substrate, reducing the number of effective impacts. As we operated at the shortest dwell time possible (in order to obtain better spatial resolution) and at high current densities (for shorter implantation times at high implant doses) an important difference from BII implanted samples seems reasonable. For doses of roughly $10^{14}\,\mathrm{Ga^+/cm^2}$ Cu lines as fine as 200 nm were obtained over a length of 40 µm.

Using a microcapillary, detailed microelectrochemical analysis of the deposition process was performed. The influences of the implanted species, implant energy, and implant dose as well as electrolyte composition were studied. It was found that the choice of implanted species does not seem to play a crucial role as long as *the depth distribution and the amount of damage created* remain constant. By implanting different ionic species at different energies we found that for all the species used, an implant dose, d_{crit}, of maximum deposition current exists. The best results are usually obtained for implant doses lower than d_{crit} as the reaction kinetics are unfavourable for good deposits to develop at d_{crit}. For significantly lower implantation doses, complete coverage of the implant may be difficult to achieve as the reactions take place too slowly. For implantation doses $>d_{\mathrm{crit}}$ the deposition current is reduced and outgrowth occurs readily while complete coverage of the implant remains difficult; we assume that this is due to the amorphization of the substrate as mentioned above.

Current-transient analysis was used to identify the nature of the deposition process and to calculate the diffusion coefficient, D, of the electrolyte. In all cases D depended exponentially on the applied potential, which may explain the great importance of the applied potential for the quality of the deposits. For Cu containing electrolytes BTA slows down diffusion mainly at more cathodic potentials, while it may even increase diffusion close to the ocp. The nucleation mechanism for Cu containing electrolytes was identified as progressive; therefore the deposit quality depends strongly on the deposition time. Au containing electrolytes have a more instantaneous nucleation behaviour, a characteristic which is even more marked for lower potentials. This is probably the reason why the characteristics of Au deposits are less sensitive to the deposition time than Cu deposits.

Mott-Schottky plots and theoretical considerations were used to develop a model of the deposition process. It was found that Cu deposition should not occur on p-Si as the substrate is in depletion condition. Microelectrochemical experiments show indeed that deposition is impossible on defect-free zones. Only on defect sites Cu^{2+} may be reduced by hole tunnelling through the interface via additional states in the bandgap to form nuclei. Once nuclei are formed and stable, these also act as sites of increased reactivity due to a facilitated charge transfer at the nucleus/Si interface. We therefore think that deposition is only possible at defect sites and that ion beam implantation is a suitable technique to create these defects. Since the species of the implanted ion seemed secondary for the results, we believe that it is indeed the damage created by the impact of the ion and not any local doping of the substrate that is responsible for the selectivity.

Finally, IPDS was used to implant large surface areas with high resolution structures through a stencil mask. In these experiments various noble gas ions at 75 keV were used. Even though implant conditions were quite different from before, structures as small as 100 nm were deposited over a surface of several mm^2 using the same parameters as previously. These structures reflect the morphology of the implants, indicating that the limiting factor still lies with the implantation process and not with the electrochemistry. These experiments also demonstrate the 'robustness' of the process as the structures were obtained in a normal laboratory environment rather than in a cleanroom.

By using ion projection lithography in conjunction with a stencil mask (as well as a broad range of different ionic species at different energies) instead of a FIB, the universality of the approach was demonstrated. Furthermore, the successful use of IPDS for damage creation shows the potential for larger scale applications of the process; based on these findings a patent request was filed together with our partners from the Fraunhofer Institute (see chapter 3.2.2).

5.1 Outlook

We have shown that ion beam induced damage can be used to selectively deposit metals onto a p-Si surface. Still, several interesting points remain to be investigated touching upon both scientific aspects as well as questions concerning possible industrial applications.

For one, the universality of the approach remains to be tested, i.e. whether the same procedure can be used for other p-type semiconductors. Even though all previous experience would encourage us to believe so, the experiment remains to be done. Also, the possibility to deposit insulating or semiconducting materials should be investigated; especially insulators may offer interesting new applications.

The resolution of the process may be further increased below 50 nm by use of lower implant energies. If combined with more refined electrolytes, this may indeed offer an alternative to photolitographic techniques. For industrial applications, it would be necessary to investigate the consequences of exposing a wafer surface to an electrolyte with respect to surface contamination. Also, compatibility of the process with standard industrial procedures and technologies would have to be looked into and feasibility studies concerning the integration of IPDS combined with selective electrochemistry into an industrial environment would have to be made.

In general the question of usefulness of the structures obtained remains somewhat unanswered: nevertheless, the potential for creating structures showing quantum confinement effects for fundamental studies, microelectromechanical systems (MEMS), or conductive layers/paths for ICs remains.

APPENDIX

The following pages will give an overview over the experiments performed in the 3 main electrolytes. The potentials used were -2500 mV, -1500 mV, and -500 mV (electrolyte 1 and 2), and -4000 mV, -2500 mV, and -1300 mV for electrolyte 3. Exposure times used are 30 s, 15 s, and 2 s at doses $10^{15}\,Ga^+/cm^2$, $5 \cdot 10^{13}\,Ga^+/cm^2$, and $10^{12}\,Ga^+/cm^2$. Some pictures are missing, indicating that no trace of the implant or the deposit were visible by SEM. All images are arranged according to the following table:

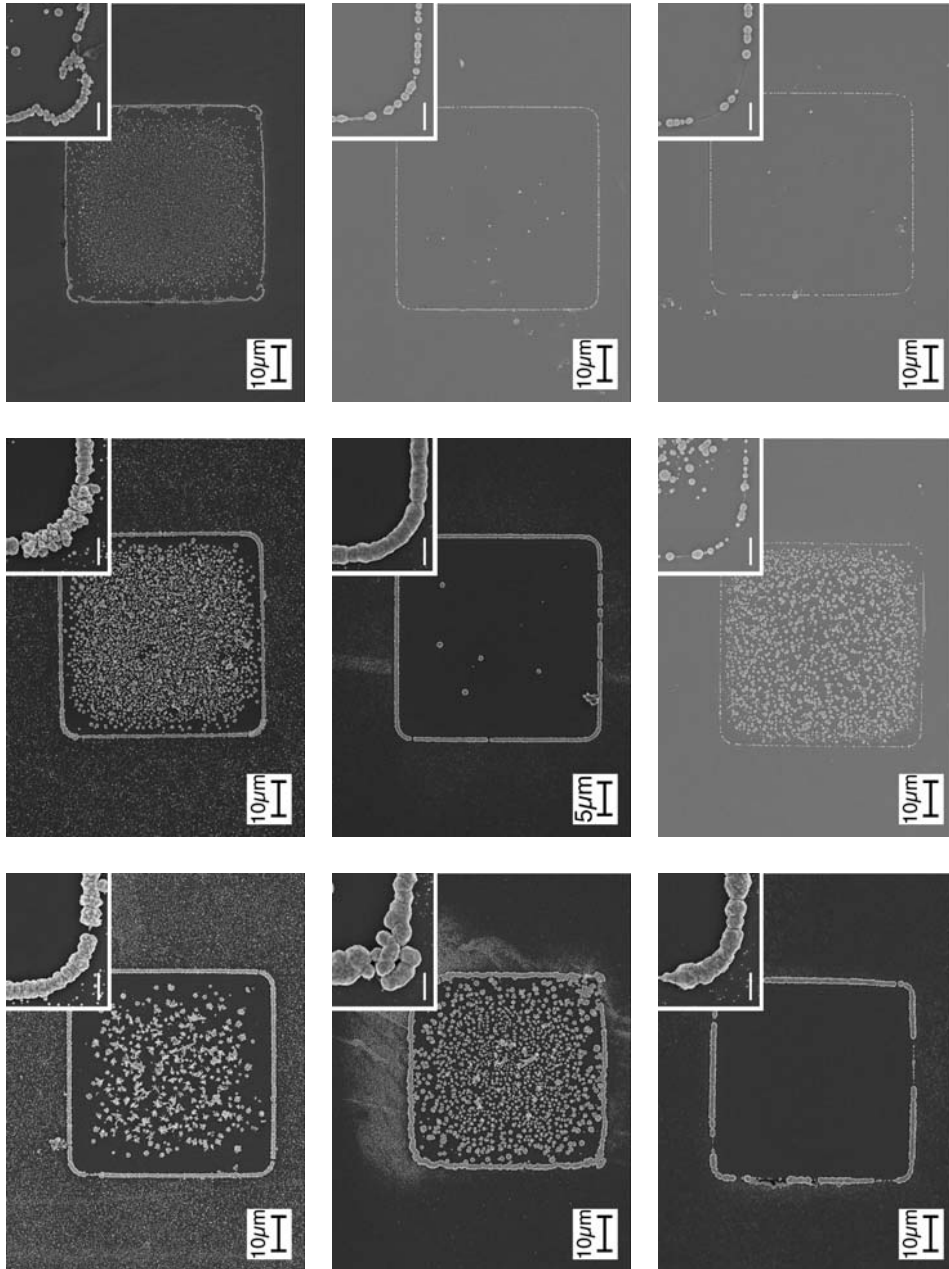|	30 s	15 s	2 s
-2500 mV (electrolyte 1 and 2) -4000 mV (electrolyte 3)	30 s @ -2500 mV/ 30 s @ -4000 mV	15 s @ -2500 mV/ 15 s @ -4000 mV	2 s @ -2500 mV/ 2 s @ -4000 mV
-1500 mV (electrolyte 1 and 2) -2500 mV (electrolyte 3)	30 s @ -1500 mV/ 30 s @ -2500 mV	15 s @ -1500 mV/ 15 s @ -2500 mV	2 s @ -1500 mV/ 2 @ -2500 mV
-500 mV (electrolyte 1 and 2) -1300 mV (electrolyte 3)	30 s @ -500 mV/ 30 s @ -1300 mV	15 s @ -500 mV/ 15 s @ -1300 mV	2 s @ -500 mV/ 2 s @ -1300 mV

Fig. 1.1: Overview: deposits using electrolyte 1 on p-Si implanted with $10^{15}\,\mathrm{Ga^+/cm^2}$ by BII.

Fig. 1.2: Overview: deposits using electrolyte 1 on p-Si implanted with $5 \cdot 10^{13}$ Ga^+/cm^2 by BII.

Fig. 1.3: Overview: deposits using electrolyte 1 on p-Si implanted with $10^{12}\,\mathrm{Ga^+/cm^2}$ by BII.
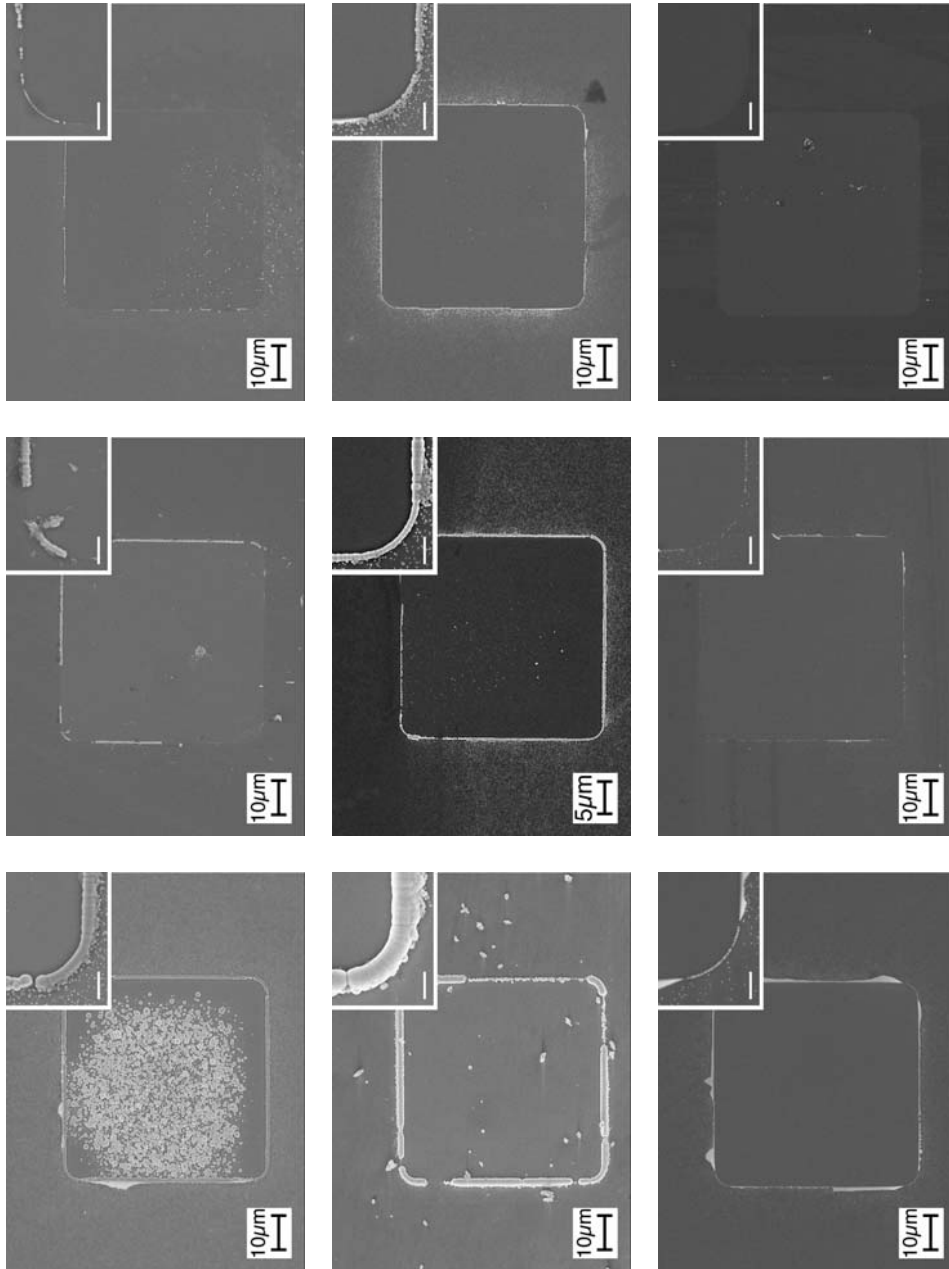
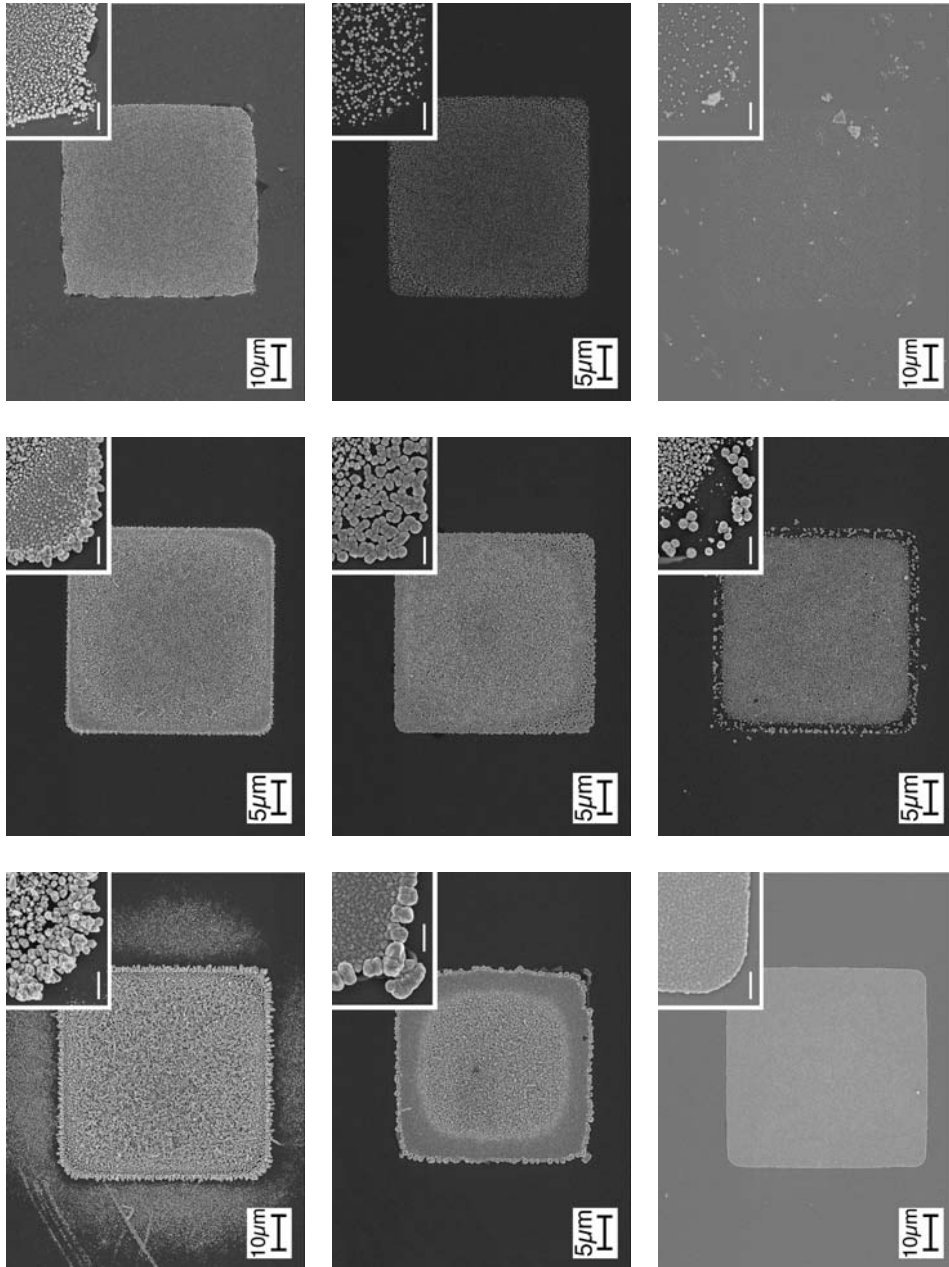**Fig. 1.4:** Overview: deposits using electrolyte 2 on p-Si implanted with $10^{15}\,\mathrm{Ga^+/cm^2}$ by BII.

Fig. 1.5: Overview: deposits using electrolyte 2 on p-Si implanted with $5 \cdot 10^{13}$ Ga^+/cm^2 by BII.
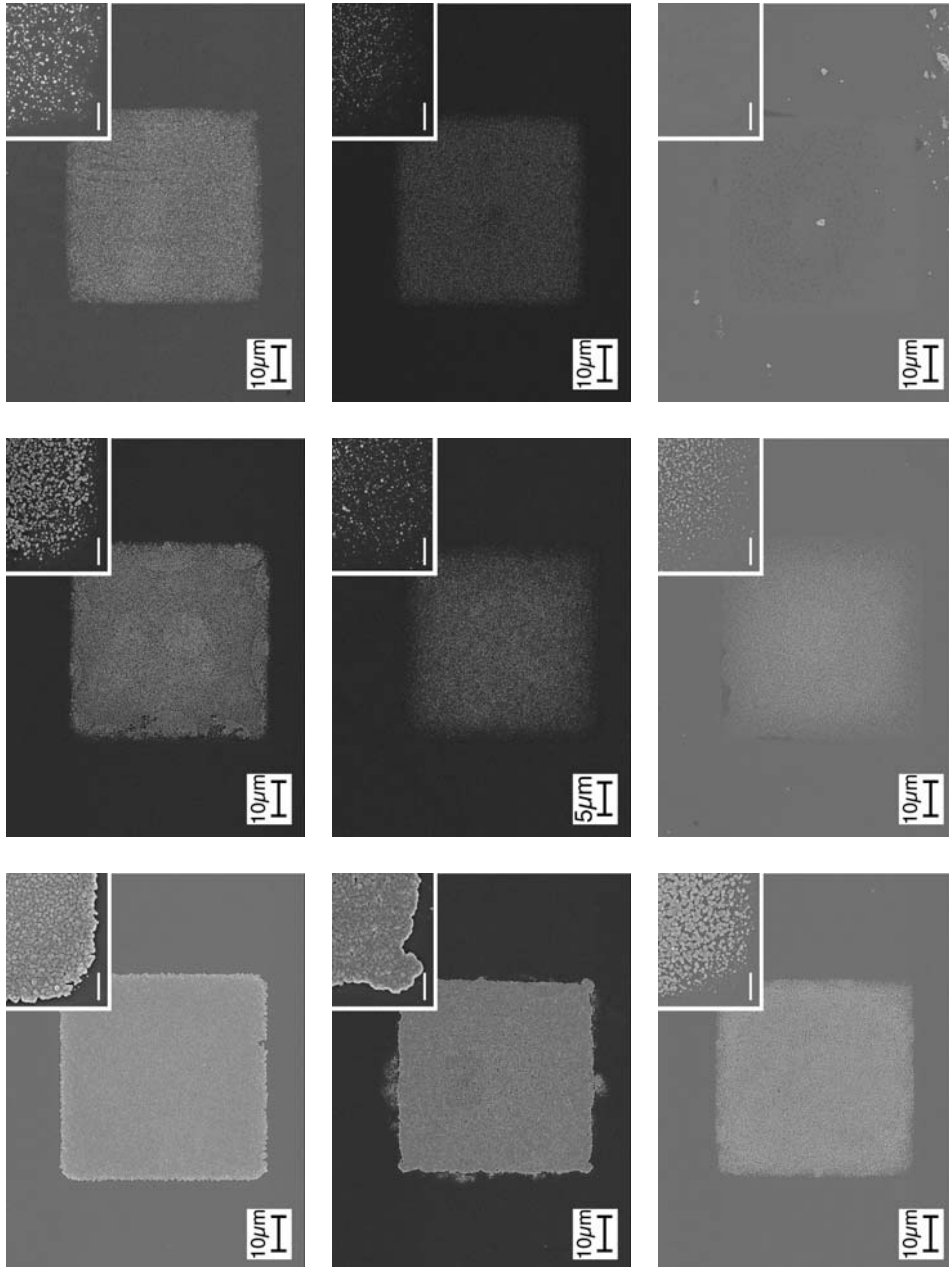
Fig. 1.6: Overview: deposits using electrolyte 2 on p-Si implanted with $10^{12}\,\mathrm{Ga^+/cm^2}$ by BII.

Fig. 1.7: Overview: deposits using electrolyte 3 on p-Si implanted with $10^{15}\,\mathrm{Ga^+/cm^2}$ by BII.
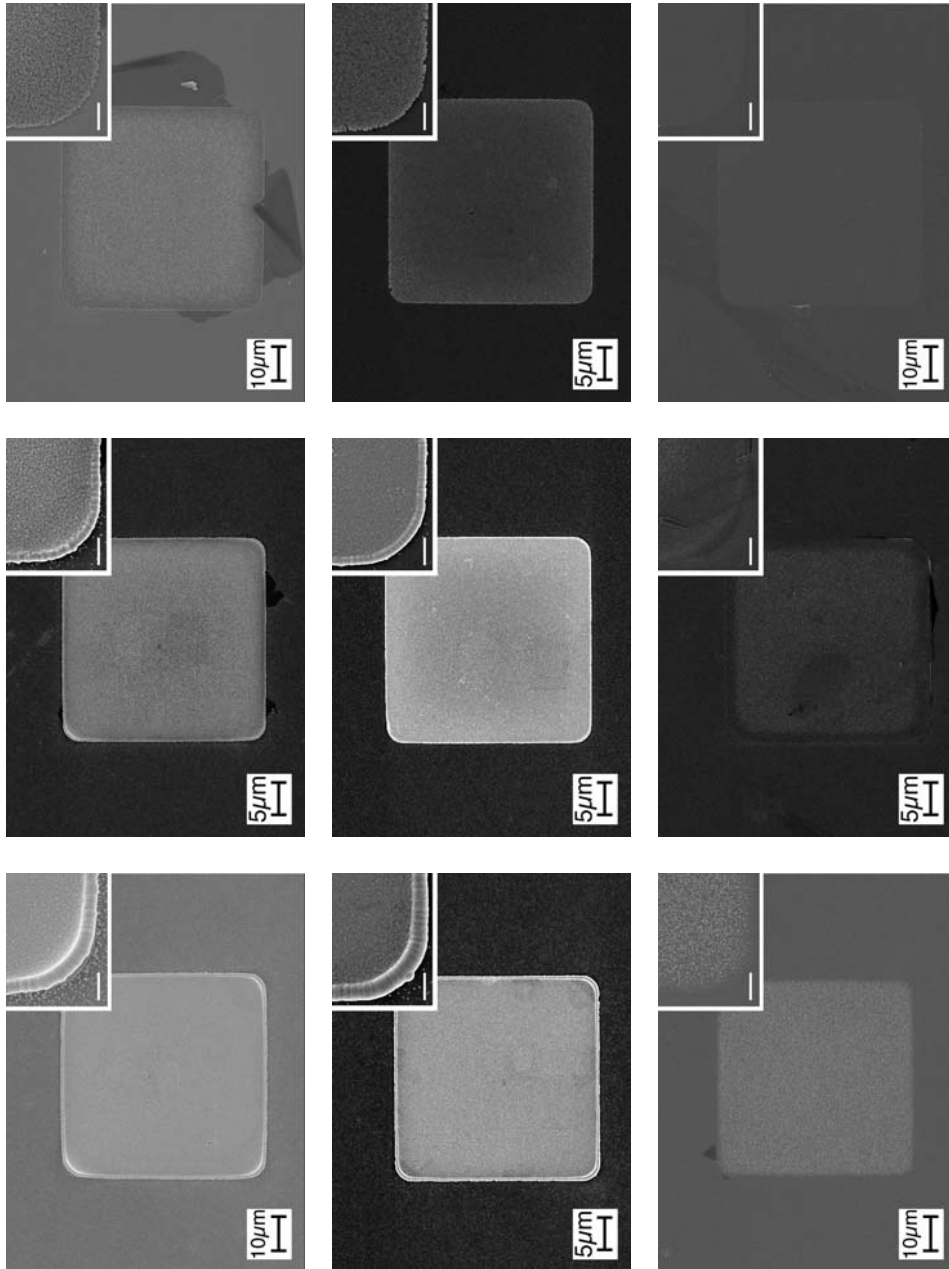
Fig. 1.8: Overview: deposits using electrolyte 3 on p-Si implanted with $5 \cdot 10^{13}$ Ga$^+$/cm^2 by BII.

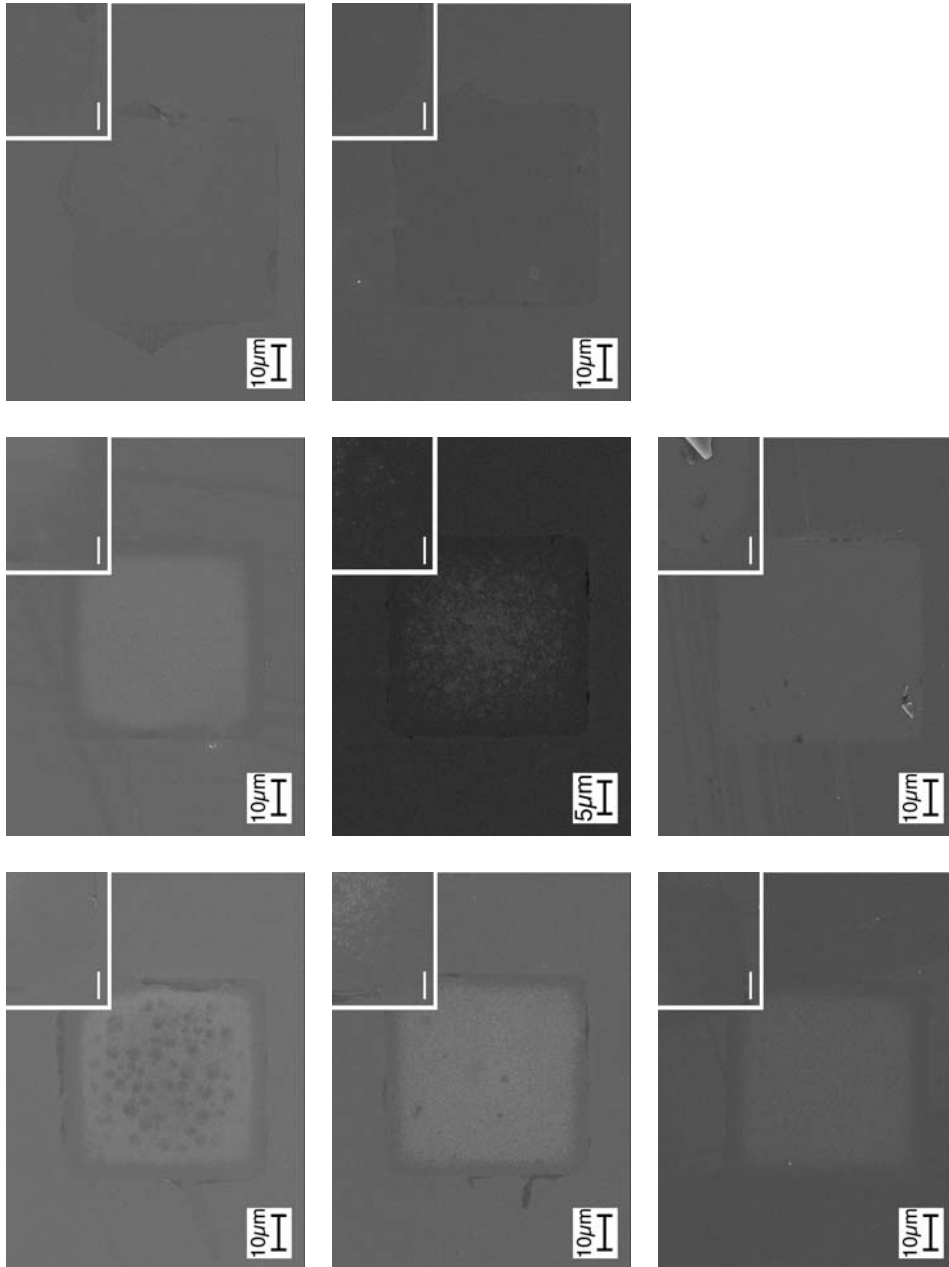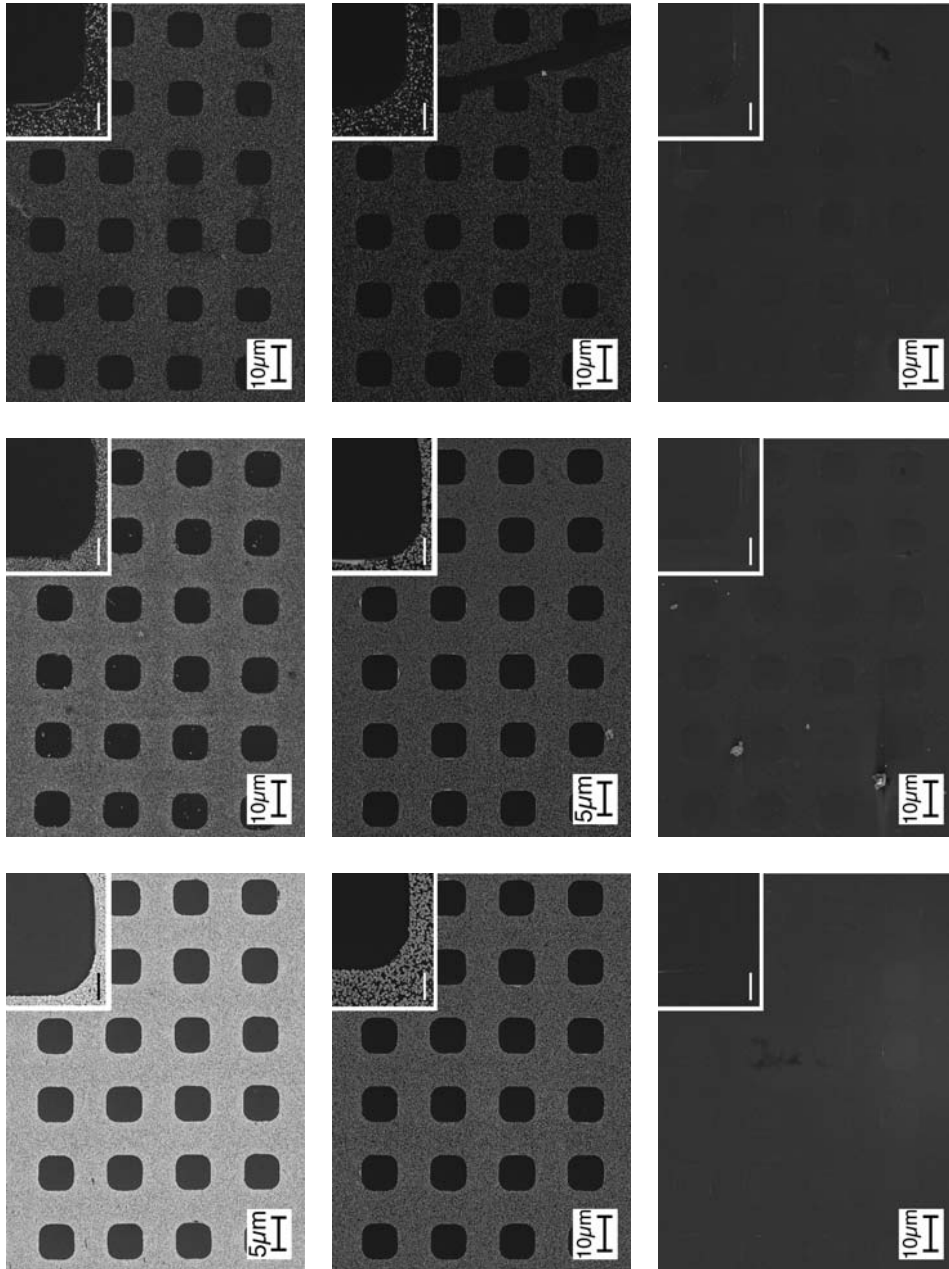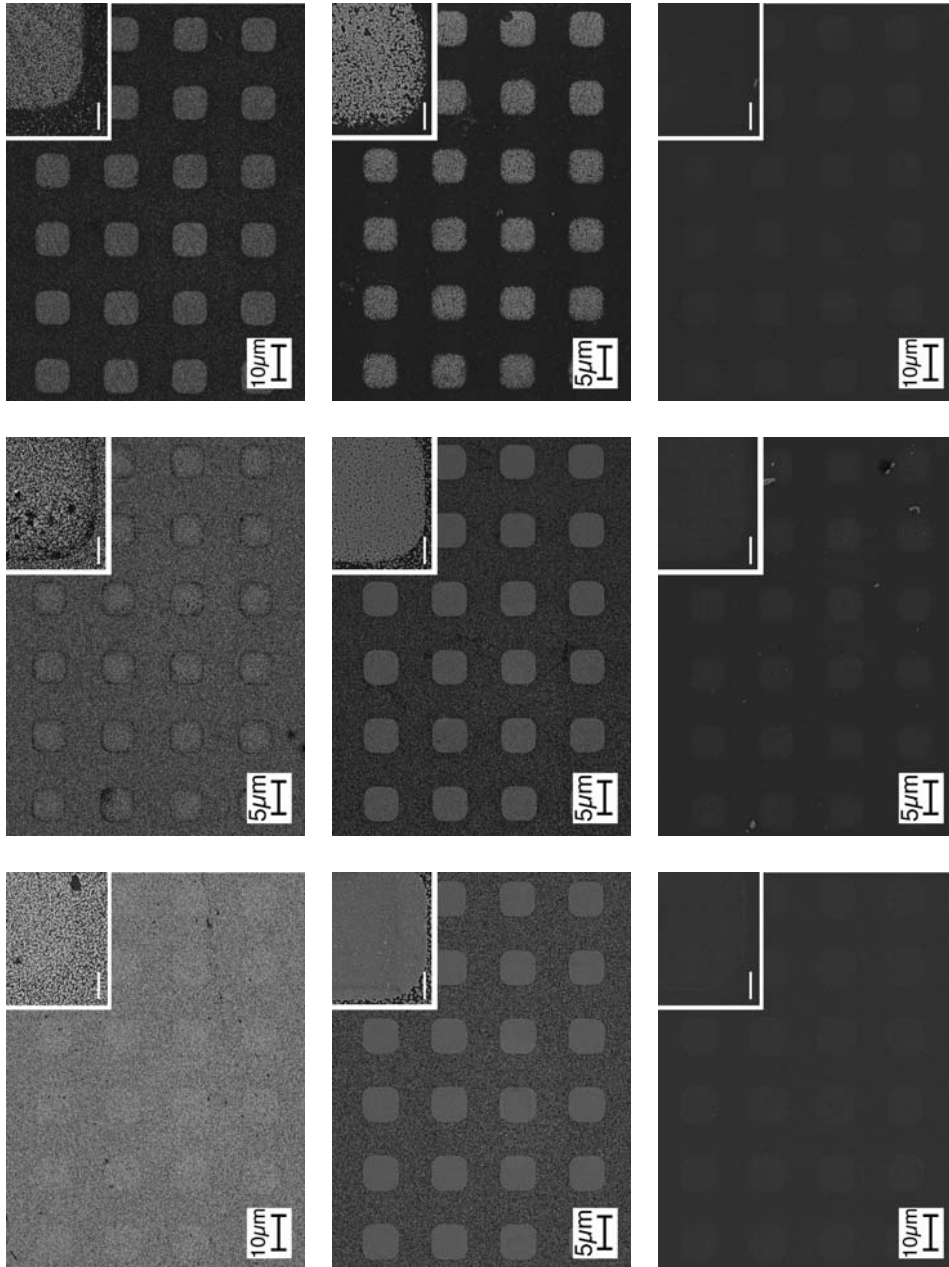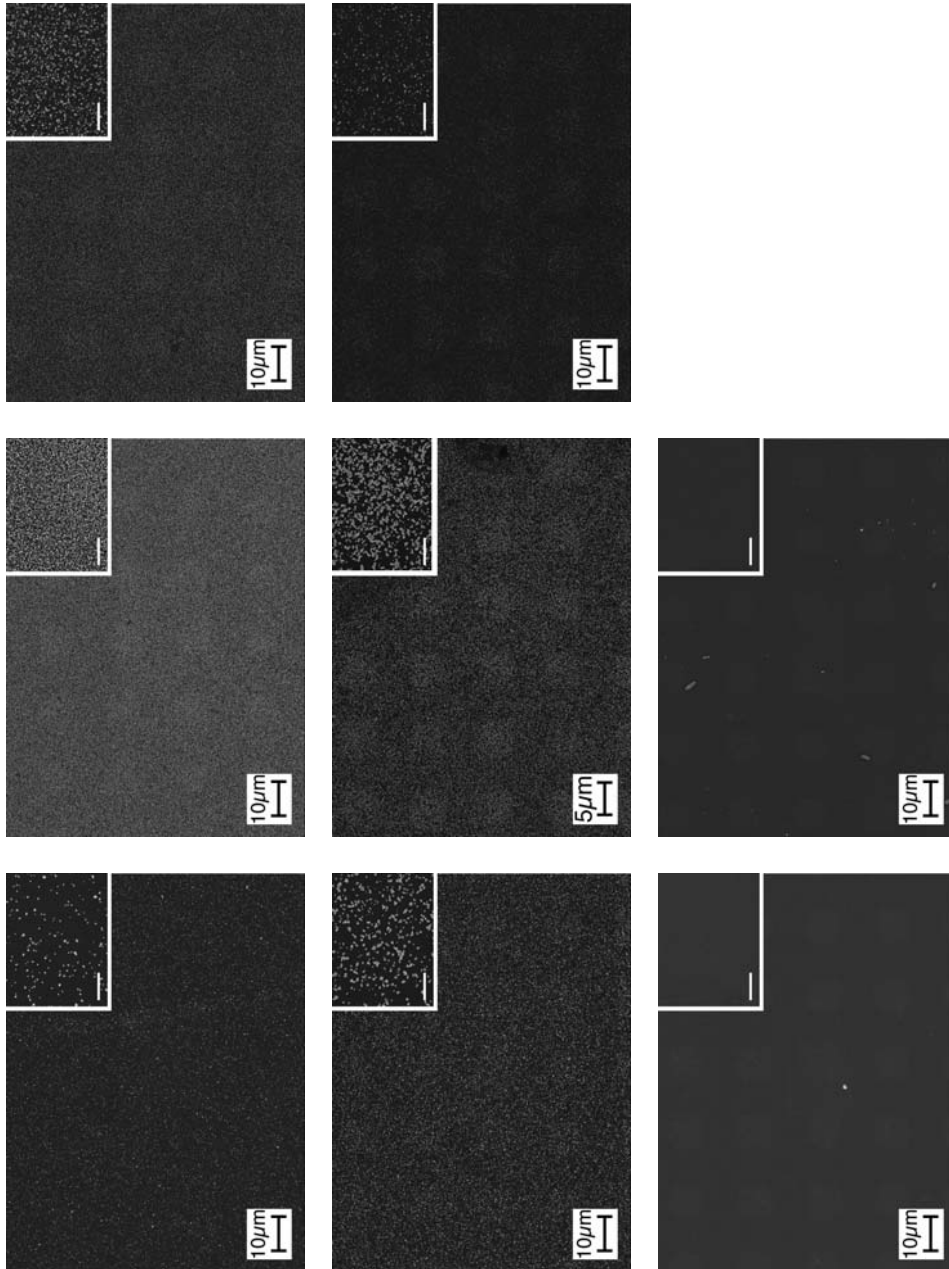**Fig. 1.9:** Overview: deposits using electrolyte 3 on p-Si implanted with $10^{12}\,\mathrm{Ga^+/cm^2}$ by BII.

REFERENCES

[1]   J. S. Kilby, "*Miniaturized Electronic Circuits*", Patent #: 3138743, USA, 1959.

[2]   G. Moore, *Electronics*, 114 (1965).

[3]   A. Fowler, *Phys. Today*, **50**, 50 (1997).

[4]   S. H. M. Persson, L. Olofsson, and L. Gunnarsson, *Appl. Phys. Lett.*, **74**, 2546 (1999).

[5]   S. Nonogaki, T. Ueno, and T. Ito, *Microlithography fundamentals in semiconductor devices and fabrication technology*, Dekker, New York (1998).

[6]   P. Van Zant, *LinkMicrochip fabrication : a practical guide to semiconductor processing*, McGraw-Hill, New York (1997).

[7]   *Processing of semiconductors*, VCH, Weinheim (1996).

[8]   J. Melngailis, A. A. Mondelli, I. L. Berry III, and R. Mohondro, *J. Vac. Sci. Technol. B*, **16**, 927 (1998).

[9]   P. Schmuki, L. E. Erickson, and D. J. Lockwood, *Phys. Rev. Lett.*, **80**, 4060 (1998).

[10] A. Spiegel, L. E. Erickson, and P. Schmuki, *J. Electrochem. Soc.*, **147**, 2993 (2000).

[11] W. Blum, *J. Electrochem. Soc.*, **99**, 31C (1952).

[12] H. W. Dettner, J. Elze, and E. Raub, *Handbuch der Galvanotechnik*, Carl Hanser Verlag, München (1966).

[13] B. L. McKinney and C. L. Faust, *J. electrochem. Soc.*, **124**, 379C (1977).

[14] D. Landolt, *J. Electrochem. Soc.*, **149**, S9 (2002).

[15] L. F. Thomson, C. G. Wilson, and M. J. Bowden, *Introduction to Microlithography*, American Chemical Society, Washington D.C. (1994).

[16] S. M. Sze, *VLSI Technology*, McGraw-Hill, New York (1988).

[17] S. K. Ghandi, *VLSI Fabrication Principles*, John Wiley & Sons, New York (1983).

[18] Y. Shacham Diamand and Y. Sverdlov, *Microelectron. Eng.*, **50**, 525 (2000).

[19] P. Neves Hercules, D. Kudrle Thomas, M. Chen Jia, G. Adams Scott, M. Maharbiz, S. Lopatin, and N. C. MacDonald, Mat. Res. Soc. Symp. Proc., PV **546**, 139 (1999).

[20] G. Oskam, J. G. Long, M. Nikolova, and P. C. Searson, Mat. Res. Soc. Symp. Proc., PV **451**, 257 (1997).

[21] G. Oskam, D. van Heerden, and P. C. Searson, *Appl. Phys. Lett.*, **73**, 3241 (1998).

[22] G. Oskam, P. C. Searson, and M. W. Cole, *Appl. Phys. Lett.*, **76**, 1300 (2000).

[23] S. M. Sze, *Physics of Semiconductor Devices*, Wiley, New York (1981).

[24] R. A. Colclaser, *Microelectronics: Processing and Device Design*, John Wiley & Sons, New York (1980).

[25] S. M. Sze, *Semiconductor devices: Physics and Technology*, Wiley, New York (1985).

[26] http://www.intel.com/intel/intelis/museum/exhibit/hist_micro/hof/hof_main.htm

[27] P. C. Andricacos, C. Uzoh, J. O. Dukovic, J. Horkans, and H. Deligianni, *IBM J. Res. Develop.*, **42**, 567 (1998).

[28] P. C. Andricacos, *Electrochem. Soc. Interf.*, **8**, 32 (1999).

[29] A. Radisic, A. C. West, and P. C. Searson, *J. Electrochem Soc*, **149**, C94 (2002).

[30] G. C. Taylor, D. W. Bechtle, P. C. Jozwiak, S. G. Liu, and R. L. Camisa, Proc. SPIE Int. Soc. Opt. Eng., PV **1475**, 103 (1991).

[31] S. Popelar, A. Strandjord, and B. Niemet, Proc. SPIE Int. Soc. Opt. Eng., PV **4587**, 575 (2001).

[32] J. G. Strandjord Andrew, S. Popelar, and C. Jauernig, *Microelectron. Reliab.*, **42**, 265 (2002).

[33] J. Tiffany, R. E. Cavicchi, and S. Semancik, Proc. SPIE Int. Soc. Opt. Eng., PV **4205**, 240 (2001).

[34] J. Mizsei, L. Pirttiaho, M. Karppinen, and V. Lantto, *Sens. Act. B*, **65**, 195 (2000).

[35] C. A. Scotchford, C. P. Gilmore, E. Cooper, G. J. Leggett, and S. Downes, *J. Biomed. Mater. Res.*, **59**, 84 (2002).

[36] D. Tidwell Caren, I. Ertel Sylvie, D. Ratner Buddy, J. Tarasevich Barbara, S. Atre, and L. Allara David, *Langmuir*, **13**, 3404 (1997).

[37] M. S. Lambrechts, W., *Biosensors: Microelectrochemical Devices*, Institute of Physics Publishing, Philadelphia, PA (1992).

[38] I. D. Karalemas, C. A. Georgiou, and D. S. Papastathopoulos, *Talanta*, **53**, 391 (2000).

[39] G. Scherb and D. M. Kolb, *J. Electroanal. Chem.*, **396**, 151 (1995).

[40] X. Ye, M. D. Bonte, J. P. Celis, and J. R. Roos, *J. Electrochem. Soc.*, **139**, 1592 (1992).

[41] P. Allongue and E. Souteyrand, *Electrochim. Acta*, **34**, 1717 (1989).

[42] P. Allongue and E. Souteyrand, *J. Electroanal. Chem.*, **286**, 217 (1990).

[43] R. Reineke and R. Memming, *Surf. Sci.*, **192**, 66 (1987).

[44] P. Allongue and E. Souteyrand, *J. Vac. Sci. Technol. B*, **5**, 1644 (1987).

[45] P. Bindra, H. Gerischer, and D. M. Kolb, *J. Electrochem. Soc.*, **124**, 1012 (1977).

[46] F. H. Dörbeck, *Sol. State Electron.*, **9**, 1135 (1966).

[47] F. Möller, H. J. Tolle, and R. Memming, *J. Electrochem. Soc.*, **121**, 1160 (1974).

[48] S. Menezes, A. Heller, and B. Miller, *J. Electrochem. Soc.*, **127**, 1268 (1980).

[49] E. Budevski, G. Staikov, and W. J. Lorenz, *Electrochim. Acta*, **45**, 2559 (2000).

[50] H. Gerischer, *Reactions at Semiconductor-Electrolyte Interfaces–Theory*, NATO Summer School Notes, Ghent (1968).

[51] H. Gerischer, *Z. Phys. Chem.*, **6**, 223 (1960).

[52] G. Oskam, J. G. Long, A. Natarajan, and P. C. Searson, *J. Phys. D: Appl. Phys.*, **31**, 1927 (1998).

[53] H. Cachet, M. Froment, E. Souteyrand, and C. Dennig, *J Electrochem Soc*, **139**, 2920 (1992).

[54] A. Spiegel, L. Staemmler, M. Dobeli, and P. Schmuki, *J. Electrochem. Soc.*, **149**, C432 (2002).

[55] L. Santinacci, T. Djenizian, and P. Schmuki, *J. Electrochem. Soc.*, **148**, C640 (2001).

[56] X. Cheng, G. Li, E. A. Kneer, B. Vermeire, H. G. Parks, S. Raghavan, and J. S. Jeon, *J. Electrochem. Soc.*, **145**, 352 (1998).

[57] Q. J. Chen, K. Imen, and S. D. Allen, *J. Electrochem. Soc.*, **147**, 1418 (2000).

[58] P. C. Andricacos, C. Uzoh, J. O. Dukovic, J. Horkans, and H. Deligianni, Electrochem. Soc. Symp. Proc., PV **98-6**, 48 (1999).

[59] T. P. Moffat, J. E. Bonevich, W. H. Huber, A. Stanishevsky, D. R. Kelly, G. R. Stafford, and D. Josell, *J. Electrochem. Soc.*, **147**, 4524 (2000).

[60] J. Orloff, *Rev. Sci. Instr.*, **64**, 1105 (1993).

[61] J. Orloff, *Sci. Am.*, **265**, 74 (1991).

[62] T. Tao, W. Wilkonson, and J. Melngailis, *J. Vac. Sci. Technol. B*, **9**, 162 (1991).

[63] R. Boylan, M. Ward, and D. Tuggle, Int. Sym. for Testing and Failure Analysis (ISTFA), 249 (1989).

[64] P. D. Prewett and P. J. Heard, *J. Phys. D: Appl. Phys.*, **20**, 1207 (1987).

[65] R. L. Kubena, F. P. Stratton, J. W. Ward, G. M. Atkinson, and R. J. Joyce, *J. Vac. Sci. Technol. B*, **7**, 1789 (1989).

[66] L. Bischoff and J. Teichert, AIP Conf. Proc., PV **392**, 1175 (1997).

[67] L. Bischoff, J. Teichert, E. Hesse, D. Panknin, and W. Skorupa, *J. Vac. Sci. Technol. B*, **12**, 3523 (1994).

[68] M. J. Vasile, C. Biddick, and S. A. Schwalm, *J. Vac. Sci. Technol. B*, **12**, 2388 (1994).

[69] T. Chraska, M. J. Cabra, S. Mesarovic, D. M. Longo, E. A. Stach, J. C. Bean, and R. Hull, Mat. Res. Soc. Symp. Proc., PV **636**, 362 (2001).

[70] R. Hull, T. Chraska, Y. Liu, and D. Longo, *Mat. Sci. Eng. C*, **C19**, 383 (2002).

[71] R. Hull and D. Longo, Proc. SPIE Int. Soc. Opt. Eng., PV **3975**, 974 (2000).

[72] A. Yamaguchi, M. Shibata, and T. Hashinaga, *J. Vac. Sci. Technol. B*, **12**, 2388 (1994).

[73] J. Melngailis, Proc. SPIE Int. Soc. Opt. Eng., PV **1465**, 36 (1991).

[74] H. D. Wanzenboeck, A. Lugstein, H. Langfischer, and E. Bertagnolli, Mat. Res. Soc. Symp. Proc., PV **624**, 163 (2000).

[75] H. D. Wanzenboeck, A. Lugstein, H. Langfischer, E. Bertagnolli, M. Gritsch, and H. Hutter, *IEE Conference Publication*, **473**, 485 (2000).

[76] C. Flier, I. H. White, M. Kuball, P. J. Heard, G. C. Allen, C. Marinelli, J. M. Rorison, R. V. Penty, Y. Chen, and S. Y. Wang, Mat. Res. Soc. Symp. Proc., PV **537**, 57 (1999).

[77] Y. Lee Hyun, W. Paek Seung, J. Lee Young, and B. Chung Hong, Int. Symp. Elec. Insul. Mat. (ISEIM), PV **98TH8286**, 151 (1998).

[78] R. Levi-Setti, J. M. Chabala, and Y. L. Wang, *Ultramicroscopy*, **24**, 97 (1988).

[79] Y. Yamaoka, T. Goto, M. Nakao, S. Kanemaru, and J. Itoh, *Jpn. J. Appl. Phys. 1*, **34**, 6932 (1995).

[80] S. Matsui, Y. Kojima, Y. Ochiai, T. Honda, and K. Suzuki, *Microelectron. Eng.*, **11**, 427 (1990).

[81] T. Ohta, T. Kanayama, and M. Komuro, *Microelectron. Eng.*, **6**, 447 (1987).

[82] H. Fuhrmann, M. Döbeli, R. Mühle, and M. Suter, *J. Vac. Sci. Technol. B*, **17**, 945 (1999).

[83] H. Fuhrmann, A. Candel, M. Döbeli, and R. Mühle, *J. Vac. Sci. Technol. B*, **17**, 2443 (1999).

[84] T. Kaito and T. Adachi, *J Jap Soc Prec Eng*, **53**, 857 (1987).

[85] A. J. Steckl, S. Balakrishnan, H. S. Jin, and J. C. Corelli, *Microelectron. Eng.*, **5**, 23 (1986).

[86] K. Gamo and S. Namba, *Microelectron. Eng.*, **11**, 403 (1990).

[87] R. Harriott Lloyd, *Jpn. J. Appl. Phys. 1*, **33**, 7094 (1994).

[88] T. P. Chiang, H. H. Sawin, and C. V. Thompson, *J. Vac. Sci. Technol. A*, **15**, 3104 (1997).

[89] K. Gamo, N. Takakura, N. Samoto, R. Shimizu, and S. Namba, *Jpn. J. Appl. Phys. 2*, **23**, L293 (1984).

[90] S. T. Davies and B. Khamsehpour, *Vacuum*, **47**, 455 (1996).

[91] S. Fujiwara and M. Komuro, *Publ by Foundation for the Promotion Ion Engineering, Jpn p*, 485 (1986).

[92] K. Wang, A. Chelnokov, S. Rowson, P. Garoche, and J. M. Lourtioz, Mat. Res. Soc. Symp. Proc., PV **637**, E141 (2001).

[93] M. Yoshida, S. Murakami, M. Nakayama, J. Yanagisawa, F. Wakaya, T. Kaito, and K. Gamo, *Microelec. Eng.*, **57-58**, 877 (2001).

[94] M. Ueda, S. Nagamachi, Y. Yamakage, H. Maruno, and J. Ishikawa, Electron-Beam Sources and Charged-Particle Optics, PV **2522**, 396 (1995).

[95] T. Chikyow, N. Koguchi, and A. Shikanai, *Surf. Sci.*, **386**, 254 (1997).

[96] M. M. Mitan, D. P. Pivin, T. L. Alford, and J. W. Mayer, *J. Vac. Sci. Technol. B*, **19**, 2525 (2001).

[97] A. Matsushita, T. Sadoh, and T. Tsurushima, Proc. Int. Conf. Ion Impl. Tech., PV **2**, 861 (1999).

[98] L. Bischoff and J. Teichert, *Appl. Surf. Sci.*, **184**, 336 (2001).

[99] W. H. Bruenger, M. Torkler, C. Dzionk, B. D. Terris, L. Folks, D. Weller, H. Rothuizen, P. Vettiger, G. Stangl, and W. Fallmann, *Microelectron. Eng.*, **53**, 605 (2000).

[100] K. Edinger, J. Melngailis, and J. Orloff, *J. Vac. Sci. Technol. B*, **16**, 3311 (1998).

[101] Y. Fu, A. Bryan Ngoi Kok, and N. Shing Ong, *Sens. Act. A*, **88**, 58 (2001).

[102] H. Langfischer, B. Basnar, H. Hutter, and E. Bertagnolli, *J. Vac. Sci. Technol. A*, **20**, 1408 (2002).

[103] S. Lipp, L. Frey, C. Lehrer, E. Demm, S. Pauthner, and H. Ryssel, *Microelectron. Reliab.*, **36**, 1779 (1996).

[104] M. Abramo, E. Adams, M. Gibson, L. Hahn, and A. Doyle, Ann. Proc. Reliab. Phys. Symp., 66 (1997).

[105] H. Komano, H. Nakamura, M. Kariya, and M. Ogasawara, Proc. SPIE Int. Soc. Opt. Eng., PV **2723**, 46 (1996).

[106] J. Funatsu, V. Thompson Carl, J. Melngailis, and N. Walpole James, *J. Vac. Sci. Technol. B*, **14**, 179 (1996).

[107] P. G. Blauner and A. Wagner, *Ion Solid Interactions for Materials Modification and Processing Materials Research Society Symposium Proceedings*, **396**, 695 (1996).

[108] R. L. Kubena, F. P. Stratton, and T. M. Mayer, Proc. SPIE Int. Soc. Opt. Eng., PV **1392**, 595 (1990).

[109] B. Schmidt, L. Bischoff, and J. Teichert, *Sens. Act. A*, 369 (1997).

[110] J. Brugger, G. Beljakovic, M. Despont, N. F. de Rooij, and P. Vettiger, *Microelectron. Eng.*, **35**, 401 (1997).

[111] W. Chen, P. Chen, A. Madhukar, R. Viswanathan, and J. So, Mat. Res. Soc. Symp. Proc., PV **279**, 599 (1993).

[112] H. Arimoto, M. Kosugi, H. Kitada, and E. Miyauchi, *Microelectron. Eng.*, **9**, 321 (1989).

[113] S. Rennon, L. Bach, H. Konig, J. P. Reithmaier, A. Forchel, J. L. Gentner, and L. Goldstein, *Microelectron. Eng.*, 57 (2001).

[114] J. Xu and A. J. Steckl, *Appl. Phys. Lett.*, **65**, 2081 (1994).

[115] K. D. Cummings, L. R. Harriott, G. C. Chi, and F. W. Ostermayer, Jr., Proc. SPIE Int. Soc. Opt. Eng., PV **632**, 93 (1986).

[116] P. Schmuki, L. E. Erickson, D. J. Lockwood, J. W. Fraser, G. Champion, and H. J. Labbe, *Appl. Phys. Lett.*, **72**, 1039 (1998).

[117] P. Schmuki, L. E. Erickson, and G. Champion, *J. Electrochem. Soc.*, **148**, C177 (2001).

[118] P. Schmuki and L. E. Erickson, Phys. Rev. Lett., **85**, 2985 (2000).

[119] C. Spinella, Mat. Sci. Semic. Proc., PV **1**, 55 (1998).

[120] G. Garozzo, A. La Magna, S. Coffa, G. D' Arrigo, N. Parasole, M. Renna, and C. Spinella, *Comp. Mat. Sci.*, **24**, 246 (2002).

[121] H. Son Seung, S. Park Yong, and Y. Choi Sie, *J. Micromech. Microeng.*, **12**, 63 (2002).

[122] D. M. Kolb, R. Ullmann, and T. Will, *Science*, **275**, 1097 (1997).

[123] D. M. Kolb, R. Ullmann, and J. C. Ziegler, *Electrochim. Acta*, **43**, 2751 (1998).

[124] L. Staemmler, T. Suter, and H. Bohni, *Electrochem. Solid State Lett.*, **5**, C61 (2002).

[125] L. Santinacci, T. Djenizian, and P. Schmuki, *Appl. Phys. Lett.*, **79**, 1882 (2001).

[126] D. Landolt, *Corrosion et Chimie de Surfaces des Métaux*, PPUR, Lausanne (1997).

[127] C. Kittel, *Introduction to Solid State Physics*, Wiley, New York (1956).

[128] S. M. Sze, *Semiconductor Devices - Physics and Technology*, Wiley, New York (1995).

[129] L. M. Peter, in *Porous silicon science and technology*, J. C. Vial and J. Derrien, Eds. Berlin: Springer, 1995.

[130] H. Gerischer, *Z. Phys. Chem.*, **26**, 40 (1961).

[131] R. A. Marcus, *J. Chem. Phys.*, **24**, 966 (1956).

[132] R. A. Marcus, *Can. J. Chem.*, **37** (1959).

[133] W. Schottky, *Z. Phys.*, **118**, 539 (1941).

[134] N. F. Mott, Proc. R. Soc., PV **A 171**, 27 (1939).

[135] W. Schottky, *Z. Phys.*, **113**, 367 (1939).

[136] S. R. Morrison, *The Chemical Physics of Surfaces*, Plenum Press, New York (1977).

[137] K. Micka and H. Gerischer, *J. Electroanal. Chem.*, **38**, 397 (1972).

[138] P. M. Hoffmann, A. Radisic, and P. C. Searson, *J. Electrochem. Soc.*, **147**, 2576 (2000).

[139] M. Volmer and A. Weber, *Z. Phys. Chem.*, **119**, 277 (1926).

[140] Erdey-Gruz and M. Volmer, *Z. Phys. Chem.*, **150A**, 201 (1930).

[141] Erdey-Gruz and M. Volmer, *Z. Phys. Chem.*, **157A**, 201 (1931).

[142] F. C. Frank, *Disc. Faraday Soc.*, **5**, 48 (1949).

[143] E. B. Budevski, "*Comprehensive Treatise of Electrochemistry*", vol. 7, E. B. Conway, Ed. New York: Plenum, 1983, p. 399.

[144] L. T. Romankiw and T. A. Palumbo, in *Electrodeposition Technology, Theory and Practice*, L. T. Romankiw and D. R. Turner, Eds. Pennington, NJ: Electrochem. Soc., 1988, p. 13.

[145] P. C. Searson and T. P. Moffat, *Crit. Rev. Surf. Chem.*, **3**, 171 (1994).

[146] M. Paunovic and M. Schlesinger, *Fundamentals of electrochemical deposition*, John Wiley & Sons Inc., New York (1998).

[147] P. Currie, *Comptes Rendus*, **130**, 76 (1900).

[148] J. F. Ziegler, J. P. Biersack, and U. Littmark, *The stopping and range of ions in solids*, Pergamon Press, New York, USA (1985).

[149] J. J. Thomson, *Conduction of Electricity through Gasses*, Cambridge University Press, Cambridge (1903).

[150] N. Bohr, *Phil. Mag.*, **25**, 10 (1913).

[151] N. Bohr, *Phil. Mag.*, **30**, 581 (1915).

[152] H. A. Bethe, *Ann. Phys.*, **5**, 325 (1930).

[153] H. A. Bethe, *Z. Physik*, **76**, 293 (1932).

[154] F. Bloch, *Ann. Phys.*, **16**, 287 (1933).

[155] F. Bloch, *Z. Physik*, **81**, 363 (1933).

[156] N. Bohr, *Phys. Rev.*, **58**, 654 (1940).

[157] N. Bohr, *Phys. Rev.*, **59**, 270 (1941).

[158] J. Lindhard, M. Scharff, and H. E. Schiott, *Mat. Fys. Medd. Dan. Vid. Selsk.*, **33** (1963).

[159] C. C. Rousseau, W. K. Chu, and D. Powers, *Phys. Rev.*, **A4**, 1066 (1970).

[160] W. K. Chu and D. Powers, *Phys. Lett.*, **A40**, 23 (1972).

[161] B. M. Latta and P. J. Scanlon, *Phys. Rev.*, **12A**, 34 (1975).

[162] G. J. Iafrate and J. F. Ziegler, *J. Appl. Phys.*, **50**, 5579 (1979).

[163] N. Bohr, *Mat. Fys. Medd. Dan. Vid. Selsk.*, **18** (1948).

[164] O. B. Firsov, *JEPT*, **7**, 308 (1958).

[165] O. B. Firsov, *Zh. Eksp. Teor. Fiz.*, **34**, 447 (1958).

[166] F. Bloch, *Z. Phys. Chem.*, **81**, 363 (1933).

[167] J. C. Ziegler and J. M. Manoyan, *Nucl. Instr. Meth. B*, **35**, 215 (1988).

[168] L. C. Northcliffe and R. F. Schilling, *Nucl. Data Tables*, **7**, 233 (1970).

[169] W. Brandt and M.-. Kitagawa, *Phys. Rev. B*, **25**, 5631 (1982).

[170] J. M. Anthony and W. A. Landford, *Phys. Rev. A*, **25**, 1868 (1982).

[171] http:///www.srim.org

[172] D. A. Thompson, *Rad. Eff.*, **56**, 105 (1981).

[173] T. D. De la Rubia, R. S. Averback, R. Benedek, and W. E. King, *Phys. Rev. Lett.*, **59**, 1930 (1987).

[174] M. J. Caturla, T. D. De la Rubia, and G. H. Gilmer, *Nucl. Instr. Meth. B*, **106**, 1 (1995).

[175] T. D. De la Rubia, *Nucl. Instr. Meth. B*, **120**, 19 (1996).

[176] G. H. Kinchin and R. S. Pease, *Rep. Progr. Phys.*, **18**, 1 (1955).

[177] H. H. Anderson, *Appl. Phys.*, **18**, 131 (1979).

[178] P. Sigmund, *Appl. Phys. Lett.*, **14**, 114 (1969).

[179] S. Hausmann, PhD, *Die Dynamik von Strahlenschaeden durch fokussierte Ionenstrahlen am Beispiel der Ionenstrahlsynthese*, Technische Univ. Dresden (Germany), 2001.

[180] J. F. Gibbons, Proc. IEEE, PV **56**, 295 (1968).

[181] J. F. Gibbons, Proc. IEEE, PV **60**, 1062 (1972).

[182] F. F. Morehead and B. L. Crowder, "*A model for the formation of amorphous Si by ion bombardment*", in *Ion implantation*, F. H. Eisen and L. T. Chadderton, Eds. London: Gordon and Breach Science Publishers, 1971.

[183] A. Natarajan, G. Oskam, and P. C. Searson, *J. Appl. Physics*, **83**, 2112 (1998).

[184] P. Schmuki, H. Bohni, and J. A. Bardwell, *J. Electrochem. Soc.*, **142**, 1705 (1995).

[185] G. Taylor, Proc. R. Soc. A, PV **133**, 383 (1964).

[186] Y. Lee, R. A. Gough, W. B. Kunkel, K. N. Leung, J. Vujic, M. D. Williams, D. Wutte, and N. Zahir, *Rev. Sci. Instr.*, **69**, 877 (1998).

[187] Y. Lee, R. A. Gough, K. N. Leung, J. Vujic, M. D. Williams, N. Zahir, W. Fallman, M. Tockler, and W. Bruenger, *J. Vac. Sci. Technol. B*, **16**, 3367 (1998).

[188] W. H. Bruenger, M. Torkler, K. N. Leung, Y. Lee, M. D. Williams, H. Loeschner, G. Stengl, W. Fallmann, F. Paschke, G. Stangl, I. W. Rangelow, and P. Hudek, *Microelectron. Eng.*, **46**, 477 (1999).

[189] A. Heuberger and W. Bruenger, *Microelectron. Eng.*, **34**, 39 (1996).

[190] A. Dietzel, R. Berger, H. Grimm, C. Schug, W. H. Bruenger, C. Dzionk, F. Letzkus, R. Springer, H. Loeschner, E. Platzgummer, G. Stengl, S. Anders, Z. Z. Bandic, C. T. Rettner, B. D. Terris, H. Eichhorn, M. Boehm, and D. Adam, Mat. Res. Soc. Symp. Proc., PV **705**, 279 (2002).

[191] L. M. Velesevich, S. S. Kruglikov, M. M. Yarlykov, and V. A. Morozov, *Sov. Electrochem.*, **23**, 920 (1987).

[192] J. Kim Jae, K. Kim Soo, and U. Bae Jong, *Thin Solid Films*, **415**, 101 (2002).

[193] W. U. Schmidt, R. C. Alkire, and A. A. Gewirth, *J. Electrochem. Soc.*, **143**, 3122 (1996).

[194] Y. Ling, Y. Guan, and K. N. Han, *Corrosion*, **51**, 367 (1995).

[195] S. L. F. A. da Costa and S. M. L. Agostinho, *Corrosion*, **45**, 472 (1989).

[196] C. Clerc and R. Alkire, *J. Electrochem. Soc.*, **138**, 25 (1991).

[197] A. M. Fenelon and C. B. Breslin, *J. Appl Electrochem*, **31**, 509 (2001).

[198] F. M. Al Kharafi and B. G. Ateya, *J. Electrochem. Soc.*, **149**, B206 (2002).

[199] D. Tromans and G. Li, *Electrochem. Solid State Lett.*, **5**, B5 (2002).

[200] T. Suter, T. Peter, and H. Böhni, *Mater. Sci. Forum*, **192-194**, 25 (1985).

[201] T. Suter, Ph.D. Thesis No. 11962, ETH Zürich, 1997.

[202] H. Böhni, T. Suter, and F. Assi, *Surf. Coat. Technol.*, **130**, 80 (2000).

[203] P. W. Nebiker, M. Doebeli, R. Muehle, M. Suter, and D. Vetterli, *Nucl. Instr. Meth. B*, **113**, 205 (1996).

[204] F. Yongqi, N. K. A. Bryan, S. Ong Nan, and W. Hung Nguyen Phu, *Sens. Act. A*, **A79**, 230 (2000).

[205] P. Schmuki, L. E. Erickson, G. Champion, B. F. Mason, J. Fraser, and C. Moessner, *Appl. Phys. Lett.*, **70**, 1305 (1997).

[206] H. A. Fuhrmann, Ph.D. Thesis No. 13616, *Herstellung von sub-µm CoSi$_2$-Strukturen mit dem fokussierten Ionenstrahl*, ETHZ, 2000.

[207] J. G. Graselli and B. J. Bulkin, *Analytical Raman Spectroscopy*, John Wiley & Sons, Inc, New York (1991).

[208] A. Baba, D. Bai, T. Sadoh, A. Kenjo, H. Nakashima, H. Mori, and T. Tsurushima, *Nucl. Instr. Meth. B*, **121**, 299 (1997).

[209] S. Hausmann, L. Bisohoff, J. Teichert, M. Voelskow, D. Grambole, F. Herrmann, and W. Moller, *Appl. Phys. Lett.*, **72**, 2719 (1998).

[210] S. Hausmann, L. Bischoff, M. Voelskow, J. Teichert, W. Moller, and H. Fuhrmann, *Nucl. Instr. Meth. B*, **148**, 610 (1999).

[211] S. Hausmann, L. Bischoff, J. Teichert, M. Voelskow, and W. Moller, *J. Appl. Physics*, **87**, 57 (2000).

[212] M. Scendo and J. Malyszko, *J. Electrochem. Soc.*, **147**, 1758 (2000).

[213] T. Y. B. Leung, M. Kang, F. Corry Brian, and A. Gewirth Andrew, *J. Electrochem. Soc.*, **147**, 3326 (2000).

[214] R. B. Wehrspohn, J. N. Chazalviel, F. Ozanam, and I. Solomon, *Thin Solid Films*, **297**, 5 (1997).

[215] R. A. Street, *Technology and Applications of Amorphous Silicon*, Spriner, Berlin (2000).

[216] V. Augelli, "*Conductivity of undoped GD a-Si:H*", in *Properties of Amorphous Silicon*. London: INSPEC, 1989, p. 185.

[217] B. Scharifker and G. Hills, *Electrochim. Acta*, **28**, 879 (1983).

[218] J. A. Bardwell, N. Draper, and P. Schmuki, *J. Appl. Phys.*, **79**, 8761 (1996).

[219] T. Djenizian, L. Santinacci, and P. Schmuki, *J. Electrochem. Soc.*, **148**, C197 (2001).

LIST OF SYMBOLS

Roman letters

A:	Surface area
A_n:	Nucleation rate constant
a:	Screening parameter for Coulomb potential; fitting parameter
a_0:	Standard screening parameter for Coulomb potential
B:	Magnetic field
	Brightness
b:	Fitting parameter
C:	Capacity
C_S:	Spherical aberration of a lens
C_{scl}:	Capacity of the space charge layer
c:	Concentration
c_{ox}:	Concentration of the oxidized species
c_{red}:	Concentration of the oxidized species
D:	Diffusion coefficient; ion dose per cm^2
d_a:	Ion implantation dose needed for substrate amorphization
d_{crit}:	Ion implantation dose at which the deposition current is maximum
$D_{ox}(E)$:	Density of unoccupied states
$D_{red}(E)$:	Density of occupied states
e^-:	Electron
E:	Electric field
	Ion energy
E_c:	Lower level of the conduction band
$E_{c,b}$:	Lower level of the conduction band in the bulk semiconductor

$E_{c,s}$:	Lower level of the conduction band at the semiconductor surface
E_d:	Energy needed to create a stable Frenkel pair
E_F:	Fermi energy level
$E_{F,b}$:	Fermi energy level of the bulk semiconductor
$E_{F,s}$:	Fermi energy level of the semiconductor surface
E_F^{redox}:	Fermi energy level of the electrolyte
E_F^{SC}:	Fermi energy level of the semiconductor
E_g:	Band gap
E_{ox}:	Potential of the oxidized species
E_{redox}:	Redox potential
E_{red}:	Potential of the reduced species
E_v:	Upper level of the valence band
$E_{v,b}$:	Upper level of the valence band in the bulk semiconductor
$E_{v,s}$:	Upper level of the valence band at the semiconductor surface
f_a:	Degree of amorphization
h^+:	Hole
I:	Current
i:	Current density
i_{max}:	Maximum of the current density for current transient
J_{nucl}:	Rate of 2D-nucleation
k_r:	Rate constant of nucleation
M:	Molecular weight
Me:	Metal
N:	Number of ions or ions
n(E):	Electron density
N(E):	Density of allowed energy states per unit volume
$N(t)$:	Density of nuclei as a function of time
N_C:	Effective density of states in the conduction band
N_{crit}:	Number of atoms of the critical nucleus
N_D:	Donors concentration

N_∞:	Final density of nuclei
P(E):	Probability of occupying the energy state E
r:	Distance between two atoms
r_m:	Ultimate resolution of a lithographic system
R_p:	Penetration depth of an ion
R_t:	Ion range
$S(E)$:	Stopping power
T:	Temperature
t:	Time
t_max:	Time corresponding to the current maximum of a current transient
U_bd:	Schottky barrier breakdown potential
$U_\mathrm{bd,d}$:	Schottky barrier breakdown potential at defect site
$U_\mathrm{bd,s}$:	Schottky barrier breakdown potential at intact surface
U_d:	Deposition potential
U_Sb:	Schottky barrier potential
V:	Potential or applied voltage
V_fb:	Flat band potential
V_m:	Atomic volume
$V(r)$:	Screened Coulomb potential
$W_\mathrm{ox}(E)$:	Probability that the energy on an oxidized specie has fluctuated to energy E
$W_\mathrm{red}(E)$:	Probability that the energy on a reduced specie has fluctuated to energy E
W_scl:	Width of the space charge layer
w_b:	Approximated FIB beam width
X_0 or X^0:	Standard value of X
Z_X:	Atomic number of element X
z:	Number of electrons involved in redox reaction
	Penetration depth of ion in sample

Greek letters

ΔV:	Contact potential
$\Delta \Phi$:	Electric field across the interface
$\Delta \Phi_{GC}$:	Electric field of the Gouy-Chapman diffusion layer
$\Delta \Phi_H$:	Electric field of the Helmoltz double layer
$\Delta \Phi_{scl}$:	Electric field of the space charge layer
$\Delta \Phi^{\circ}_{scl}$:	Electric field of the space charge layer under equilibrium conditions
ΔG_c:	Critical Gibbs free energy
$\Delta G(N)$:	Gibbs free energy of a cluster formation of N ions
ΔX:	Variation of X
ε:	Dielectric constant in the direction normal to the surface
$\varepsilon(E)$:	Stopping cross section
$\Phi(N)$:	Excess energy due to the formation of a new interface (proportional to the surface)
γ:	Effective charge parameter
η:	Overvoltage
λ:	Reorganisation energy
	Wavelength
$\mu_{M,b}$:	Electrochemical potential of bulk metal
$\mu_{M,solv}$:	Electrochemical potential of solvated metal ion
v:	Ion velocity
v_0:	Orbital velocity of an electron
$v(E)$:	Ion's energy not used for electronic stopping
π-Si:	Porous silicon
ρ:	Density
σ:	Average specific surface energy
	Full width at half maximum
σ_0:	Diameter of amorphized cylinder created by impinging ion
ξ:	Fitting parameter depending on the scattering potential
Ω:	Segment of a circle

Acronyms

a-Si:	Amorphous silicon
AC:	Alternative current
AES:	Auger electron microscopy
AFM:	Atomic force microscopy
BTA:	Benzo triazole
CVC:	Current-density/voltage curve
CVD:	Chemical vapour deposition
DC:	Direct current
EPFL:	École Polytechnique Fédérale de Lausanne (Switzerland)
ESCM:	Electrochemical scanning capillary microscope
FAU:	Friedrich – Alexander Universität (Erlangen - Nuremberg, Germany)
FET:	Field effect transistor
FIB:	Focused ion beam
GPIB:	General purpose interface bus
IC:	Integrated circuit
IMS:	Ion Microfabrication Systems (Vienna, Austria)
IPDS:	Ion projection direct structuring
IPL:	Ion projection lithography
ISiT:	Institut für Siliziumtechnologie (Itzehoe, Germany)
LAIS:	Liquid alloy ion source
LIGA:	Lithographie für Galvanoabformung
LMIS:	Liquid metal ion source
MEMS:	Micro electromechanical system
MES:	Metal-semiconductor
MIPS:	Multicusp plasma ion source
MOS:	Metal-oxide-semiconductor
NEMS:	Nano electromechanical system
ocp:	Open cell potential
IS:	Plasma ion source

PMMA: Poly methyl methacrylate
PSI: Paul Scherrer Institut (Villigen, Switzerland)
SC: Semiconductor
SCE: Saturated calomel electrode
SCL: Space charge layer
SEM: Scanning electron microscopy
SIMS: Secondary ion mass spectroscopy
SRIM: Stopping and range of ions in matter
STM: Scanning tunnel microscope
TEM: Transmission electron microscopy
TRIM: Transport of ions in matter

Constants

h: Planck constant $6.626 \cdot 10^{-34}\,\mathrm{J \cdot s}$
k: Boltzmann constant $8.617 \cdot 10^{-5}\,\mathrm{eV \cdot K^{-1}}$
e: Electron charge $1.602 \cdot 10^{-19}\,\mathrm{C}$
R: Gas constant $8.314\,\mathrm{J \cdot mol^{-1} \cdot K^{-1}}$
F: Faraday constant $96485\,\mathrm{C \cdot mol^{-1}}$
N_A: Avogadro number $6.022 \cdot 10^{23}\,\mathrm{mol^{-1}}$
ε°: Permissivity of the vacuum $8.854 \cdot 10^{-14}\,\mathrm{F \cdot cm^{-1}}$
π: Pi 3.141593

CURRICULUM VITÆ

Name:	Adrian Spiegel
Place, date of birth:	Basel, Switzerland, November 16, 1974
Nationality:	Swiss

Education

1980 – 1984	Elementary school, Neubad-Nord, Basel, Switzerland.
1985 – 1993	High school, Humanistisches Gymnasium, Basel, Switzerland.
1993 – 1994	Jewish Theological Seminary, JTS, New York, USA.
1994 – 1999	Study at the Swiss Federal Institute of Technology Lausanne, EPFL, Switzerland, and at the University of Manchester Institute for Science and Technology, UMIST, GB (1996-1997). Diploma thesis on "Morphology and Photoluminescence in Localised Porous Silicon".
2000 – 2003	Ph.D. student at the Department of Materials Science at EPFL and at the Swiss Federal Institute of Technology Zurich, ETHZ, Switzerland. Ph.D. Thesis on "Electrochemical Investigation of Ion Implanted p-Si".

Professional Experience

1994 and 1995	Research work at Sandoz Pharmaceuticals Inc. (now Novartis Pharmaceuticals Inc., Basel, Switzerland): synthesis and characterization in the field of peptide chemistry.
1997	Research work at the electrochemistry laboratory at EPFL: influence of passivity on tribocorrosive wear of carbon steel in aqueous solution.
1999	Research work at the Ceramics laboratory at EPFL for Medtronic Inc.: "Corrosion of Silicon and Titanium in Drug Delivery Systems".
1999	Medical polymer research for drug delivery systems at Tokyo Women's Medical University, TWMU, Tokyo, Japan.

PUBLICATIONS

S. Mischler, A. Spiegel, and D. Landolt, "The role of passive oxide films on the degradation of steel in tribocorrosion systems", *Wear*, **229**, 1078 (1999).

A. Spiegel, L. E. Erickson, and P. Schmuki, "Selective growth of porous silicon on focused ion beam patterns", *J. Electrochem. Soc.*, **147**, 2993 (2000).

S. Mischler, A. Spiegel, M. Stemp, and D. Landolt, "Influence of passivity on the tribocorrosion of carbon steel in aqueous solutions", *Wear*, **250**, 1295 (2001).

A. Spiegel, M. Döbeli, and P. Schmuki, "Nanoscale Electrochemical Deposition of Metals on FIB Sensitized p-Type Silicon", *Mat. Res. Soc. Symp. Proc.*, **PV 705**, Y4.3.1 (2002).

A. Spiegel and P. Schmuki, "Controlled and Selective Aggregation of Submicrometer Cu-Crystallites on FIB Sensitized p-Si", *Mat. Res. Soc. Symp. Proc.*, **PV 704**, W7.10.1 (2002).

A. Spiegel, L. Staemmler, M. Döbeli, and P. Schmuki, "Selective electrodeposition of Cu nanostructures on focused ion beam sensitized p-Si", *J. Electrochem. Soc.*, **149**, C432 (2002).

A. Spiegel, W. H. Bruenger, and P. Schmuki, "Verfahren zur Herstellung einer Struktur auf einem Substrat - Methode zur galvanischen Abscheidung von Nanostrukturen auf Halbleiteroberflächen nach Bestrahlung durch Ionenprojektion", *German patent pending* (2002).

A. Spiegel, W. H. Bruenger, C. Dzionk, and P. Schmuki, "Ion projection sensitized selective Cu electroplating on uncoated p-Si", *J. Vac. Sci. B*, **20**, 2713 (2002).

A. Spiegel, W. H. Bruenger, C. Dzionk, and P. Schmuki, "Resistless Deposition of Metallic Nanostructures on Ion Projection Sensitized *p*–Si", *J. Micro. Nano. Eng.*, accepted for publication (2003).

T. Suter, A. Spiegel, and H. Böhni, "Microcell applications on different systems", in *Proc. Electrochem. Soc. Meeting Symp.*, **PV G1**, 377 (2003).

P. Schmuki, S. Maupai, T. Djenizian, L. Santinacci, A. Spiegel, U. Schlierf, "Techniques in Electrochemical Nanotechnology" in "Encyclopaedia of Nanoscience and Nanotechnology", Ed. H. S. Nalva, American Scientific Publishes (2003).

ACKNOWLEDGMENTS